Quantitative assessment of brain perfusion with magnetic resonance imaging

Bleeker, E.J.W.

Quantitative assessment of brain perfusion with magnetic resonance imaging

EGBERT J.W. BLEEKER

2011

COLOPHONE

About this cover

The four-leaf-clover is a symbol for luck, but is the arterial input function measurement of Dynamic Susceptibility Contrast MRI also a matter of luck? Models for an optimal location for arterial input function measurements, as presented in this thesis, show for both the magnitude and the phase of the MR signal a four-leaf-clover pattern. Is this just a coincidence or are we always lucky?

Quantitative assessment of brain perfusion with magnetic resonance imaging
Thesis, Leiden University Medical Center, with references and summary in Dutch

Layout and printing: Optima Grafische Communicatie, Rotterdam, The Netherlands
ISBN: 978-94-6169-054-8

Quantitative assessment of brain perfusion with magnetic resonance imaging

Proefschrift

ter verkrijging van
de graad van Doctor aan de Universiteit Leiden,
op gezag van de Rector Magnificus prof.mr. P.F. van der Heijden,
volgens besluit van het College voor Promoties
te verdedigen op woensdag 1 juni 2011
klokke 15:00 uur

door

Egbert Jan Willem Bleeker

geboren te Paramaribo
in 1980

PROMOTIECOMMISSIE

Promotores:	Prof. dr. A.G. Webb Prof. dr. M.A. van Buchem
Co-promotor:	Dr. ir. M.J.P. van Osch
Overige leden:	Prof. dr. P.R. Luijten (University Medical Center Utrecht, Utrecht, the Netherlands) Prof. dr. D.G. Norris (Donders Centre for Cognitive Neuroimaging, Nijmegen, the Netherlands) Dr. L. Knutsson (Lund University, Lund, Sweden)

Financial support for publication of this thesis was generously provided by: Philips Healthcare, Stichting Bazis, Stichting Imago, J.E.Jurriaanse Stichting, Guerbet Nederland BV, Bayer BV, Toshiba and Medrad Europe BV.

The research described in this thesis was carried out at the department of Radiology (head: prof. dr. J.L. Bloem) of the Leiden University Medical Center.

Aan mijn ouders

Contents

Chapter 1: General introduction

The human body is a wonderful creation and it is worth investigating its beauty. The order and complexity of life and living beings is surprising, especially the robust unity of all the complicated systems involved in sustaining and creating life. This thesis focuses on the human brain. More specifically, it focuses on the measurement of blood supply to brain tissue (or brain-perfusion) with Magnetic Resonance Imaging (MRI).

An MRI scanner is a unity of complicated electrical systems, software and physical principles that allow an investigator to study the inside of the human body, especially soft tissue. MRI can make a series of images each with different diagnostic information that helps the physician in determining the condition of patients. Furthermore, post processing of a single image or a series of images can reveal additional (diagnostic) information, such as brain activation, functional brain connections, structural brain connections or hemodynamic properties. One of the intriguing facts of MRI is that, in general, the signal for image formation is based on free water molecules, one of life's most essential molecules, whereas each specific MRI technique reflects completely different aspects of the functioning of the brain.

In the human body, water can diffuse freely over the membranes but nutrients have to be supplied by the blood stream. Blood must flow slowly (like in the capillaries) to allow exchange of nutrients. Measuring the blood supply to brain tissue (and thereby indirectly the nutrients supply) is relevant in multiple clinical conditions. An example is measurement of blood supply in a brain tumor in order to asses its (degree of) malignancy. Another example is assessing the extent of tissue at risk following an ischemic stroke. In both conditions, flow measurements have important therapeutic consequences.

This thesis focuses on assessing blood supply to brain tissue using MRI. Chapter 2 is a review on measurements of blood supply to brain tissue and describes two techniques for measuring brain perfusion with MRI. One technique uses a contrast agent to measure the perfusion, the other employs water in the arteries as a label to measure the cerebral blood flow. The other chapters of this thesis focus on perfusion measurements with dynamic susceptibility contrast (DSC-) MRI, which uses gadolinium-based contrast agents and dynamic $T_2^{(*)}$ weighted images.

For DSC-MRI (or bolus tracking MRI) a series of images is acquired during the passage of a bolus contrast agent through the brain up to the point that the contrast agent is equally mixed within the total blood pool. The concentration-time curve (determined using the MR-signal

change) measured in tissue holds the hemodynamic information and the cerebral blood flow and volume can be determined when the input of the microvasculature is a delta (or Dirac) function. Contrast agent is injected in the antecubital vein as a short bolus. Subsequently, the bolus travels through the right side of the heart, the lungs circulation, and the left side of the heart. After the second passage through the heart, the bolus contrast agent enters the oxygen rich arterial stream that supplies the body with oxygen and nutrients. When the bolus reaches the brain-feeding arteries the bolus no longer has a clearly defined beginning and end due to the dispersion in the heart and lungs, and consequently the shape of the concentration profile is no longer the same as at its injection site. For this reason, a reference or calibration measurement close to the brain tissue is required to enable quantification of perfusion. The measurement of the change in concentration contrast agent in a brain-feeding artery is called an arterial input function (AIF) measurement.

A special focus of this thesis lies on how to measure a correct AIF. A correct shape of the AIF is crucial for absolute or even relative perfusion values. A correct peak-height is necessary for absolute perfusion quantification, but an erroneous peak-height in combination with a correct shape of the AIF can still produce correct relative values for cerebral blood flow and volume. Therefore, the first objective should be to measure the correct shape of the AIF, whereas the measurement of the peak-height of the AIF should be considered of secondary importance. Partial volume effects are known to corrupt the shape of the AIF measurement, and a relevant question is: where to select an AIF with a correct shape? Another relevant question is: can an AIF with correct shape also be selected automatically?

We used numerical simulations, modeling physical principles present in AIF measurements, to determine the optimal location for correct AIF measurements near two of the main brain-feeding arteries, the left and right middle cerebral artery. These manual AIF measurements can be performed using the magnitude of the MR signal, which is described in chapter 3, as well as using the phase of the MR signal (see Chapter 4). Phase-based AIF measurements have a number of potential advantages compared to the magnitude-based AIF measurements. Both chapters focus on manual AIF selection within the acquired dataset.

Several research groups have proposed automatic AIF selection procedures, however if the selection criteria do not prevent the inclusion of incorrect AIF measurements the results are not reliable. An additional criterion can improve the reliability of the automatic AIF selection methods or aid manual AIF selection. The proposed criterion is based on tracer kinetic theory and tests whether the AIF measurement has an erroneous shape of the concentration-time curve (see Chapter 5). More specifically, specific shape errors that are normally not detected by the current automatic selection criteria. Most automatic AIF selection procedures focus on selecting local AIF measurements (region specific AIF measurements in small brain-feeding arteries). However, do the local AIF measurements reflect the true concentration-time curve of small arteries? Chapter 6 investigates the question whether automatic local AIF measurement can in theory select the correct AIFs of small brain-feeding arteries.

Finally, we performed and analyzed a DSC-MRI study in patients with migraine to investigate whether interictal perfusion changes occur in the migraine patients, since this has not been convincingly demonstrated yet (see Chapter 7). This thesis concludes with a general discussion in chapter 8, a summary in English and Dutch, as well as a list of publications, Curriculum Vitae and Acknowledgements.

Chapter 2: Measurement of cerebral perfusion using MRI

Egbert JW Bleeker and Matthias JP van Osch

ABSTRACT

Cerebral Perfusion MRI is becoming an increasingly important method for diagnosing and staging brain diseases. Magnetic resonance imaging (MRI) provides the opportunity of combining perfusion imaging with high quality anatomical imaging and is therefore for most brain diseases the modality of choice. Perfusion MRI techniques can be categorized in two different groups based on tracer type. First, Dynamic Susceptibility Contrast (DSC-) MRI is a method based on the injection of an exogenous tracer, a gadolinium-based contrast agent, in the arm vein. By means of fast T_2 or T_2^*-weighted imaging the first passage of the contrast agent through the brain tissue is monitored. The second technique, arterial spin labeling (ASL), is a completely non-invasive technique that employs water protons as an endogenous tracer. In this review, the crucial elements for correct perfusion measurements by DSC-MRI and ASL are discussed. In DSC-MRI, the conversion from signal changes to concentration contrast agent, the arterial input function measurement and the deconvolution method are the most important elements. Whereas in ASL, the efficiency of the labeling method, correction for relaxation processes, and M_0-calibration methods can be considered the most essential components of blood flow quantification.

Published in Imaging in Medicine (2010) Feb; 2(1):41-61

INTRODUCTION

Brain perfusion MRI characterizes the microvascular blood supply of brain tissue. Blood supplies the tissue with oxygen and nutrients and removes waste products. In many brain diseases and pathologies blood supply is altered and therefore perfusion MRI can aid in the diagnosis and staging of different brain diseases and pathologies (1-7). For example, in brain tumors the cerebral blood volume can be used to identify angiogenesis, the formation of new vasculature that enables brain tumors to grow larger than 1-2 mm (8). Perfusion imaging can also be helpful in characterizing the autoregulation of cerebral blood flow. Reduction in perfusion pressure, for example caused by stenosed or occluded brain feeding arteries, is counteracted by vasodilatation of especially the arterioles that reduce the resistance of the microvascular bed, thereby stabilizing blood flow (9, 10). This process of vasodilatation can be monitored by measuring the blood volume. Subsequent lowering of perfusion pressure will result in a reduction of cerebral blood flow (CBF), but by increasing the oxygen extraction, aerobic metabolism can be sustained. Parallel to this microvascular blood flow regulation, collateral blood flow, for example via the Circle of Willis or the leptomeningeal arteries, assists in continuing cerebral blood flow (11-13). Transport times of the blood to the brain tissue provides some insight in the quality of collateral blood flow (14, 15). In acute stroke it is hypothesized that perfusion deficits enable differentiation between penumbra and core of the infarct (16-18). Finally, it is known that in patients with Alzheimer's Disease reduction in cerebral perfusion precedes anatomical changes (19, 20), although the interplay between blood flow, amyloid-β deposition and tangle formation is not completely understood at the moment.

Characterizing cerebral perfusion with MRI requires differentiating static brain tissue from moving blood. This can be performed by introducing a tracer in the blood stream, as first applied in humans by S.S. Kety in the first half of the 20th century (21). The first group of MR perfusion techniques, named Dynamic Susceptibility Contrast (DSC) MRI or first-passage bolus-tracking perfusion MRI, relies also on the injection of an exogenous tracer that for MRI is based on the lanthanum ion gadolinium (22). However, MRI is the only imaging modality that also allows the use of an endogenous tracer for perfusion imaging. This other MR perfusion technique, called arterial spin labeling (ASL), employs RF-pulses to magnetically label proton spins in blood thereby creating an endogenous tracer (23).

Hemodynamic parameters

Brain perfusion can be characterized using several hemodynamic parameters, each reflecting a different physiological element of the blood supply to tissue. The CBF describes the amount of blood supplied to the capillaries in a volume of tissue per minute that is [ml/100 ml of tissue/min] or [ml/100 g of tissue/min]. Measuring CBF can for example be used to grade tumors (24-26) or assess the hemodynamic effect of large vessel occlusions (27-29). The term perfusion is

often solely used for CBF, there are however more metrics characterizing microvascular blood supply.

Cerebral blood volume (CBV) is defined as the amount of blood in a given volume of tissue and is expressed in [ml/ 100 ml of tissue] or [ml / 100 g of tissue]. The CBV is a good marker for vasodilatation and angiogenesis (7, 30) and aids in the differentiation of the penumbra from the core of the infarct in acute stroke (31-33).

The mean transit time (MTT) is the averaged time the blood resides in the capillary bed. The MTT can be used for delineating the penumbra and core of the infarct in stroke patients (6, 33). Furthermore, 1/MTT is an index of local cerebral perfusion pressure (34, 35) and provides therefore essential information on the cerebral autoregulation, for example in carotid occlusive disease.

The bolus arrival time (BAT), the time of arrival (TA) and the time to peak (TTP) are timing parameters related to the large vessel blood transport towards the capillaries and can for instance be used to assess occlusions in brain feeding arteries or collateral flow through the Circle of Willis (15).

DYNAMIC SUSCEPTIBILITY CONTRAST MRI (DSC-MRI)

DSC-MRI measures perfusion using the passage of an exogenous contrast agent through the brain vasculature. The contrast agent is injected in the arm vein and after passing the heart and lungs it passes through the brain (micro-)vasculature, which is dynamically monitored by fast MR imaging. The presence of contrast agent decreases the longitudinal relaxation (T_1) and transverse relaxation (T_2) and disturbs the local magnetic field in and around the vessels. Detection of contrast agent can therefore be based on T_1, T_2, or T_2^*-weighted imaging. T_1 weighted imaging will result in signal enhancement and is frequently used to obtain information about the permeability of the capillaries. This method is known under the name of Dynamic Contrast Enhanced MRI (DCE-MRI), but is beyond the scope of this review and we refer to other articles for more information (36-39). The name Dynamic Susceptibility Contrast MRI is reserved for perfusion measurements based on monitoring the first passage of contrast agent by T_2 or T_2^* weighted imaging. Based on simulations of Knutsson et al., the dynamic scan time should be chosen faster than 1.5 sec/image (40) to enable accurate perfusion quantification. To obtain such a high temporal resolution and still have whole brain coverage at a high resolution, acquisition is performed with fast imaging techniques such as EPI most often in combination with parallel imaging (41, 42). Guidelines for imaging settings used in acute stroke are described by Wintermark (43).

The actual signal drop observed in T_2 and T_2^* weighted magnitude images (see figure 1) is a combination of relaxation effects, diffusion of water protons over the local field changes and, for T_2^* weighted images, dephasing due to the presence of local magnetic field changes (22).

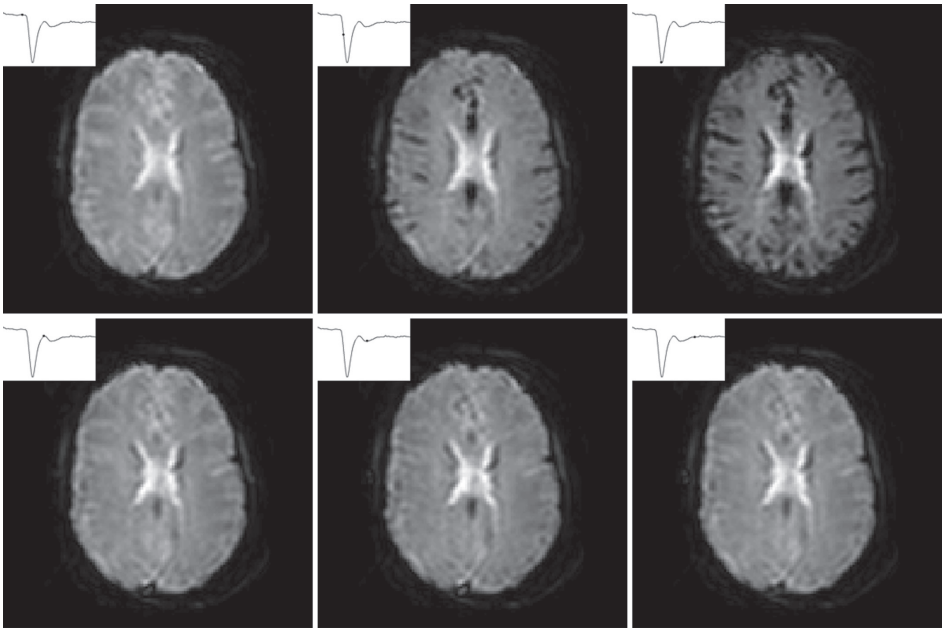

Figure 1: T_2^* weighted PRESTO magnitude images before the contrast agent arrival (top left image) and at several time points during the contrast passage through the brain vasculature. The whole brain average is plotted in the top left corner of every magnitude image with a circle depicting the specific time point for the magnitude image. The signal decrease is especially observed in the gray matter and not so much in the white matter.

The transformation from signal decrease to concentration contrast agent is important for accurate hemodynamic measurements.

Having a correct concentration-time curve of the first passage of contrast agent through brain tissue is, however, not sufficient to calculate the hemodynamic parameters. Three of the hemodynamic parameters (CBF, CBV and MTT see figure 2) can be obtained from the so-called impulse response function, which is mandatory for CBF and MTT estimations. The impulse response is the outcome of the hypothetical experiment of a delta-injection of contrast agent in the brain-feeding artery. It describes the delay and broadening (dispersion) of this delta-injection due to the transport through the vascular network. From tracer kinetic theory, it can be shown that the maximum value of the impulse response function equals the CBF and the area-under-the-curve equals the CBV. However, in clinical practice, the bolus is injected in the arm vein and the shape of the arterial input function (AIF), the concentration profile of a brain-feeding artery, is therefore much broader and is dependent on the subject specific transport properties between the injection site and the AIF measurement location and on the cardiac ejection fraction. The impulse response function can be obtained by deconvolving the tissue response with the AIF.

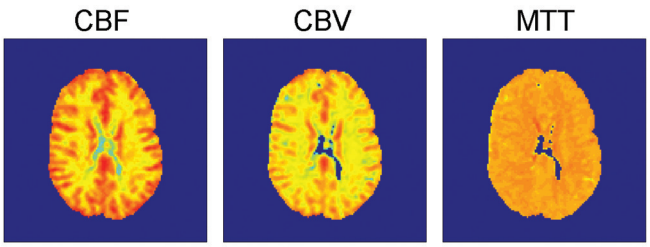

Figure 2: The resulting CBF, CBV and MTT maps after post processing of the data presented in figure 1. The AIF was selected manually and a block circulant SVD was used for the deconvolution. The figure show that the gray matter has a higher CBF and CBV and the MTT is almost the same for gray and white matter.

In summary, DSC-MRI is based on the fast injection of contrast agent in arm vein, whose passage through a brain-feeding artery (AIF) and brain tissue is monitored by fast dynamic MR imaging. Subsequently the MR signal changes are converted to concentration-time curves and a deconvolution is performed; finally, the perfusion parameters are calculated from the impulse response function as based on tracer kinetics.

Contrast agent

Most clinically approved contrast agents consist out of a gadolinium ion (Gd^{3+}) and a chelate to prevent toxic reactions in vivo. The first clinically approved contrast agent was gadolinium-diethylene triamine pentaacetic acid or gadopentetate dimeglumine (Gd-DTPA, Magnevist, Bayer Schering, Berlin, Germany). Since the approval of Gd-DTPA for commercial use in 1988 many new chelates have been developed. DTPA has a linear chemical structure and is ionic (see figure 3). Until recently Gd-DTPA was used most often but recent studies showed that chelates with linear chemical structures have a chance of transmetallation, the uncoupling of the Gd^{3+} with the chelate, which can lead to nephrogenic systemic fibrosis (NSF) in patients with reduced renal function (44, 45). New chelates with a cyclic structure such as gadoteridol (Prohance), gadobutrol (Gadovist) and gadoterate meglumine (Dotarem), (see figure 3) reduce the chance of transmetallation. Furthermore, non-neutral chelates such as gadoterate meglumine bind the

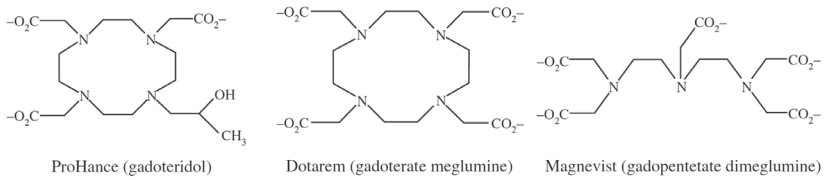

Figure 3: The chemical structure of the chelates gadoteridol, gadoterate meglumine and gadopentetate dimeglumine. The first two chelates have a cyclic structure the third chelate has a linear structure. The first chelate is neutral and the second and third are non-neutral chelates. The second chelates binds gadolinium the strongest compared to the other two chelates.

Gd^{3+} stronger than neutral chelates such as gadoteridol, hereby further reducing the chance of transmetallation.

The concentration gadolinium can be 0.5 mol/l and 1.0 mol/l depending on the product. The increased concentration results in a lower volume to inject in the arm vein and this could lead to a shorter and sharper bolus with a higher peak concentration (46). However, a later study showed no significant difference in peak width when comparing equal doses with different molarities (47).

The effects of the contrast agent on the MR signal are threefold: first, the susceptibility difference of the gadolinium-based contrast agent with blood results in local magnetic field changes in and around vessels. Second, the contrast agent decreases the transverse relaxation time of nearby water protons. Third, the contrast agent decreases the longitudinal relaxation time of nearby water protons.

The intravascular susceptibility is linearly related to the concentration of contrast agent and changes the local magnetic field (48, 49) in and around a vessel. For an infinite cylinder the local magnetic field changes due to the susceptibility difference can be obtained from the Maxwell equations (see also figure 4):

$$\Delta B_{\text{int}} = \frac{\delta\chi \cdot [Gd]}{6}\left(3\cos^2\theta - 1\right)B_0 \qquad [1]$$

$$\Delta B_{ext} = \frac{\delta\chi \cdot [Gd]}{2}\left(\left(\frac{a}{\rho}\right)^2 \sin^2\theta \cdot \cos 2\varphi\right)B_0 \qquad [2]$$

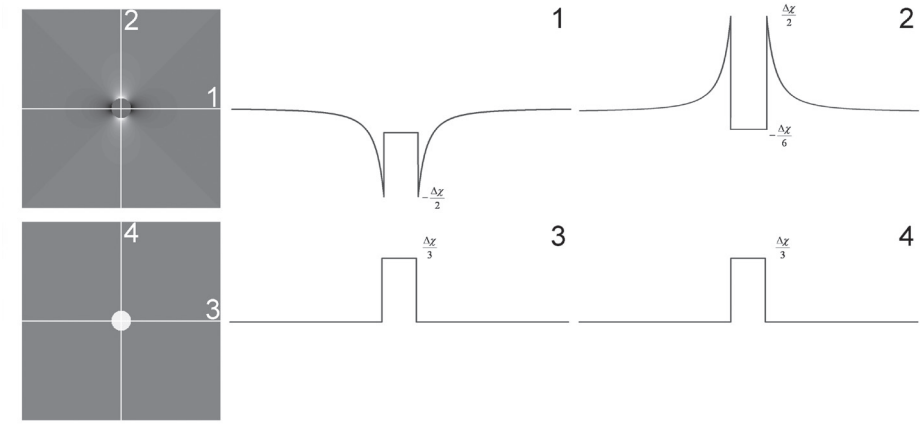

Figure 4: Magnetic field change due to a susceptibility difference in and around an infinite cylinder oriented perpendicular to the main magnetic field (top) and parallel to the main magnetic field (bottom). For the perpendicular oriented cylinder, there is a lobular pattern around the cylinder and a homogenous magnetic field inside the cylinder. For a parallel oriented cylinder, there is only a homogenous magnetic field change inside the cylinder. The subfigures 1 to 4 correspond with the lines 1 to 4 in each of the magnetic field graphs.

where ΔB_{int} is the magnetic field change inside the cylinder, ΔB_{ext} is the magnetic field change outside the cylinder, $\delta\chi$ is the susceptibility difference per mol/l of gadolinium between the interior and exterior compartments, [Gd] is the concentration of gadolinium, a is the radius of the cylinder, ρ is the distance from any given point (p) to the cylinder center, θ is the angle between the cylinder axis and B_0, and φ is the angle of p in the plane perpendicular to the cylinder axis. The interior magnetic field change for a parallel oriented cylinder is twice as strong and opposite of sign of the interior magnetic field change for a perpendicular oriented cylinder. Whereas a parallel cylinder does not change the magnetic field outside the cylinder, magnetic field changes outside the cylinder do occur for other orientations, where a pattern with positive and negative lobes can be observed.

For a voxel in tissue filled with randomly oriented capillaries the signal decrease as observed in T_2^* weighted images is a result of susceptibility effects in and around the capillary network, diffusion through these magnetic field inhomogeneities and relaxation changes inside the vasculature (50). A numerical study by Kjølby et al. showed that the susceptibility effects in the surrounding of the capillaries are the main cause of the signal decrease in the magnitude images (51).

The concentration contrast agent in tissue can be determined by relating the signal intensity of the dynamic $T_2^{(*)}$-weighted images to the signal intensity prior to the arrival of contrast agent. The equilibrium signal relation of gradient echo sequences is as follows:

$$S(t) \propto \frac{\sin\alpha\left(1 - e^{\frac{-TR}{T_1(t)}}\right)e^{\frac{-TE}{T_2^*(t)}}}{1 - \cos\alpha \cdot e^{\frac{-TR}{T_1(t)}}} \qquad [3]$$

where S(t) is the evolution of the magnitude of the MR signal, α is the flip angle, TR is the repetition time, $T_1(t)$ is the longitudinal relaxation time which will decrease during the contrast agent passage, TE is the echo time and $T_2^*(t)$ the transverse relaxation time, which is also dependent on the contrast agent concentration. For sequences insensitive to longitudinal relaxation time changes, this relation simplifies to:

$$S(t) \propto e^{\frac{-TE}{T_2^*(t)}} \qquad [4]$$

When using short TR sequences, like in PRESTO (Principles of echo-shifting with a train of observations) or segmented EPI, T_1-effects of the contrast agent can no longer be neglected when the flip angle is chosen close to the Ernst angle. Such effects do not only lead to erroneous quantitative CBF-values, but also affect relative CBF measurements (52). From theoretical and simulation studies it has been shown that the relation between the concentration contrast agent in brain tissue and ΔR_2^* is linear with relaxivity r_2^*, whereas the ΔR_2 has a slightly non-linear relation with the concentration contrast agent (50, 51, 53, 54). The $\Delta R_2^{(*)}$ is defined as:

$$\Delta R_2^{(*)}(t) \equiv \frac{1}{T_2^{(*)}(t)} - \frac{1}{T_2^{(*)}(0)} = \frac{1}{TE} \ln\left(\frac{S(0)}{S(t)}\right) \quad [5]$$

with S(0) the magnitude signal before contrast agent arrival and $T_2^{(*)}(0)$ the $T_2^{(*)}$ without the presence of contrast agent. When acquiring more echoes, ΔR_2^*-measurements can be obtained that are insensitive to T_1-effects of the contrast agent (55-58). Whereas spin echo sequence are slower, show less signal changes for a certain concentration contrast agent and have a non-linear relationship with the concentration contrast agent, it shows specific sensitivity towards the microvascular bed yielding perfusion maps less affected by large vessel artifacts (53).

Inside brain feeding arteries the relation between the ΔR_2^* and the concentration contrast agent is more complex. In vitro experiments showed that the relation between the ΔR_2^* and the concentration contrast agent in human blood is quadratic and dependent on the hematocrit level (49, 59). This quadratic relation can be explained by the compartmentalization of the contrast agent within blood since the contrast agent remains extracellular. Based on the original Monte Carlo simulation study of Boxerman and co-workers, one might conclude that measurement of concentration contrast agent in or near a large vessel is not possible with spin echo sequences, since these authors showed a vanishing sensitivity towards the presence of contrast agents for vessels larger than 30-50 μm (53). However, based on measurements in pigs, it has been concluded that also for AIF measurements a linear relation exists between ΔR_2 and the concentration contrast agent (60, 61).

Tracer kinetics

The method for determining the hemodynamic parameters CBF, CBV and MTT as measured with DSC-MRI is based on classic tracer kinetic theory as develop by Zierler and excellent reviewed by Lassen (62, 63). The concentration contrast agent in the capillaries c(t) is dependent on the concentration contrast agent in the artery $c_{AIF}(t)$ supplying the blood to the tissue microvasculature (arterial input function (AIF)) and the transport properties of the microvasculature itself. The output of the microvasculature, $c_{out}(t)$, can be expressed as a convolution of the AIF with a blood transport function h(t):

$$c_{out}(t) = \int_{t_0}^{t} h(t-\tau) c_{AIF}(\tau) d\tau \quad [6]$$

The blood transport function h(t) represents the distribution of transit times through the microvasculature. Under the assumption of an intact blood-brain barrier, all contrast agent will leave the microvasculature at some moment and therefore h(t) possesses the following property:

$$\int_0^\infty h(t)dt = 1 \qquad [7]$$

Following the same argument or by integration of equation 6 in time leads to the following relation:

$$\int_{-\infty}^{\infty} c_{out}(t) = \int_{-\infty}^{\infty} c_{AIF}(t) \qquad [8]$$

This is the basis of correction methods for partial volume artifacts of the AIF that rescale the AIF to have the same the area-under-the-curve as the venous output function (64-66). It should however be noted that partial volume effects can also lead to shape changes, which are not corrected for in this approach (see section *AIF measurements*). DSC-MRI does, however, not measure the output of the microvascular system, but the amount of contrast agent still present in tissue. Therefore, it is easier to describe the tracer kinetics in terms of the residue function $\Re$(t), which describes the fraction of the concentration contrast agent that remains in the microvasculature after a delta injection contrast agent at the input of the microvasculature. The tissue residue function is equal to the impulse response normalized to unity. $\Re$(t) can be deduced from h(t):

$$\Re(t) = 1 - \int_0^t h(\tau)d\tau \qquad [9]$$

At the onset, this residue function has a value of one and this becomes zero when the contrast agent has completely washed out. The input to a voxel in the microvasculature ($n_t^{in}(t)$ in mol contrast agent) can be calculated from the AIF, when assuming that the AIF is not delayed nor dispersed during the transport from the location of the AIF-measurements towards the brain tissue:

$$n_t^{in}(t) = f \cdot c_{AIF}(t) \cdot dt \qquad [10]$$

where f is the blood flow in ml/sec at the input of the voxel. The concentration contrast agent of a voxel in tissue is:

$$c_t(t) = \frac{n_t(t)}{V_{voxel}} = \frac{\int_{t_0}^{t} \Re(t-\tau) n_t^{in}(\tau)d\tau}{V_{voxel}} = \frac{f\int_{t_0}^{t} \Re(t-\tau) c_{AIF}(\tau)d\tau}{V_{voxel}} = \frac{f}{V_{voxel}} \cdot \Re(t) \otimes c_{AIF}(t) \qquad [11]$$

where f/V_{voxel} equals the CBF except for some conversion factors.

The CBF can therefore be obtained by means of a deconvolution from the tissue passage curves and the AIF, when keeping in mind that $\Re(0)=1$:

$$CBF \cdot \Re(t) = c_t(t) \otimes^{-1} c_{AIF}(t) \quad [12]$$

When the AIF was actually delayed by TA (time-of-arrival) seconds, then $\Re(t)$ will be zero for t<TA and will reach the value of one at TA sec. Therefore, CBF is in practice not calculated from $\Re(0)$, but as the maximum value of $\Re(t)$:

$$CBF = \max\left(c_t(t) \otimes^{-1} c_{AIF}(t)\right) \quad [13]$$

where as the timepoint of the maximum value of $\Re(t)$ is taken as TA. This method assumes that the applied deconvolution method handles delays correctly. This was not the case for the original SVD method, but recent methods provide delay-insensitive results (67-70).

The CBV can be calculated from the product of the blood flow and the transport time function, comparable to the calculation of distance traveled from the product of velocity and time:

$$CBV = \int_0^\infty CBF \cdot h(t) \cdot t \cdot dt = -\left[CBF \cdot \Re(t) \cdot t\right]_0^\infty + CBF \int_0^\infty \Re(t) dt = CBF \int_0^\infty \Re(t) dt \quad [14]$$

The CBV can also be calculated from the ratio of the areas-under-the-curve of the tissue passage curve and the AIF, although this results in slightly worse quantification due to difficulties in differentiating between the first passage and the recirculation (71). It should be noted that an additional correction for CBF and CBV is used to account for the difference in hematocrit in large (artery) and small (capillary) vessels.

Finally, the MTT of the blood through the capillary network can be calculated by using the central volume theorem, which describes the relation between CBF, CBV and the mean transit time (72, 73):

$$MTT = \frac{CBV}{CBF} \quad [15]$$

As can be seen from equation 14, the MTT can also be calculated by taking the area-under-the-curve of the residue function.

Arterial input function measurements

The AIF measurement is a crucial element for obtaining the hemodynamic parameters CBF, CBV and MTT with DSC-MRI. The AIF represents the concentration in time of the contrast agent through a brain-feeding artery (referred to as concentration-time curve). The concentration-time curve needs a correct shape and the right peak height to provide quantitative values for

CBV, CBF and MTT. If the shape of the AIF is correctly measured, but the height is incorrect, then CBV and CBF will only show correct relative values, but MTT will still be quantitatively correct, since CBV and CBF will scale by the same factor. If the shape of the AIF is incorrect, all perfusion parameters calculated from the impulse response function will be incorrect, although relative CBV values can be obtained from the area-under-the-curve of the tissue response. AIF selection is often performed manually but a number of automatic selection procedures have been proposed based on shape characteristics of a correct AIF, like high peak height, small full-width-half-maximum, low first moment and steep rise (74-76).

Initial approaches to measure the AIF measurement with both correct height and correct shape concentrated on finding voxels located completely inside a brain-feeding artery. In this case a quadratic relaxation rate for magnitude-based AIF measurements should be used and a linear relation for phase-based AIF measurements (49, 59, 77). At an optimal dose and echo time phase-based AIF measurements have increased signal-to-noise ratio (SNR) compared to magnitude-based AIF measurements (78, 79). However, phase-based AIF measurements still require a magnitude-based estimation of the brain tissue response, because the contrast agent induces almost no phase changes in a voxel filled with randomly oriented capillaries (80). Due to the high maximum concentration of the AIF (approximately 15 mM at 1.5 T), the MR signal can drop into noise level, which would corrupt the shape of the concentration-time curve independent of whether the amplitude or the phase of the MR signal is used for the measurement. Reducing the echo time or lowering the contrast agent dose could prevent signal depletion, but both methods would result in a lower SNR of the tissue response measurement. Therefore, dual echo approaches have been proposed with a short echo time for the AIF measurement and a longer echo time for the tissue response (55). An additional advantage of dual echo sequences is that longitudinal relaxation effect can be compensated for (58, 81).

The AIF can theoretically be measured correctly in a voxel located completely within an artery, but due to the limited spatial resolution of DSC-MRI such voxels cannot be found in actual experiments and partial volume effects can therefore not be avoided. Due to mixing of arterial signal with signal from the surrounding tissue, non-linear distortions of the AIF can occur when gradient echo imaging is employed. These distortions occur because the phase evolution of the arterial compartment will differ from the phase evolution in the surroundings, leading to in- and out-of-phase effects depending on the concentration contrast agent. Partial volume effects affect both the magnitude-based and phase-based AIF measurements and can attain different manifestations as shown in figure 5. AIF shape distortions due to partial volume effects can only be corrected for arteries parallel to the main magnetic field, because only in this orientation magnetic field changes are not present in the surrounding tissue when the contrast agent passes through the artery (82) (see figure 4).

Since AIF measurements in voxels located in or near the artery are hampered by these partial volume effects, the AIF is often selected in tissue surrounding the artery. When the artery is not oriented parallel to the main magnetic field, the magnetic field outside the artery will

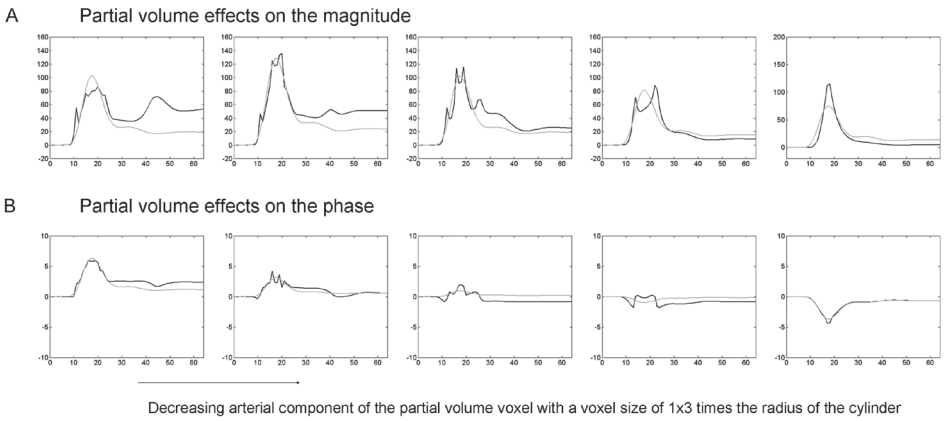

Figure 5: Simulated partial volume effects on AIF measurements for the magnitude-based approach (A) and the phase-based approach (B). These partial volume effects lead to errors in the shape of the AIF measurement. The gray line represents the ground truth scaled to have an equal CBV obtained from the first passage. All profiles are created in noise free simulations.

also change due to the passage of the contrast agent within the vessel. These magnetic field changes lead to changes in the phase and amplitude of the MR-signal of tissue surrounding the vessel, which can therefore be used to estimate the AIF. Voxels located close to the vessel wall but completely outside the artery are unaffected by partial voluming with arterial signal, but show still reasonable large signal changes during the arterial bolus passage. By numerical modeling it has been shown that at specific locations outside an artery a correct measurement of the shape of the AIF can be obtained using either the magnitude or the phase of the MR signal (83-85). A disadvantage of measuring the AIF in tissue surrounding an artery is that such measurements will be affected by the tissue response of the same voxel. Thornton et al. proposed subtraction of the tissue response to improve the magnitude-based AIF measurements (86). Phase-based AIF measurements have almost no tissue response and are therefore very little affected by the tissue passage.

Traditionally, a single (global) AIF is used for all voxels in the brain tissue and such a global AIF is frequently measured in the internal or middle cerebral artery. However, these arteries are located at a relatively large distance from the microvasculature. All dispersion between these arteries, where the AIF is measured and the actual input of the microvasculature, would be incorrectly interpreted as microvascular dispersion and thus lead to quantification errors in the CBF (68). Thijs et al. showed for example that for stroke patients the AIF is best selected on the contralateral side of the infarct (87). Based on the original ideas of Alsop et al., several investigators have looked into the possibility of estimating an individual AIF for every tissue voxel (88). Such 'local' AIFs would much less be affected by dispersion effects. Independent component analysis, factor analysis, and feature extraction have been proposed for obtaining local AIF measurements (88-91). The benefit of reduced dispersion effects for local AIFs comes

with potential disadvantages, such as increased risk of partial volume effects (92) and reduced signal-to-noise.

Deconvolution

A correct AIF and tissue response still require a deconvolution approach to produce the impulse response from which the CBF, CBV and MTT are derived. There are two general approaches for deconvolution: (i) model dependent approaches (93-96) and (ii) model independent approaches (69, 97, 98). The model independent approaches are little dependent to the underlying vasculature but can be sensitive to noise and dispersion of the bolus. Dispersion effects lead in general to an underestimation of CBF and hence an overestimation of MTT (68) the effect of dispersion is excellently reviewed by Calamante (99).

The simplest model employed for model dependent approaches is an exponential decay; this model describes the microvasculature as a single well-mixed compartment. Models that are more complex can describe in some extent delay and dispersion, but with additional parameters fitting the residue function becomes more difficult. Moreover, if the model is different from the true vascular response the obtained hemodynamic parameters have erroneous values.

Currently most post-processing methods of DSC-MRI rely on model independent deconvolution techniques that do not pose restrictions on the shape of the impulse response. A number of different model independent deconvolution approaches have been reported. For example, the SVD and block-circulant SVD (which is a modified version of the SVD in order to make the deconvolution delay insensitive) (67, 69, 70) or the Tikhonov regularization (100). A different approach is the Fourier based deconvolution, where deconvolution is a mere division (97, 101). Deconvolution can also be performed using a statistical approach such as the maximum likelihood estimation maximization (MLEM) and its modified version mMLEM (in order to make the deconvolution less sensitive to delay and dispersion) (98, 102, 103).

All deconvolution methods are susceptible to noise on the tissue response and the AIF. Noise on the concentration profiles can corrupt the outcome of the deconvolution and therefore each deconvolution method employs some kind of filtering, either by spectral filtering (96, 97), cutoff value on the eigenvalues of the matrix inversion (69, 104), or by limiting the number of iterations in iterative methods (98, 102).

ARTERIAL SPIN LABELING (ASL)

Arterial spin labeling is a completely non-invasive perfusion imaging technique that employs water protons as an endogenous tracer to probe the blood supply to tissue (23, 105). Since water transport across the blood brain barrier is relatively unrestricted, water protons are considered diffusible (although not completely freely diffusing) tracers (23, 106-109). Labeling

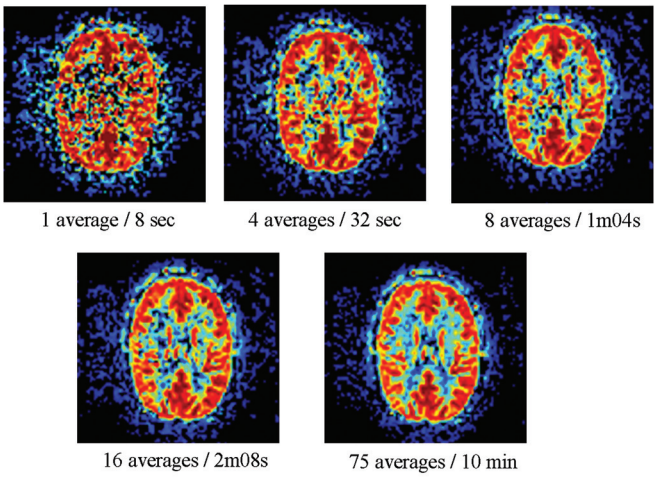

Figure 6: ASL based cerebral blood flow images for different numbers of signal averages. Note that for a single average the gray-white matter contrast already is already evident, whereas 75 averages are necessary for an adequate depiction of the white matter. Acquisition employs pseudo-continuous labeling with a label duration of 1650 msec, a delay of 1515 msec and background suppression.

is performed at the location of the larger brain-feeding arteries such as the internal carotid artery or the basilar artery and after labeling a delay is inserted in the sequence to allow the labeled spins to travel towards the microvasculature. The spin of water protons located in the brain-feeding arteries are either inverted (23) or saturated (110, 111) by a radiofrequency pulse. The imaging performed after the labeling is proton density weighted, having a short echo time, to limit the influence of transverse relaxation. Since such images are not only sensitive to the inflow of labeled spins, but also to signal from static tissue, a second image is acquired without labeling arterial blood. A subtraction of the label from the control image provides an image that is only sensitive to the presence of labeled spins. Such a single subtraction image is, however, of limited quality and therefore 30-60 averages are usually obtained to increase SNR (see figure 6). In the following sections the labeling part, the imaging part, and quantification of the CBF are discussed. Furthermore, ASL provides the possibility to label only a single artery, enabling the possibility to image the flow territory of a single vessel. This has importance in pinpointing the origin of emboli in acute stroke (112), differentiating en passage feeders from direct feeders in arterio-venous malformation, and to understand collateral blood flow in large vessel disease (28, 29, 113, 114). The different approaches of flow territory mapping will also be discussed.

Labeling of arterial blood

Labeling approaches for ASL can be subdivided into three categories: continuous ASL (CASL), pulsed ASL (PASL), and velocity selective ASL (VSASL). These three categories differ based on the temporal layout of the sequence and the spatial extent of the labeling sequence. ASL is a

subtraction technique based on the assumption that the only difference between the label and control image originates from the inflow of labeled spins. When designing a labeling approach it is therefore essential that the influence on the spins in the imaging slices is equal for the label and control module. In this respect, it is essential to avoid magnetization transfer (MT) effects (see next section).

Magnetization transfer effects

All labeling approaches employ slice selective RF pulses to invert or saturate water spins at the labeling location. Whereas water protons in blood have a narrow frequency spectrum, the frequency spectrum of macromolecules in brain tissue is much broader. Therefore, slice selective RF pulses of the labeling module do still affect macromolecular spins even when they are located at a different location along the slice selection gradient and this magnetization can be transferred to the free water signal. When the total power of RF pulses in the labeling part of the sequence differs from the control part, a net difference in magnetization will be created that will show as subtraction errors in the ASL CBF images. For some ASL implementation the

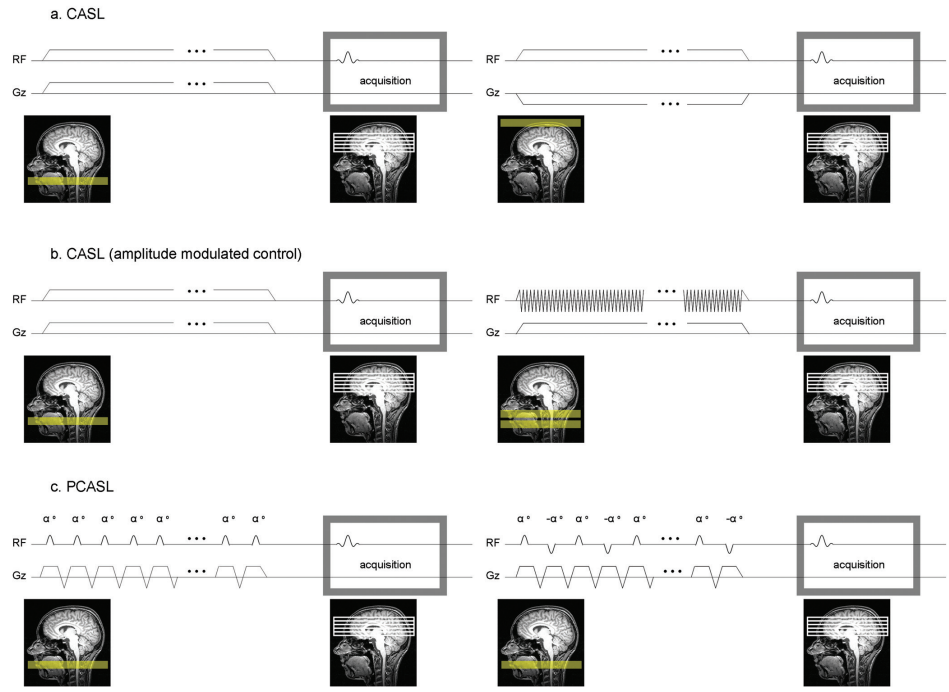

Figure 7: Schematic pulse diagrams for different continuous ASL sequences with schematic images for the labeling slab (yellow) and read-out slices (white). Read-out modules are indicated by gray boxes. Figure a shows the diagram for continuous ASL, figure b shows the pulse diagram for CASL with amplitude modulation control and figure c shows the pulse diagram for pseudo continuous ASL.

occurrence of this type of error is easily tested by labeling superior from the imaging slices instead of the neck region (e.g. in (115)).

Continuous ASL

In continuous ASL labeling is performed using a small labeling plane through the brain-feeding arteries (see figure 7). The water protons that flow through that labeling plane are inverted using a flow driven adiabatic inversion RF pulse in combination with a small gradient in the flow direction (23, 116, 117). The labeling is switched on for a relatively long period of 1.5-2.5 seconds to create sufficient label resulting in a long bolus of labeled blood. Because of the continuous RF pulse, the total RF power is high, thereby potentially leading to severe magnetization transfer effects. To avoid such MT-effects, the control image needs to have the same RF power with minimal effect on the magnetization of arterial blood. Two different approaches have been proposed: the first approach limits the coverage to a single plane, by changing the position of the labeling plane to the other side of the imaging plane. When extending the coverage to more than a single plane, this approach would result in slightly asymmetrical excitation of the macromolecules for the control and the label part, which will lead to subtraction errors. Therefore, a second approach has been proposed that employs amplitude modulation of the RF pulse for the control images to create two inversion planes close to each other, thereby resulting in a double inversion of the blood flowing through these planes. The last approach is at the moment the most common implementation of CASL, although the double inversion plane approach results in a slightly lower labeling efficiency of approximately 80%.

Advantages of CASL are that all spins are labeled at the same level of the arterial tree and that the temporal width of the bolus is determined by the labeling duration. Both characteristics result in a straightforward quantification of the CBF as long as all labeled spin have reached the microvasculature in the imaging volume before the start of the readout (118, 119). Disadvantages of CASL are the difficult implementation of the continuous RF pulse on modern RF amplifiers and the relatively high specific absorption rate (SAR) of the sequence.

Pseudo or pulsed CASL (PCASL) was recently proposed to reduce the demands on the RF amplifier and to lower the SAR while keeping the advantages of CASL (120-122). PCASL splits the continuous RF pulse of CASL into a train of short, slice selective RF pulses that gradually invert the spins of the water protons when combined with a small net gradient along the artery. As control scan, the amplitude of the odd pulses can be inverted or the net gradient can be nulled. It has been shown that the labeling efficiency of PCASL can be higher than the amplitude-modulated CASL implementation, although the sequence is sensitive to off-resonance effects and the efficiency depends on the arterial velocity (120, 122).

Pulsed ASL

The labeling approach in pulsed ASL is fundamentally different from the CASL approach: instead of a temporal long but spatially confined labeling pulse, a short labeling pulse is

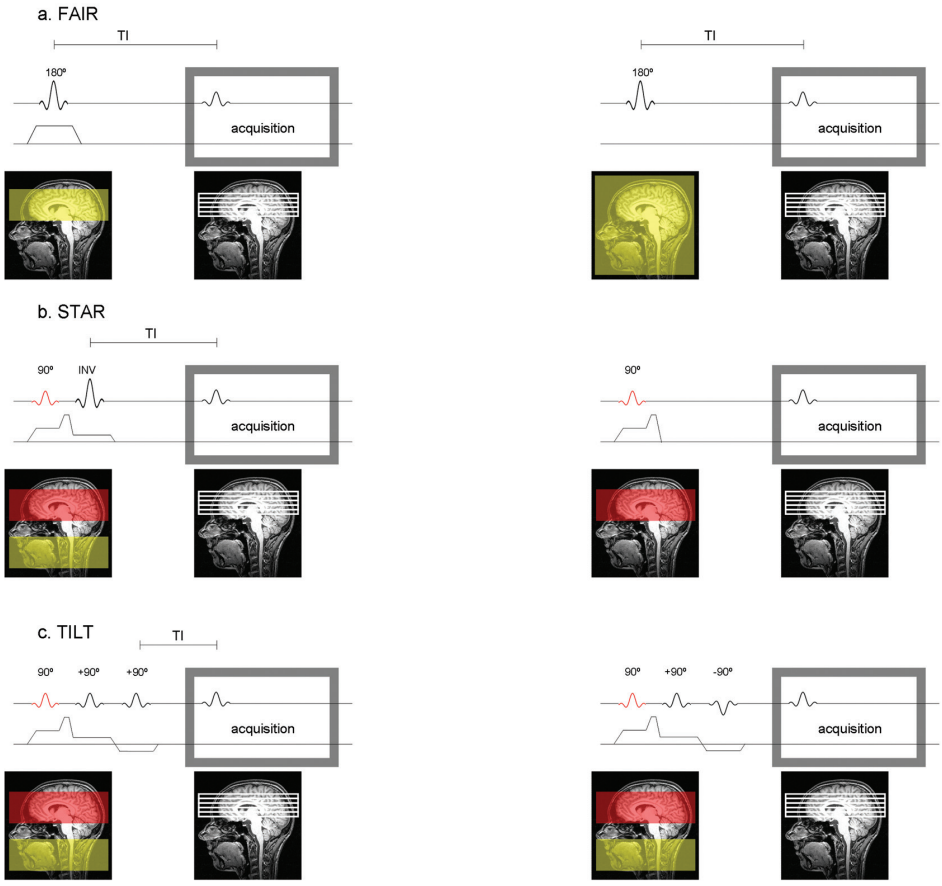

Figure 8: Schematic pulse diagrams for different pulsed ASL sequences indicating the labeling slab in yellow, saturation slab in red and read-out slices in white. Figure a shows the diagram for the FAIR sequence, figure b shows the pulse diagram for the STAR sequence and figure c shows the pulse diagram for the TILT sequence. Both STAR and TILT have a saturation pulse before inversions of the water-protons.

employed over a large region. Although the labeling period is short, in the order of 10-15 msec, still a large amount of spins can be labeled, since a much larger part of the brain-feeding vasculature is labeled. Many different approaches have been proposed for PASL, although in the end all implementations create a situation in which spins proximal to brain vasculature have an opposite magnetization during labeling compared to the control situation (123-133), see also the overview in (134). Three of the best-known PASL sequences are flow-sensitive alternating inversion recovery (FAIR), signal targeting with alternating radiofrequency (STAR) and transfer insensitive labeling technique (TILT) (see figure 8). FAIR employs a slice-selective inversion of the imaging slices as label condition and a non-selective inversion pulse in the control situation. STAR and TILT are both based on a slice selective inversion below the imaging slices, where STAR employs no RF-pulses for the control image and TILT uses a +90 and -90 pulse as control.

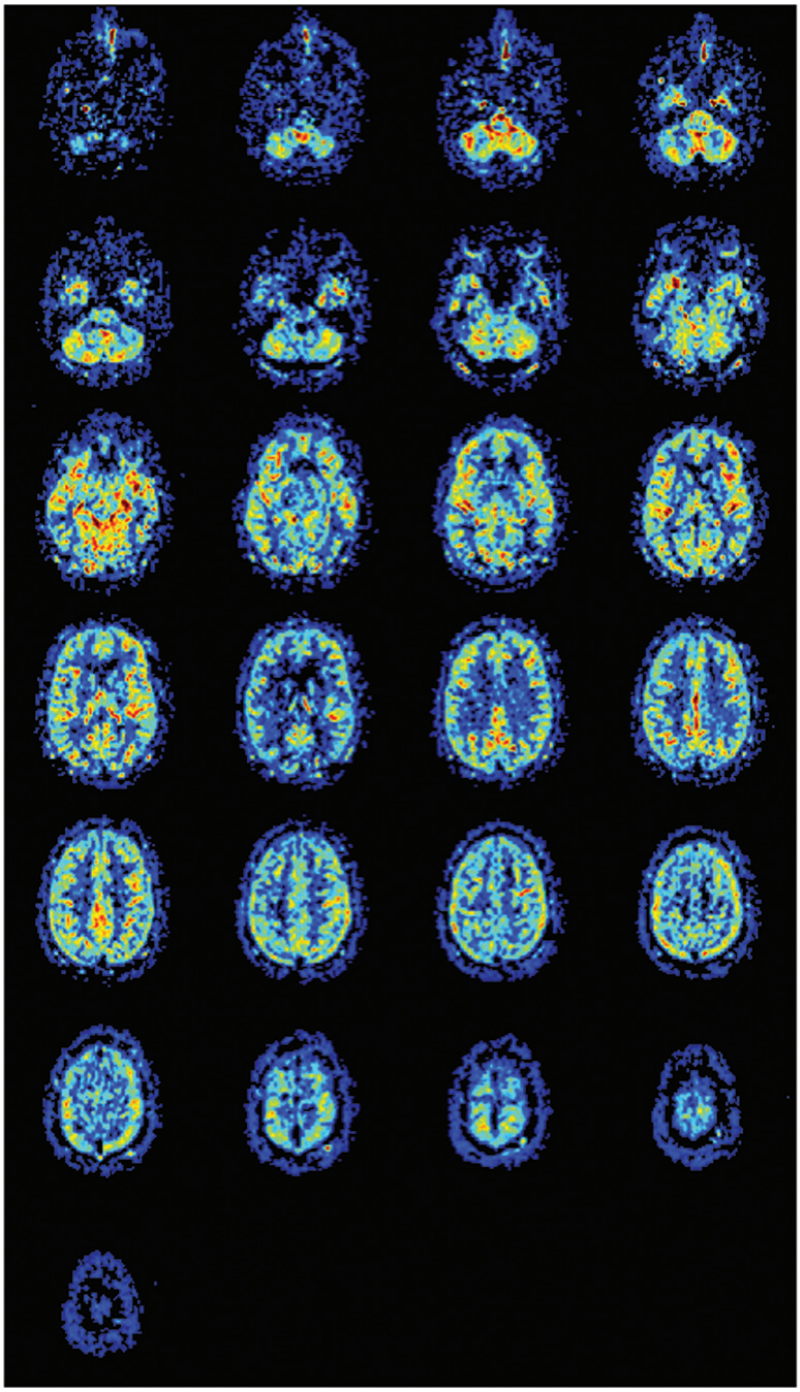

Figure 9: Whole brain perfusion imaging at a resolution of 3x3 mm2 acquired in a total scan time of 4m10s. Acquisition is based on pseudo-continuous ASL at 3 Tesla with 1650 msec label duration, 1525 msec delay, background suppression and a multi-slice single-shot EPI readout module.

Advantages of PASL are the high labeling efficiency and the lower SAR due to the short RF-pulses. Disadvantages are the potentially lower SNR of the CBF-images and difficulties in quantification, because labeling is performed spatially, thereby incorporating a dependency on the layout of the arterial tree.

Velocity selective ASL

Whereas both CASL and PASL differentiate flowing arterial blood from static tissue signal by spatially limiting the labeling to the region below the imaging slice, velocity selective ASL differentiates flowing from stationary spins by employing flow encoding gradients. In the label condition spins that flow faster than approximately 2 cm/sec are saturated, whereas only minimal flow sensitive components are used in the control condition (111). Since arterial blood flow is gradually slowing when flowing from the brain-feeding arteries into the microvasculature and venous blood is accelerating when leaving the microvasculature, this approach enables discrimination of arterial and venous signal. Flow encoding can be performed in the imaging slab thereby labeling the arterial blood much closer to the microvasculature and thus minimizing transport times of the labeled spins. However, comparable to PASL it is ill-defined how much spins are exactly labeled, thereby making accurate quantification difficult.

Read-out approaches for ASL

In principle, any readout sequence can be used for ASL as long as the sequence is predominantly proton density weighted. However, since the combination of labeling and delay-times are time-consuming (at least 1.5 sec), the imaging sequence should enable to acquire all image data after a single (or a few) labeling periods. Single-shot EPI or fast low-angle shot (FLASH) readout sequences are therefore the most commonly used readout protocols (134-136). With the recent advances in gradients performance and the introduction of parallel imaging, it has become feasible to acquire whole brain perfusion images at a resolution of 3x3 mm^2 within a total readout time of 900 msec, thereby resulting in high quality perfusion images in 4 minutes (see figure 9). More recently, the application of True-fast imaging with steady state precession (FISP) as readout module for ASL has been investigated (137-139).

Traditionally, CASL has been frequently combined with spin echo EPI and PASL with gradient echo EPI. However, the choice of readout sequence is not depending on the kind of labeling module, but only on the clinical research question, e.g. lower in the brain spin echo sequences provide better image quality than gradient echo at the expense of slower imaging. Since recently, 3D single (or multishot) acquisition methods (gradient and spin echo, GRASE), have gained much attention, for two reasons: first, 3D sequence have an inherently higher SNR than multi slice sequences and second, all blood flow information is acquired at exactly the same moment (140). This last issue avoids modulation of the blood flow information by different transport times for different slices and enables perfect background suppression for the complete volume (see next section).

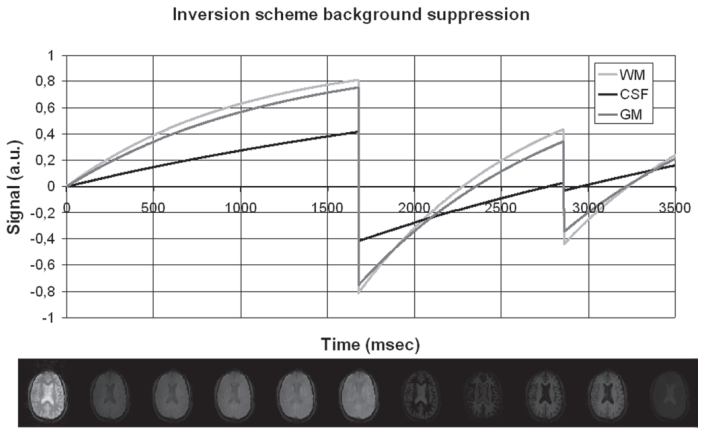

Figure 10: Background suppression using two inversion pulses. White matter (WM), gray matter (GM) and CSF have different longitudinal relaxation values; therefore, the GM relaxes back much faster than CSF. The two inversion pulses are set to specific inversion times to create low signal for both brain tissue and brain fluids during readout of the ASL images. The images below show the effect of the inversion pulses on a single slice.

Background suppression

All implementations of ASL use a subtraction to separate the signal from static tissue from the perfusion signal. Since cerebral blood volume is less than 5%, the perfusion signal is more than a factor of 20 smaller than the signal from static tissue. This implies that a few percent signal fluctuations of the static tissue signal are of same order of magnitude as the perfusion signal. Physiological noise caused by for example the respiratory cycle, can result in such signal fluctuations, thereby degrading the SNR of the ASL. When the relative signal contribution of static tissue and perfusion signal would be more comparable, the influence on the SNR of ASL images of such signal fluctuations would decrease considerably. This is the basis of the so-called background suppression: by including additional non-selective inversion pulses prior to the read-out module, background signal of static tissue can be nulled during acquisition (see figure 10) (141). Although nulling of the background signal would in principle leave exclusively the signal of the labeled spins, nulling of all tissue components cannot be achieved and to avoid uncertainties in the sign of the magnetization of these residual components, a small positive residual signal of approximately 5-10% is aimed for. For multi-slice sequences, background suppression will be optimal for the first slice, but gradual regrow of the static tissue magnetization will result in sub-optimal background signal for subsequent slices.

Quantification of cerebral blood flow by ASL

After subtraction of the label from the control image, an image is obtained that reflects the amount of labeled spins present in the tissue at the moment of imaging. Since MRI provides only arbitrary numbers, the values from the subtraction image should be normalized. This is

often referred to as the M_0-measurement and the different approaches to obtain this calibration factor are discussed below. Although information on the cerebral perfusion is included in the calibrated subtraction image, other factors affect the amount of detected labeled spins, like the input function (that is the amount of labeled spins), loss of label due to longitudinal relaxation while the spins reside in the blood and tissue compartment, loss of signal due to transversal relaxation, imperfect excitation pulses, etc. These different factors will be discussed in the following sections.

M_0 measurement

Quantification of cerebral blood flow by ASL is based upon the idea to create label in brain-feeding arteries and to monitor what brain tissue is fed by this label. Therefore, the signal intensities in the subtraction image should be compared to the signal intensity of pure blood, which is the maximal signal that could be obtained if perfectly created label would fill a complete voxel. The first step in quantification of ASL images is therefore to normalize the signal intensities of the subtraction image by M_0, the signal intensity of pure blood in a proton density sequence. To measure M_0, several approaches have been proposed, all based on measurement of the MR signal intensity in reference areas, like the ventricles, the sagittal sinus, or by employing the signal intensity of the control images as a reference. Except for the sagittal sinus, all other approaches need correction factors to compensate for differences in proton density, for example between cerebral spinal fluid (CSF) and blood (142). When measuring the M_0 of brain tissue in the control images, division by the brain-blood partition coefficient (frequently represented by $\lambda = M_0^{\text{brain tissue}}/M_0^{\text{blood}} \approx 0.9$ (143)) needs to be performed to obtain M_0^{blood}. When using $M_0^{\text{brain tissue}}$ differences in proton density in e.g. gray and white matter or pathology will bias the CBF values, although on the other hand differences in coil sensitivity profiles are automatically compensated for. Measurements in smaller regions-of-interest like the sagittal sinus or the ventricles are known to introduce a considerable amount of noise in the quantification, thereby limiting the usefulness of these calibration methods. Sub-optimal measurement of M_0 is probably still one of the main sources of quantification errors in ASL (144).

Input function of labeled spins

As a second step in the quantification process, the temporal profile of the bolus of labeled spins that leave the labeling area has to be known, which is determined by the labeling efficiency and the temporal-spatial layout of the labeling pulses. Since almost all ASL-methods (except VSASL) create an inversion difference between label and control, the maximum difference between label and control equals two times M_0 (e.g. $+M_0$ versus $-M_0$). For PASL an almost perfect labeling efficiency can be obtained by using adiabatic inversion pulses that provide a proper inversion over a large area, independent of local B_0 and B_1 inhomogeneities (145). However, also such adiabatic inversion pulses do lead to some efficiency losses due to transverse relaxation. For CASL and PCASL the labeling efficiency will be approximately 20% lower and show a slight

dependency on the arterial flow velocity. Estimates of the labeling efficiency, frequently represented by α, have been obtained by using the single slice CASL as reference or by simulations of the Bloch equations (116, 117, 119, 122). Finally, it has recently been proposed to use a separate phase contrast quantitative flow sequence in combination with an estimation of the total brain volume, to estimate the labeling efficiency and thereby normalizing the CBF maps (146). When an estimate of the labeling efficiency is obtained, the difference image is be divided by this factor to correct for the imperfect labeling efficiency.

CASL and PCASL perform the labeling at a single position in the brain feeding arteries for a period of 1-2 sec. This implies that the input function can be considered to be a block-function with an amplitude of α and a temporal width equal to the labeling duration. This width will be equal for all labeled vessels, although α might be variable for different arteries. For PASL the input function is more complicated, since labeling is performed over a much larger region of the arterial tree (see figure 8). The temporal width of the input function when it leaves the upper part of the labeling slab will be determined by the length of the vessels within the labeling slab and the blood velocity therein. The input function will be different for different vessels due to these dependencies. Furthermore, spins that are labeled more proximal in the arterial tree will leave the labeling later and during this transport delay, some label will be lost due to longitudinal relaxation. The input function will therefore have an exponential decreasing shape. Finally, the slice profile of the inversion pulses will modulate the shape of the input function. This can be especially important for the most proximally labeled spins, where the slice profile can be affected by the coil transmit profile (147, 148). Especially due to the uncertainties in the temporal width of the input function in PASL, quantification becomes challenging. To circumvent this issue, three different solutions have been proposed:

1. Wong and co-workers have proposed to cut off the input function by means of a saturation pulse at the labeling location shortly (approximately 800 msec) after the inversion pulse (125). When not all inverted spins have left the labeling slab, this implies that the width of the input function has been fixed to the same duration (e.g. 800 msec). However, the width of the input function would still be undetermined when the saturation pulse is played out too late, e.g. all labeled spins of a certain artery have already left the labeling slab. A correct choice of the timing of the saturation pulse is therefore essential: when chosen too short, only very little spins have been labeled, whereas a too late applied saturation pulse will no longer fix the width of the label bolus. This approach is named QUIPSS-II (quantitative imaging of perfusion using a single subtraction) and can be combined with most PASL approaches. When the saturation pulse is replaced by a train of saturation pulses with a smaller slice thickness, the approach is dubbed Q2TIPS (149).
2. Instead of influencing the shape of the input function, the width can also be estimated by monitoring the signal evolution over time in the brain tissue. In this approach, images are not acquired at a single delay time as is usually performed with ASL, but a series of images with different delay are acquired (118, 131, 150). In such an approach images will

be acquired directly (100 msec) after labeling until most signal is lost (approximately 3000 msec after labeling) at a 150-300 msec interval. Modeling of the signal-time curves results indirectly in an estimate of the width of the input function.

3. Finally, it is possible to incorporate the measurement of the shape of the input function into the ASL sequence (151, 152). This shape can be obtained by subtracting an ASL image with vascular crushing (tissue signal) from an ASL image without crushing of fast flowing spins (tissue plus arterial signal). Since this approach needs to acquire images with and without vascular crushing, the sequence will last longer than conventional approaches. After obtaining the correct shape of the input function, this knowledge is incorporated into the analysis, thereby enabling an improved quantification of the cerebral blood flow.

Transport of the label towards the brain tissue

After leaving the labeling slab, the labeled spins will be transported to the microvasculature. These transport times can be different for different brain regions and may especially vary in patients with vascular occlusive disease. While residing in blood, the label as encoded in the longitudinal magnetization will decay due to longitudinal relaxation. When the transport time is longer than the delay in the sequence not all labeled spins will have arrived in the brain tissue when imaging, leading to an underestimation of the perfusion. Errors due to prolonged transit times are especially prominent in patients with large vessel disease and multi inversion time (TI) approaches have been used to correct for this.

When the capillaries are reached, the label will start to cross the blood-brain barrier and exchange with the brain tissue (109). Finally, label will also leave the tissue into the venous compartment (see figure 11). While the label resides in the brain tissue, it will no longer decay with the T_1 of blood, but with the T_1 of tissue. The fact that decay of label differs in which

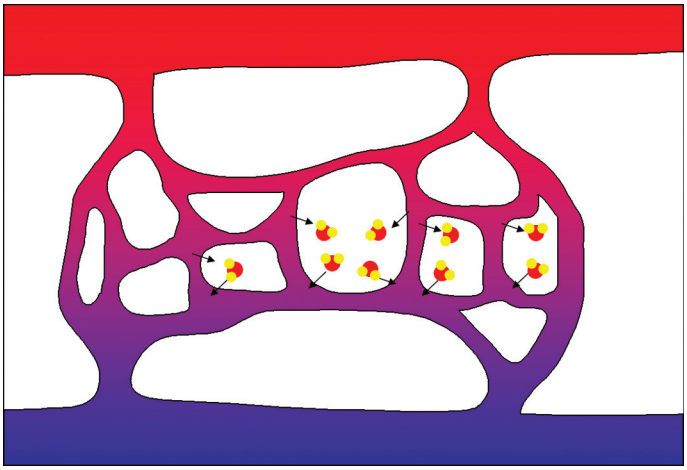

Figure 11: Schematic overview of labeled water protons that will leave the microvasculature and will return into the venous compartment.

compartment the label resides complicates quantification, but fortunately the longitudinal relaxation times of blood and tissue are comparable and most commonly a single T_1 is assumed. However, several researchers have investigated how this assumption affects quantification (106, 107, 109). From these studies, it can be concluded that the error made by this so-called single compartment assumption are smaller for PASL than for CASL and more prominent for white than gray matter for low perfusion values.

Transverse decay of signal

Except for spiral readout approaches, all imaging modules employed in ASL result in T_2 or T_2^* decay of the signal after the excitation pulse (153). Whereas most researchers will assume a single reference value for T_2^* and employ a correction factor when converting the signal intensities to CBF-values, this assumption might breakdown regionally, in pathology, or when monitoring CBF changes upon brain activation. Especially, in the frontal areas and above the petrous bones, magnetic field inhomogeneities result in a much shorter T_2^* than in more homogenous brain tissue (154). This can result in an underestimation of the regional CBF by 30%. In a preliminary study employing a dual echo readout module, we have further shown that T_2^* changes upon activation have only marginal effects in ASL (154). This implies that the ASL-signal originates predominantly from the arterial side of the microvasculature, whereas blood oxygen level dependent (BOLD) effects are on the venous side. Dual echo ASL sequences can therefore be used to monitor simultaneously cerebral blood flow changes (first, short TE) and BOLD (second, long TE) (155, 156).

Taking it all together: the Buxton model

Buxton and co-workers were among the first to describe a model of ASL that includes most terms affecting ASL perfusion quantification. This model was dubbed the general kinetic model, but is recently better known under the name "Buxton-model". The simplest version of the general kinetic model consists of three functions: the input function of labeled spins at the tissue level (c_{input}), the residue function describing how long labeled water molecules will stay in the tissue voxel ($r(t)=\exp(-f \cdot t/\lambda)$), and the magnetization relaxation function ($m(t)=\exp(-t/T_1)$) that describes the loss of label due to longitudinal relaxation. The only difference between PASL and CASL is in the shape of the input function at the entrance of the tissue, reflecting the difference in travel times of labeled water molecules in PASL depending on the localization within the label slab:

$$c_{input} = \begin{cases} 0 & 0 < t < \Delta t \\ \alpha e^{-t/T_1^{blood}} \text{ (PASL)} & \Delta t < t < \Delta t + \tau \\ \alpha e^{-\Delta t/T_1^{blood}} \text{ (CASL)} & \Delta t < t < \Delta t + \tau \\ 0 & t > \tau + \Delta \end{cases}$$

$$\Delta M(t) = 2 \cdot M_0^{blood} \cdot f \cdot c(t) \otimes (r(t) \cdot m(t)) \quad [16]$$

with Δt equaling the transit delay and τ the fresh inflow time (PASL) or labeling duration (CASL or QUIPSS). This model is the basis for multi TI ASL measurements, which is based on fitting Eq. 16 to measured ASL difference signal at multiple delay times.

Imaging artifacts

B_1 variations are especially eminent at medium (3 Tesla) and higher magnetic field strengths (7 Tesla). Any variation in B_1 deposition will result in deviations from the perfect 90° excitation pulse and will result in a modulation of the CBF map. By acquiring images at multiple flip angles, this effect can be corrected for, although at the expense of a time penalty (152). Also, variations in receive profile of the reception coil can result in erroneous CBF-maps, although coil sensitivity profiles are now frequently measured and corrected for as part of the implementation of parallel imaging. Finally, it should be noted that the urge of using fast sequences can result in distortions or blurring of the CBF-maps. By limiting the readout-time of the sequence, for example by parallel imaging, such distortions and blurring can be minimized. Single shot 3D sequences bare the risk of significant blurring in the z-direction due to T_2-decay of the signal during the long readout.

Flow territory imaging

In the last decade, flow territory mapping based on ASL methods have gained much attention, especially since the only alternative for flow territory mapping by ASL is the invasive method of conventional catheter angiography with the associated mortality and morbidity. The principal idea of flow territory mapping, is to restrict the labeling pulses to a single artery, thereby exclusively imaging the tissue supplied by this artery. Several different approaches have been proposed to limit the labeling to a single artery, like:

1. Separate labeling coil
   By positioning a small labeling coil on top of a vessel, the RF is limited to this vessel and the labeling will therefore also be restricted to this artery (157-159). This method is easily implemented, although it relies on separate hardware and yield only limited flexibility in which arteries can be labeled during a single session.
2. Tilting of labeling plane

Whereas traditionally ASL labeling planes are always in the transverse orientation, this labeling plane can also be tilted and positioned in such a way that only a single vessel is labeled (129, 160) . After tilting the labeling plane, the plane could intersect with the imaging slices and therefore it is essential that saturation pulses before and after labeling are included in the sequence to circumvent artifacts in the subtraction images. Secondly, it can be challenging to plan this tilted plane in such a way that only a single vessel is labeled. This method is therefore mainly used to differentiate between left and right internal carotid artery flow territories and posterior circulation.

3. For CASL and PCASL the gradient in the flow direction of vessel can be rotated during labeling to limit labeling to a single spot in the labeling plane (161). This approach enables superselective labeling of the smallest vessels. For CASL this method can result in artifacts in the imaging slices, but for PCASL this issue does not occur, since the rotating gradients are played in between the RF-pulses (162).
4. Wong and co-workers have developed a plannings-free method for flow territory mapping, that is based on the acquisition of four or more images with different labeling distribution over the different brain feeding arteries (see figure 12) (163-166). The first two images are the control and label images of a normal ASL experiments and a subtraction of these two images results in a normal non-selective perfusion map. In the following images the labeling efficiency is varied in the right-left or anterior-posterior (or any other) direction (see figure 12b and c). Subtraction of these images from the control image and normalizing with respect to non-selective perfusion map, results in a relative labeling efficiency map. Based on clustering methods regions are identified that have comparable relative labeling efficiency independent of how the labeling efficiency of the arteries is changed.

CONCLUDING REMARKS AND FUTURE PERSPECTIVE

Both DSC-MRI and ASL are becoming important tools in the radiological clinic and both perfusion methods are considered essential for many different clinical indications, like brain tumors and acute stroke. Furthermore, ASL is starting to play an important role in psychological research since it enables positron emission tomography (PET)-like studies of the cognitive state of subjects. Both methods will continue to benefit from hardware improvements, like techniques for parallel transmission and reception, improved coil design and higher magnetic field strengths. These developments will continue to provide improved new insights in the cerebral hemodynamics. In the coming years quantification of cerebral perfusion will remain the most challenging part of both MRI techniques and more research is definitely needed to obtain absolute quantification of CBF and CBV. Finally, it is anticipated that reactivity measurements, that is relative blood flow changes upon a vasodilatory challenge such as acetazolamide or breath-holding will improve the hemodynamic characterization of neurodegenerative disease.

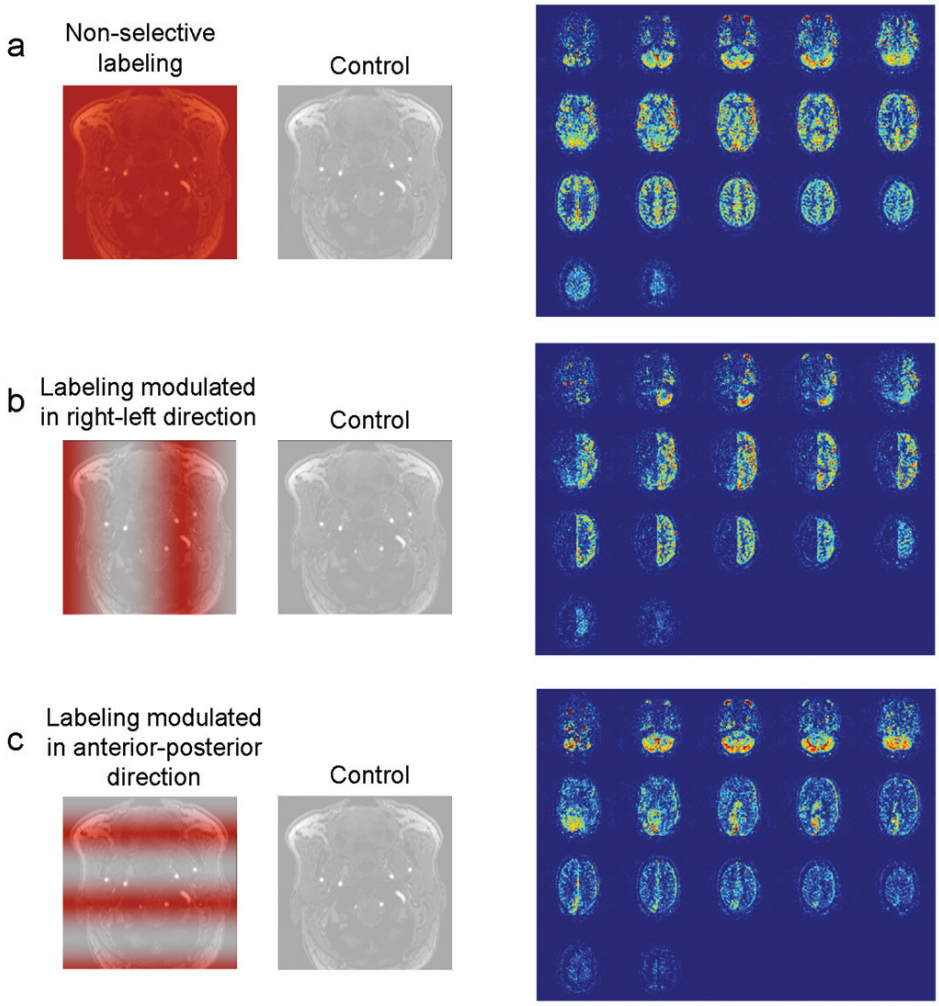

Figure 12: Overview of plannings-free flow territory mapping. A normal ASL experiment (see a) consisting of a non-selective label (red) and a control (white) image, results in a global perfusion image (right pane of a). Subtraction of an image in which the labeling was modulated in the right-left direction (figure b) or anterior-posterior direction (figure c) from the control image results in vessel specific perfusion images. After a subsequent clustering step, the flow territories can be identified.

REFERENCES

1. Christensen S, Mouridsen K, Wu O, Hjort N, Karstoft H, Thomalla G, Rother J, Fiehler J, Kucinski T, Ostergaard L. Comparison of 10 Perfusion MRI Parameters in 97 Sub-6-Hour Stroke Patients Using Voxel-Based Receiver Operating Characteristics Analysis. Stroke 2009.
2. Emblem KE, Zoellner FG, Tennoe B, Nedregaard B, Nome T, Due-Tonnessen P, Hald JK, Scheie D, Bjornerud A. Predictive modeling in glioma grading from MR perfusion images using support vector machines. Magnetic Resonance in Medicine 2008;60(4):945-952.
3. Lemort M, Canizares-Perez AC, Van der Stappen A, Kampouridis S. Progress in magnetic resonance imaging of brain tumours. Current Opinion in Oncology 2007;19(6):616-622.
4. Provenzale JM, Shah K, Patel U, McCrory DC. Systematic review of CT and MR perfusion imaging for assessment of acute cerebrovascular disease. American Journal of Neuroradiology 2008;29(8):1476-1482.
5. Theberge J. Perfusion magnetic resonance imaging in psychiatry. Top Magn Reson Imaging 2008;19(2):111-130.
6. Wintermark M, Fiebach J. Iodinated and gadolinium contrast media in computed tomography (CT) and magnetic resonance (MR) stroke imaging. Current Medicinal Chemistry 2006;13(22):2717-2723.
7. Aronen HJ, Perkio J. Dynamic susceptibility contrast MRI of gliomas. Neuroimaging Clinics of North America 2002;12(4):501-+.
8. Folkman J, Klagsbrun M. Angiogenic Factors. Science 1987;235(4787):442-447.
9. Derdeyn CP, Videen TO, Yundt KD, Fritsch SM, Carpenter DA, Grubb RL, Powers WJ. Variability of cerebral blood volume and oxygen extraction: stages of cerebral haemodynamic impairment revisited. Brain 2002;125(Pt 3):595-607.
10. Derdeyn CP, Powers WJ, Grubb RLJ. Hemodynamic effects of middle cerebral artery stenosis and occlusion. AJNR Am J Neuroradiol 1998;19(8):1463-1469.
11. Liebeskind DS. Collateral circulation. Stroke 2003;34(9):2279-2284.
12. Hendrikse J, Hartkamp MJ, Hillen B, Mali WP, van der Grond J. Collateral Ability of the Circle of Willis in Patients With Unilateral Internal Carotid Artery Occlusion: Border Zone Infarcts and Clinical Symptoms. Stroke 2001;32(12):2768-2773.
13. Rutgers DR, Klijn CJ, Kappelle LJ, Van Huffelen AC, van der Grond J. A longitudinal study of collateral flow patterns in the circle of Willis and the ophthalmic artery in patients with a symptomatic internal carotid artery occlusion. Stroke 2000;31(8):1913-1920.
14. van Osch MJ, Jansen PA, Vingerhoets RW, van der Grond J. Association between supine cerebral perfusion and symptomatic orthostatic hypotension. Neuroimage 2005;27(4):789-794.
15. Thomalla GJ, Kucinski T, Schoder V, Fiehler J, Knab R, Zeumer H, Weiller C, Rother J. Prediction of malignant middle cerebral artery infarction by early perfusion- and diffusion-weighted magnetic resonance imaging. Stroke 2003;34(8):1892-1899.
16. Sorensen AG, Buonanno FS, Gonzalez RG, Schwamm LH, Lev MH, Huang Hellinger FR, Reese TG, Weisskoff RM, Davis TL, Suwanwela N, Can U, Moreira JA, Copen WA, Look RB, Finklestein SP, Rosen BR, Koroshetz WJ. Hyperacute stroke: evaluation with combined multisection diffusion-weighted and hemodynamically weighted echo-planar MR imaging. Radiology 1996;199(2):391-401.
17. Kucharczyk J, Mintorovitch J, Asgari HS, Moseley ME. Diffusion/perfusion MR imaging of acute cerebral ischemia. Magn Reson Med 1991;19(2):311-315.
18. Moseley ME, Kucharczyk J, Mintorovitch J, Cohen Y, Kurhanewicz J, Derugin N, Asgari H, Norman D. Diffusion-weighted MR imaging of acute stroke: correlation with T2-weighted and magnetic susceptibility-enhanced MR imaging in cats. AJNR Am J Neuroradiol 1990;11(3):423-429.
19. Drzezga A, Lautenschlager N, Siebner H, Riemenschneider M, Willoch F, Minoshima S, Schwaiger M, Kurz A. Cerebral metabolic changes accompanying conversion of mild cognitive impairment into Alzheimer's disease: a PET follow-up study. Eur J Nucl Med Mol Imaging 2003;30(8):1104-1113.

20. de Leon MJ, Convit A, Wolf OT, Tarshish CY, DeSanti S, Rusinek H, Tsui W, Kandil E, Scherer AJ, Roche A, Imossi A, Thorn E, Bobinski M, Caraos C, Lesbre P, Schlyer D, Poirier J, Reisberg B, Fowler J. Prediction of cognitive decline in normal elderly subjects with 2-[(18)F]fluoro-2-deoxy-D-glucose/poitron-emission tomography (FDG/PET). Proc Natl Acad Sci U S A 2001;98(19):10966-10971.
21. Kety SS. Quantitative measurement of cerebral blood flow in man. Meth Med Res 1948;1:204-217.
22. Villringer A, Rosen BR, Belliveau JW, Ackerman JL, Lauffer RB, Buxton RB, Chao YS, Wedeen VJ, Brady TJ. Dynamic Imaging with Lanthanide Chelates in Normal Brain - Contrast Due to Magnetic-Susceptibility Effects. Magnetic Resonance in Medicine 1988;6(2):164-174.
23. Williams DS, Detre JA, Leigh JS, Koretsky AP. Magnetic-Resonance-Imaging of Perfusion Using Spin Inversion of Arterial Water. Proceedings of the National Academy of Sciences of the United States of America 1992;89(1):212-216.
24. Warmuth C, Gunther M, Zimmer C. Quantification of blood flow in brain tumors: Comparison of arterial spin labeling and dynamic susceptibility-weighted contrast-enhanced MR imaging. Radiology 2003;228(2):523-532.
25. Provenzale JM, Mukundan S, Barboriak DP. Diffusion-weighted and perfusion MR imaging for brain tumor characterization and assessment of treatment response. Radiology 2006;239(3):632-649.
26. Wolf RL, Wang JJ, Wang SM, Melhem ER, O'Rourke DM, Judy KD, Detre JA. Grading of CNS neoplasms using continuous arterial spin labeled perfusion MR imaging at 3 tesla. Journal of Magnetic Resonance Imaging 2005;22(4):475-482.
27. Bokkers RPH, van der Worp HB, Mali WPTM, Hendrikse J. Noninvasive MR imaging of cerebral perfusion in patients with a carotid artery stenosis. Neurology 2009;73(11):869-875.
28. van Laar PJ, van der Grond J, Bremmer JP, Klijn CJM, Hendrikse J. Assessment of the Contribution of the External Carotid Artery to Brain Perfusion in Patients With Internal Carotid Artery Occlusion. Stroke 2008;39(11):3003-3008.
29. van Laar PJ, Hendrikse J, Klijn CJM, Kappelle LJ, van Osch MJP, van der Grond J. Symptomatic carotid artery occlusion: Flow territories of major brain-feeding arteries. Radiology 2007;242(2):526-534.
30. Paulson ES, Schmainda KM. Comparison of Dynamic Susceptibility-weighted Contrast-enhanced MR Methods: Recommendations for Measuring Relative Cerebral Blood Volume in Brain Tumors. Radiology 2008;249(2):601-613.
31. Kluytmans M, van Everdingen KJ, Kappelle LJ, Ramos LMP, Viergever MA, van der Grond J. Prognostic value of perfusion- and diffusion-weighted MR imaging in first 3 days of stroke. European Radiology 2000;10(9):1434-1441.
32. Wu O, Christensen S, Hjort N, Dijkhuizen RM, Kucinski T, Fiehler J, Thomalla G, Rother J, Ostergaard L. Characterizing physiological heterogeneity of infarction risk in acute human ischaemic stroke using MRI. Brain 2006;129(Pt 9):2384-2393.
33. Sorensen AG, Copen WA, Ostergaard L, Buonanno FS, Gonzalez RG, Rordorf G, Rosen BR, Schwamm LH, Weisskoff RM, Koroshetz WJ. Hyperacute stroke: simultaneous measurement of relative cerebral blood volume, relative cerebral blood flow, and mean tissue transit time. Radiology 1999;210:519-527.
34. Ferrari M, Wilson DA, Hanley DF, Traystman RJ. Effects of Graded Hypotension on Cerebral Blood-Flow, Blood-Volume, and Mean Transit-Time in Dogs. American Journal of Physiology 1992;262(6):H1908-H1914.
35. Schumann P, Touzani O, Young AR, Morello R, Baron JC, MacKenzie ET. Evaluation of the ratio of cerebral blood flow to cerebral blood volume as an index of local cerebral perfusion pressure. Brain 1998;121 (Pt 7):1369-1379.
36. Tofts PS, Brix G, Buckley DL, Evelhoch JL, Henderson E, Knopp MV, Larsson HB, Lee TY, Mayr NA, Parker GJ, Port RE, Taylor J, Weisskoff RM. Estimating kinetic parameters from dynamic contrast-enhanced T(1)-weighted MRI of a diffusable tracer: standardized quantities and symbols. J Magn Reson Imaging 1999;10(3):223-232.

37. Aksoy FG, Lev MH. Dynamic contrast-enhanced brain perfusion imaging: technique and clinical applications. Semin Ultrasound CT MR 2000;21(6):462-477.
38. Covarrubias DJ, Rosen BR, Lev MH. Dynamic magnetic resonance perfusion imaging of brain tumors. Oncologist 2004;9(5):528-537.
39. Essig M, Weber MA, von Tengg-Kobligk H, Knopp MV, Yuh WT, Giesel FL. Contrast-enhanced magnetic resonance imaging of central nervous system tumors: agents, mechanisms, and applications. Top Magn Reson Imaging 2006;17(2):89-106.
40. Knutsson L, Stahlberg F, Wirestam R. Aspects on the accuracy of cerebral perfusion parameters obtained by dynamic susceptibility contrast MRI: a simulation study. Magnetic Resonance Imaging 2004;22(6):789-798.
41. Pruessmann KP, Weiger M, Scheidegger MB, Boesiger P. SENSE: Sensitivity encoding for fast MRI. Magnetic Resonance in Medicine 1999;42(5):952-962.
42. Griswold MA, Jakob PM, Heidemann RM, Nittka M, Jellus V, Wang JM, Kiefer B, Haase A. Generalized Autocalibrating Partially Parallel Acquisitions (GRAPPA). Magnetic Resonance in Medicine 2002;47(6):1202-1210.
43. Wintermark M, Albers GW, Alexandrov AV, Alger JR, Bammer R, Baron JC, Davis S, Demaerschalk BM, Derdeyn CP, Donnan GA, Eastwood JD, Fiebach JB, Fisher M, Furie KL, Goldmakher GV, Hacke W, Kidwell CS, Kloska SP, Kohrmann M, Koroshetz W, Lee TY, Lees KR, Lev MH, Liebeskind DS, Ostergaard L, Powers WJ, Provenzale J, Schellinger P, Silbergleit R, Sorensen AG, Wardlaw J, Warach S. Acute stroke imaging research roadmap. Stroke 2008;39(5):1621-1628.
44. Idee JM, Port M, Medina C, Lancelot E, Fayoux E, Ballet S, Corot C. Possible involvement of gadolinium chelates in the pathophysiology of nephrogenic systemic fibrosis: A critical review. Toxicology 2008;248(2-3):77-88.
45. Thomsen HS, Marckmann P, Logager VB. Update on Nephrogenic Systemic Fibrosis. Magnetic Resonance Imaging Clinics of North America 2008;16(4):551-+.
46. Tombach B, Benner T, Reimer P, Schuierer G, Fallenberg EM, Geens V, Wels T, Sorensen AG. Do highly concentrated gadolinium chelates improve MR brain perfusion imaging? Intraindividually controlled randomized crossover concentration comparison study of 0.5 versus 1.0 mol/L gadobutrol. Radiology 2003;226(3):880-888.
47. Thilmann O, Larsson EM, Bjorkman-Burtscher IM, Stahlberg F, Wirestam R. Comparison of contrast agents with high molarity and with weak protein binding in cerebral perfusion imaging at 3 T. Journal of Magnetic Resonance Imaging 2005;22(5):597-604.
48. Haacke EM., Brown RW, Thompson MR, Venkatesan R. MRI: basic principles and application. New York, USA: Wiley; 1999.
49. van Osch MJ, Vonken EJ, Viergever MA, van der Grond J, Bakker CJ. Measuring the arterial input function with gradient echo sequences. Magn Reson Med 2003;49(6):1067-1076.
50. Kiselev VG. On the theoretical basis of perfusion measurements by dynamic susceptibility contrast MRI. Magn Reson Med 2001;46(6):1113-1122.
51. Kjolby BF, Ostergaard L, Kiselev VG. Theoretical model of intravascular paramagnetic tracers effect on tissue relaxation. Magn Reson Med 2006;56(1):187-197.
52. Calamante F, Vonken EJ, van Osch MJ. Contrast agent concentration measurements affecting quantification of bolus-tracking perfusion MRI. Magn Reson Med 2007;58(3):544-553.
*53. Boxerman JL, Hamberg LM, Rosen BR, Weisskoff RM. MR contrast due to intravascular magnetic susceptibility perturbations. Magn Reson Med 1995;34:555-566.

One of the first in depth analyses of the relation between contrast agent concentration and △R2(*). This paper is based on Monte Carlo simulations and shows the sensitivity of spin echo imaging towards the microvasculature and the risk of vascular artifacts when using gradient echo imaging.

54. Jensen JH, Chandra R. NMR relaxation in tissues with weak magnetic inhomogeneities. Magn Reson Med 2000;44(1):144-156.

55. Perman WH, Gado MH, Larson KB, Perlmutter JS. Simultaneous MR acquisition of arterial and brain signal-time curves. Magn Reson Med 1992;28:74-83.
56. Newbould RD, Skare ST, Jochimsen TH, Alley MT, Moseley ME, Albers GW, Bammer R. Perfusion mapping with multiecho multishot parallel imaging EPI. Magn Reson Med 2007;58(1):70-81.
57. Zaharchuk G, Bammer R, Straka M, Newbould RD, Rosenberg J, Olivot JM, Mlynash M, Lansberg MG, Schwartz NE, Marks MM, Albers GW, Moseley ME. Improving dynamic susceptibility contrast MRI measurement of quantitative cerebral blood flow using corrections for partial volume and nonlinear contrast relaxivity: A xenon computed tomographic comparative study. J Magn Reson Imaging 2009;30(4):743-752.
58. Vonken EJ, van Osch MJ, Bakker CJ, Viergever MA. Measurement of cerebral perfusion with dual-echo multi-slice quantitative dynamic susceptibility contrast MRI. J Magn Reson Imaging 1999;10(2):109-117.
59. Akbudak, E, Hsu, RM, Li, Y, and Conturo, TE. ΔR2* or Δφ contrast agent perfusion effects in blood: quantitation and linearity assessment. In:Proceedings of the ISMRM 6th Annual Meeting, Sydney, 1998, p1197.
60. Porkka L, Neuder M, Hunter G, Weisskoff RM, Belliveau J, Rosen BR. Arterial input function measurement with MRI. 1991. Proc 10th Annual Meeting SMRM San Francisco p120.
61. Sorensen AG, Reimer P. Perfusion imaging: Principles and current applications. Stuttgart, Germany: Georg Thieme Verlag ; 2000.
62. Zierler KL. Theoratical basis of indicator-dilution methods for measuring flow and volume. Circ Res 1962;10:393-407.
*63. Lassen NA, Perl W. Tracer Kinetic Methods in Medical Physiology. New York: Raven Press; 1979.
Excellent book describing tracer kinetic theory. All different layouts of vascular beds and injection of contrast agent are discussed, like single input - multiple output systems, multiple input and output systems, bolus injection, slow injection, etc.
64. Lin W, Celik A, Derdeyn C, An H, Lee Y, Videen T, Ostergaard L, Powers WJ. Quantitative measurements of cerebral blood flow in patients with unilateral carotid artery occlusion: a PET and MR study. J Magn Reson Imaging 2001;14(6):659-667.
65. Knutsson L, Borjesson S, Larsson EM, Risberg J, Gustafson L, Passant U, Stahlberg F, Wirestam R. Absolute quantification of cerebral blood flow in normal volunteers: correlation between Xe-133 SPECT and dynamic susceptibility contrast MRI. J Magn Reson Imaging 2007;26(4):913-920.
66. van de Schaaf, I, Vonken EJ, Waaijer A, Velthuis B, Quist M, van Osch T. Influence of partial volume on venous output and arterial input function. AJNR Am J Neuroradiol 2006;27(1):46-50.
67. Smith MR, Lu H, Trochet S, Frayne R. Removing the effect of SVD algorithmic artifacts present in quantitative MR perfusion studies. Magn Reson Med 2004;51(3):631-634.
*68. Calamante F, Gadian DG, Connelly A. Delay and dispersion effects in dynamic susceptibility contrast MRI: Simulations using singular value decomposition. Magnetic Resonance in Medicine 2000;44(3):466-473.
Article demonstrating the errors resulting from delay and dispersion of the arterial input function on quantitative perfusion imaging by DSC-MRI.
*69. Ostergaard L, Weisskoff RM, Chesler DA, Gyldensted C, Rosen BR. High resolution measurement of cerebral blood flow using intravascular tracer bolus passages .1. Mathematical approach and statistical analysis. Magnetic Resonance in Medicine 1996;36(5):715-725.
Article provides the background theory of DSC-MRI with a special focus on the different deconvolution approaches.
70. Wu O, Ostergaard L, Weisskoff RM, Benner T, Rosen BR, Sorensen AG. Tracer arrival timing-insensitive technique for estimating flow in MR perfusion-weighted imaging using singular value decomposition with a block-circulant deconvolution matrix. Magnetic Resonance in Medicine 2003;50(1):164-174.
71. Perkio J, Soinne L, Ostergaard L, Helenius J, Kangasmaki A, Martinkauppi S, Salonen O, Savolainen S, Kaste M, Tatlisumak T, Aronen HJ. Abnormal intravoxel cerebral blood flow heterogeneity in human

ischemic stroke determined by dynamic susceptibility contrast magnetic resonance imaging. Stroke 2005;36(1):44-49.
72. Meier P, Zierler KL. On the Theory of the Indicator-Dilution Method for Measurement of Blood Flow and Volume. Journal of Applied Physiology 1954;6(12):731-744.
73. Stewart GN. Researches on the circulation time in organs and on the influences which affect it. Part I-III. J Physiolo (London) 1894;15:1.
74. Carroll TJ, Rowley HA, Haughton VM. Automatic calculation of the arterial input function for cerebral perfusion imaging with MR imaging. Radiology 2003;227(2):593-600.
75. Mouridsen K, Christensen S, Gydensted L, Ostergaard L. Automatic selection of arterial input function using cluster analysis. Magnetic Resonance in Medicine 2006;55(3):524-531.
76. Murase K, Shinohara M, Yamazaki Y, Kikuchi K, Miki H, Ikezoe J. Automated extraction of arterial input function from dynamic susceptibility contrast-enhanced magnetic resonance image using independent component analysis for quantification of cerebral blood flow. Radiology 2001;221:163.
77. Akbudak E, Conturo TE. Arterial input functions from MR phase imaging. Magnetic Resonance in Medicine 1996;36(6):809-815.
78. Kotys MS, Akbudak E, Markham J, Conturo TE. Precision, signal-to-noise ratio, and dose optimization of magnitude and phase arterial input functions in dynamic susceptibility contrast MRI. Journal of Magnetic Resonance Imaging 2007;25(3):598-611.
79. Conturo TE, Akbudak E, Kotys MS, Chen ML, Chun SJ, Hsu RM, Sweeney CC, Markham J. Arterial input functions for dynamic susceptibility contrast MRI: Requirements and signal options. J Magn Reson Imaging 2005.
80. Conturo TE, Barker PB, Mathews VP, Monsein LH, Bryan RN. MR imaging of cerebral perfusion by phase-angle reconstruction of bolus paramagnetic-induced frequency shifts. Magn Reson Med 1992;27(2):375-390.
81. Vonken EJPA, van Osch MJP, Bakker CJG, Viergever MA. Simultaneous quantitative cerebral perfusion and Gd-DTPA extravasation measurement with dual-echo dynamic susceptibility contrast MRI. Magnetic Resonance in Medicine 2000;43(6):820-827.
82. van Osch MJP, van der Grond J, Bakker CJG. Partial volume effects on arterial input functions: shape and amplitude distortions and their correction. Journal of Magnetic Resonance Imaging 2005;22(6):704-709.
83. Bleeker EJ, van Buchem MA, van Osch MJP. Optimal location for phase-based arterial input function measurements near the MCA for DSC-perfusion. Pro. Int. Soc. Mag. Reson. Med. 16 Toronto; 2008.
84. Duhamel G, Schlaug G, Alsop DC. Measurement of arterial input functions for dynamic susceptibility contrast magnetic resonance imaging using echoplanar images: Comparison of physical simulations with in vivo results. Magnetic Resonance in Medicine 2006;55(3):514-523.
85. Bleeker EJ, van Buchem MA, van Osch MJ. Optimal location for arterial input function measurements near the middle cerebral artery in first-pass perfusion MRI. J Cereb Blood Flow Metab 2009.
86. Thornton RJ, Jones JY, Wang ZYJ. Correcting the effects of background microcirculation in the measurement of arterial input functions using dynamic susceptibility contrast MRI of the brain. Magnetic Resonance Imaging 2006;24(5):619-623.
87. Thijs VN, Somford DM, Bammer R, Robberecht W, Moseley ME, Albers GW. Influence of arterial input function on hypoperfusion volumes measured with perfusion-weighted imaging. Stroke 2004;35(1):94-98.
88. Alsop DC, Wedmid A, Schlaug G. Defining a local input function for perfusion quantification with bolus contrast MRI. Pro. Int. Soc. Mag. Reson. Med. 10 Hawaii; 2002 p659.
89. Calamante F, Morup M, Hansen LK. Defining a local arterial input function for perfusion MRI using independent component analysis. Magnetic Resonance in Medicine 2004;52(4):789-797.
90. Knutsson L, Larsson EM, Thilmann O, Stahlberg F, Wirestam R. Calculation of cerebral perfusion parameters using regional arterial input functions identified by factor analysis. Journal of Magnetic Resonance Imaging 2006;23(4):444-453.

91. Duhamel G, Bazelaire CM, Alsop DC. Input functions from echoplanar hemodynamic studies using dynamic susceptibility contrast: a numerical model compared to in-vivo results. Pro. Int. Soc. Mag. Reson. Med. 11 Toronto 2003. p2199.
92. Kjolby BF, Mikkelsen IK, Pedersen M, Ostergaard L, Kiselev VG. Analysis of Partial Volume Effects on Arterial Input Functions Using Gradient Echo: A Simulation Study. Magnetic Resonance in Medicine 2009;61(6):1300-1309.
93. Ostergaard L, Chesler DA, Weisskoff RM, Sorensen AG, Rosen BR. Modeling cerebral blood flow and flow heterogeneity from magnetic resonance residue data. J Cereb Blood Flow Metab 1999;19(6):690-699.
94. Mouridsen K, Friston K, Hjort N, Gyldensted L, Ostergaard L, Kiebel S. Bayesian estimation of cerebral perfusion using a physiological model of microvasculature. Neuroimage 2006;33(2):570-579.
95. Larson KB, Perman WH, Perlmutter JS, Gado MH, Ollinger JM, Zierler K. Tracer-Kinetic Analysis for Measuring Regional Cerebral Blood-Flow by Dynamic Nuclear-Magnetic-Resonance Imaging. Journal of Theoretical Biology 1994;170(1):1-14.
96. Chen JJ, Smith MR, Frayne R. Advantages of frequency-domain modeling in dynamic-susceptibility contrast magnetic resonance cerebral blood flow quantification. Magnetic Resonance in Medicine 2005;53(3):700-707.
97. Rempp KA, Brix G, Wenz F, Becker CR, Guckel F, Lorenz WJ. Quantification of Regional Cerebral Blood-Flow and Volume with Dynamic Susceptibility Contrast-Enhanced Mr-Imaging. Radiology 1994;193(3):637-641.
98. Vonken EPA, Beekman FJ, Bakker CJG, Viergever MA. Maximum likelihood estimation of cerebral blood flow in dynamic susceptibility contrast MRI. Magnetic Resonance in Medicine 1999;41(2):343-350.
99. Calamante F. Bolus dispersion issues related to the quantification of perfusion MRI data. Journal of Magnetic Resonance Imaging 2005;22(6):718-722.
100. Calamante F, Gadian DG, Connelly A. Quantification of bolus-tracking MRI: Improved characterization of the tissue residue function using Tikhonov regularization. Magn Reson Med 2003;50(6):1237-1247.
101. Chen JJ, Frayne R, Smith MR. Reassessing the clinical efficacy of two MR quantitative DSC PWICBF algorithms following cross-calibration with PET images. Physics in Medicine and Biology 2005;50(6):1251-1263.
102. Willats L, Connelly A, Calamante F. Improved deconvolution of perfusion MRI data in the presence of bolus delay and dispersion. Magnetic Resonance in Medicine 2006;56(1):146-156.
103. Willats L, Connelly A, Calamante F. Minimising the effects of bolus dispersion in bolus-tracking MRI. Nmr in Biomedicine 2008;21(10):1126-1137.
104. Wu O, Ostergaard L, Koroshetz WJ, Schwamm LH, O'Donnell J, Schaefer PW, Rosen BR, Weisskoff RM, Sorensen AG. Effects of tracer arrival time on flow estimates in MR perfusion-weighted imaging. Magnetic Resonance in Medicine 2003;50(4):856-864.
105. Dixon WT, Du LN, Faul DD, Gado M, Rossnick S. Projection angiograms of blood labeled by adiabatic fast passage. Magn Reson Med 1986;3(3):454-462.
106. Parkes LM, Tofts PS. Improved accuracy of human cerebral blood perfusion measurements using arterial spin labeling: accounting for capillary water permeability. Magn Reson Med 2002;48(1):27-41.
107. Zhou J, Wilson DA, Ulatowski JA, Traystman RJ, Van Zijl PC. Two-compartment exchange model for perfusion quantification using arterial spin tagging. J Cereb Blood Flow Metab 2001;21(4):440-455.
108. St Lawrence KS, Wang S, Wu WC. Water exchange rates in grey and white matter measured by diffusion-weighted perfusion MRI. Pro. Int. Soc. Mag. Reson. Med. 16 Toronto; 2008. p188.
109. St Lawrence KS, Frank JA, McLaughlin AC. Effect of restricted water exchange on cerebral blood flow values calculated with arterial spin tagging: a theoretical investigation. Magn Reson Med 2000;44(3):440-449.

110. Pell GS, Thomas DL, Lythgoe MF, Calamante F, Howseman AM, Gadian DG, Ordidge RJ. Implementation of quantitative FAIR perfusion imaging with a short repetition time in time-course studies. Magnetic Resonance in Medicine 1999;41(4):829-840.
111. Wong EC, Cronin M, Wu WC, Inglis B, Frank LR, Liu TT. Velocity-selective arterial spin labeling. Magn Reson Med 2006;55(6):1334-1341.
112. Alfke K, Werner R, Helle M, Rohr A, Borsch K, Stingele R, Jansen O. Magnetic resonance imaging of individual cerebral perfusion territories improves the diagnosis of embolic stroke. J Comput Assist Tomogr 2007;31(6):894-895.
113. Hendrikse J, van der Zwan A, Ramos LM, van Osch MJ, Golay X, Tulleken CA, Van Der GJ. Altered flow territories after extracranial-intracranial bypass surgery. Neurosurgery 2005;57(3):486-494.
114. van Laar PJ, Hendrikse J, Mali WPTM, Moll FL, van der Norp HB, van Osch MJP, van der Grond J. Altered flow territories after carotid stenting and carotid endarterectomy. Journal of Vascular Surgery 2007;45(6):1155-1161.
115. van Osch MJ, Teeuwisse WM, van Walderveen MA, Hendrikse J, Kies D.A., van Buchem MA. Can arterial spin labeling detect white matter perfusion signal? Magn Reson Med 2009.
116. Alsop DC, Detre JA. Multisection cerebral blood flow MR imaging with continuous arterial spin labeling. Radiology 1998;208:410-416.
117. Werner R, Norris DG, Alfke K, Mehdorn HM, Jansen O. Improving the amplitude-modulated control experiment for multislice continuous arterial spin labeling. Magn Reson Med 2005;53(5):1096-1102.
*118. Buxton RB, Frank LR, Wong EC, Siewert B, Warach S, Edelman RR. A general kinetic model for quantitative perfusion imaging with arterial spin labeling. Magn Reson Med 1998;40(3):383-396.
Description of the tracer kinetic model of Arterial Spin Labeling. Both theory of PASL and CASL are provided and an introduction of multi TI ASL is given.
*119. Alsop DC, Detre JA. Reduced transit-time sensitivity in noninvasive magnetic resonance imaging of human cerebral blood flow. J Cereb Blood Flow Metab 1996;16(6):1236-1249.
This paper provides the basic theory for obtaining quantitative cerebral blood flow values for CASL. It demonstrates that the inclusion of a delay into the sequence, results in reduced sensitivity towards transport times.
*120. Dai W, Garcia D, de Bazelaire C, Alsop DC. Continuous flow-driven inversion for arterial spin labeling using pulsed radio frequency and gradient fields. Magn Reson Med 2008;60(6):1488-1497.
In this article, the technique of pseudo- or pulsed CASL is introduced. Due to its favorable RF-characteristics and the high SNR, this technique has gained much attention lately and will probable lead to many applications in the near future.
121. Gracia DM, Bazelaire CM, Alsop DC. Pseudo-continuous Flow Driven Adiabatic Inversion for Arterial Spin Labeling. Pro. Int. Soc. Mag. Reson. Med. 13; 2005. 37.
122. Wu WC, Fernandez-Seara M, Detre JA, Wehrli FW, Wang J. A theoretical and experimental investigation of the tagging efficiency of pseudocontinuous arterial spin labeling. Magn Reson Med 2007;58(5):1020-1027.
123. Kim SG. Quantification of relative cerebral blood flow change by flow- sensitive alternating inversion recovery (FAIR) technique: application to functional mapping. Magn Reson Med 1995;34(3):293-301.
124. Wong EC, Buxton RB, Frank LR. Quantitative perfusion imaging using arterial spin labeling. Neuroimaging Clin N Am 1999;9(2):333-342.
125. Wong EC, Buxton RB, Frank LR. Quantitative imaging of perfusion using a single subtraction (QUIPSS and QUIPSS II). Magn Reson Med 1998;39(5):702-708.
126. Edelman RR, Siewert B, Darby DG, Thangaraj V, Nobre AC, Mesulam MM, Warach S. Qualitative mapping of cerebral blood flow and functional localization with echo-planar MR imaging and signal targeting with alternating radio frequency. Radiology 1994;192(2):513-520.
127. Jahng GH, Zhu XP, Matson GB, Weiner MW, Schuff N. Improved perfusion-weighted MRI by a novel double inversion with proximal labeling of both tagged and control acquisitions. Magn Reson Med 2003;49(2):307-314.

128. Golay X, Stuber M, Pruessmann KP, Meier D, Boesiger P. Transfer insensitive labeling technique (TILT): application to multislice functional perfusion imaging. J Magn Reson Imaging 1999;9(3):454-461.
129. Golay X, Petersen ET, Hui F. Pulsed star labeling of arterial regions (PULSAR): a robust regional perfusion technique for high field imaging. Magn Reson Med 2005;53(1):15-21.
130. Hendrikse J, Lu H, van der Grond J, Van Zijl PC, Golay X. Measurements of cerebral perfusion and arterial hemodynamics during visual stimulation using TURBO-TILT. Magn Reson Med 2003;50(2):429-433.
131. Gunther M, Bock M, Schad LR. Arterial spin labeling in combination with a look-locker sampling strategy: inflow turbo-sampling EPI-FAIR (ITS-FAIR). Magn Reson Med 2001;46(5):974-984.
132. Helpern JA, Branch CA, Yongbi MN, Huang NC. Perfusion imaging by un-inverted flow-sensitive alternating inversion recovery (UNFAIR). Magn Reson Imaging 1997;15(2):135-139.
133. Mai VM, Hagspiel KD, Christopher JM, Do HM, Altes T, Knight-Scott J, Stith AL, Maier T, Berr SS. Perfusion imaging of the human lung using flow-sensitive alternating inversion recovery with an extra radiofrequency pulse (FAIRER). Magn Reson Imaging 1999;17(3):355-361.
134. Barbier EL, Lamalle L, Decorps M. Methodology of brain perfusion imaging. J Magn Reson Imaging 2001;13(4):496-520.
135. Jahng GH, Weiner MW, Schuff N. Improved arterial spin labeling method: applications for measurements of cerebral blood flow in human brain at high magnetic field MRI. Med Phys 2007;34(11):4519-4525.
136. Calamante F, Thomas DL, Pell GS, Wiersma J, Turner R. Measuring cerebral blood flow using magnetic resonance imaging techniques. J Cereb Blood Flow Metab 1999;19(7):701-735.
137. Schraml C, Boss A, Martirosian P, Schwenzer NF, Claussen CD, Schick F. FAIR true-FISP perfusion imaging of the thyroid gland. J Magn Reson Imaging 2007;26(1):66-71.
138. Martirosian P, Klose U, Mader I, Schick F. FAIR true-FISP perfusion imaging of the kidneys. Magn Reson Med 2004;51(2):353-361.
139. Grossman EJ, Zhang K, An J, Voorhees A, Inglese M, Ge Y, Oesingmann N, Xu J, McGorty KA, Chen Q. Measurement of deep gray matter perfusion using a segmented true-fast imaging with steady-state precession (True-FISP) arterial spin-labeling (ASL) method at 3T. J Magn Reson Imaging 2009;29(6):1425-1431.
140. Gunther M, Oshio K, Feinberg DA. Single-shot 3D imaging techniques improve arterial spin labeling perfusion measurements. Magn Reson Med 2005;54(2):491-498.
141. Ye FQ, Frank JA, Weinberger DR, McLaughlin AC. Noise reduction in 3D perfusion imaging by attenuating the static signal in arterial spin tagging (ASSIST). Magn Reson Med 2000;44(1):92-100.
142. Chalela JA, Alsop DC, Gonzalez-Atavales JB, Maldjian JA, Kasner SE, Detre JA. Magnetic resonance perfusion imaging in acute ischemic stroke using continuous arterial spin labeling. Stroke 2000;31(3):680-687.
143. Herscovitch P, Raichle ME. What is the correct value for the brain--blood partition coefficient for water? J Cereb Blood Flow Metab 1985;5(1):65-69.
144. Petersen ET, Zimine I, Ho YC, Golay X. Non-invasive measurement of perfusion: a critical review of arterial spin labelling techniques. Br J Radiol 2006;79(944):688-701.
145. Wong EC, Buxton RB, Frank LR. A theoretical and experimental comparison of continuous and pulsed arterial spin labeling techniques for quantitative perfusion imaging. Magn Reson Med 1998;40(3):348-355.
146. Aslan S, Xu F, Wang Pl, Uh J, Yezuvath U, van Osch MJ, Lu H. Labeling efficiency is critical in pseudo-continuous ASL. Pro. Int. Soc. Mag. Reson. Med. 17 Hawaii; 2009. 620.
147. Schepers J, van Osch MJ, Bartels LW, Heukels SN, Viergever MA, Nicolay K. The effect of B1 field inhomogeneity and the nonselective inversion profile on the kinetics of FAIR-based perfusion MRI. Magn Reson Med 2005;53(6):1355-1362.
148. Pell GS, Lewis DP, Ordidge RJ, Branch CA. TurboFLASH FAIR imaging with optimized inversion and imaging profiles. Magn Reson Med 2004;51(1):46-54.

149. Luh WM, Wong EC, Bandettini PA, Hyde JS. QUIPSS II with thin-slice TI1 periodic saturation: a method for improving accuracy of quantitative perfusion imaging using pulsed arterial spin labeling. Magn Reson Med 1999;41(6):1246-1254.
150. Hendrikse J, van Osch MJ, Rutgers DR, Bakker CJ, Kappelle LJ, Golay X, van der Grond J. Internal carotid artery occlusion assessed at pulsed arterial spin-labeling perfusion MR imaging at multiple delay times. Radiology 2004;233(3):899-904.
151. Petersen ET, Lim T, Golay X. Model-free arterial spin labeling quantification approach for perfusion MRI. Magn Reson Med 2006;55(2):219-232.
152. Petersen ET, Mouridsen K, Golay X. The QUASAR reproducibility study, Part II: Results from a multi-center Arterial Spin Labeling test-retest study. Neuroimage 2010;49(1):104-113.
153. St Lawrence KS, Wang J. Effects of the apparent transverse relaxation time on cerebral blood flow measurements obtained by arterial spin labeling. Magn Reson Med 2005;53(2):425-433.
154. Teeuwisse WM, van der Grond J, van Buchem MA, van Osch MJ. Transversal relaxation effects on arterial spin labeling investigated by dual echo pseudo continuous ASL. Pro. Int. Soc. Mag. Reson. Med. 15 Berlin; 2007. p3492.
155. Yang Y, Gu H, Stein EA. Simultaneous MRI acquisition of blood volume, blood flow, and blood oxygenation information during brain activation. Magn Reson Med 2004;52(6):1407-1417.
156. Woolrich MW, Chiarelli P, Gallichan D, Perthen J, Liu TT. Bayesian inference of hemodynamic changes in functional arterial spin labeling data. Magn Reson Med 2006;56(4):891-906.
157. Zhang W, Silva AC, Williams DS, Koretsky AP. NMR measurement of perfusion using arterial spin labeling without saturation of macromolecular spins. Magn Reson Med 1995;33(3):370-376.
158. Zaharchuk G, Ledden PJ, Kwong KK, Reese TG, Rosen BR, Wald LL. Multislice perfusion and perfusion territory imaging in humans with separate label and image coils. Magn Reson Med 1999;41(6):1093-1098.
159. Trampel R, Mildner T, Goerke U, Schaefer A, Driesel W, Norris DG. Continuous arterial spin labeling using a local magnetic field gradient coil. Magn Reson Med 2002;48(3):543-546.
160. Hendrikse J, van der Grond J., Lu H, Van Zijl PC, Golay X. Flow Territory Mapping of the Cerebral Arteries With Regional Perfusion MRI. Stroke 2004.
161. Werner R, Norris DG, Alfke K, Mehdorn HM, Jansen O. Continuous artery-selective spin labeling (CASSL). Magn Reson Med 2005;53(5):1006-1012.
162. Helle M, van Osch MJ, Norris DG, Alfke K, Jansen O. Superselective Pseudo-Continuous Arterial Spin Labeling. Pro. Int. Soc. Mag. Reson. Med. 16 Toronto; 2008. 183.
163. Kansagra AP, Wong EC. Mapping of vertebral artery perfusion territories using arterial spin labeling MRI. J Magn Reson Imaging 2008;28(3):762-766.
164. Kansagra AP, Wong EC. Quantitative assessment of mixed cerebral vascular territory supply with vessel encoded arterial spin labeling MRI. Stroke 2008;39(11):2980-2985.
165. Wu B, Wang X, Guo J, Xie S, Wong EC, Zhang J, Jiang X, Fang J. Collateral circulation imaging: MR perfusion territory arterial spin-labeling at 3T. AJNR Am J Neuroradiol 2008;29(10):1855-1860.
166. Wong EC. Vessel-encoded arterial spin-labeling using pseudocontinuous tagging. Magn Reson Med 2007;58(6):1086-1091.

Chapter 3: Optimal location for arterial input function measurements near the middle cerebral artery in first pass perfusion MRI

Egbert JW Bleeker, Mark A van Buchem, Matthias JP van Osch

ABSTRACT

One of the main difficulties in obtaining quantitative perfusion values from dynamic susceptibility contrast-magnetic resonance imaging is a correct arterial input function (AIF) measurement, as partial volume effects can lead to an erroneous shape and amplitude of the AIF. Cerebral blood flow and volume scale linearly with the area under the AIF, but shape changes of the AIF can lead to large nonlinear errors. Current manual and automated AIF selection procedures do not guarantee the exclusion of partial volume effects from AIF measurements. This study uses a numerical model, validated by phantom experiments, for predicting the optimal location for AIF measurements in the vicinity of the middle cerebral artery (MCA). Three different sequences were investigated and evaluated on a voxel-by-voxel basis by comparison with the ground truth. Subsequently, the predictions were evaluated in an in vivo example. The findings are fourfold: AIF measurements should be performed in voxels completely outside the artery, here a linear relation should be assumed between ΔR_2^* and the concentration contrast agent, the exact optimal location differs per acquisition type, and voxels including a small MCA yield also correct AIF measurements for segmented EPI when a short echo time was used.

Published in Journal of Cerebral Blood Flow and Metabolism (2009) Apr; 29(4):840-52

INTRODUCTION

Perfusion-weighted imaging can provide important physiological parameters related to the cerebral microvasculature, parameters such as cerebral blood flow (CBF), cerebral blood volume (CBV), mean transit time (MTT), and time of arrival (TA) (1, 2). These parameters enable the identification and characterization of pathological areas in brain tissue. Perfusion-weighted imaging can identify tissue at risk of infarction in stroke patients, facilitate grading and delineation of brain tumors, and can provide important hemodynamic information in, for example, Alzheimer's disease, obstructive cerebrovascular disease and migraine (3-6).

Dynamic susceptibility contrast-magnetic resonance imaging (DSC-MRI) measures brain perfusion by monitoring dynamically the first passage of a bolus of contrast agent through the microvasculature of the brain tissue. Because the concentration of the contrast agent passing through the tissue microvasculature increases, the transverse relaxation time decreases leading to decreased signal magnitude. An arterial input function (AIF), which describes the concentration of the contrast agent passing through an artery feeding the brain, is required for deconvolution to calculate the perfusion parameters CBV (area-under-the-curve of the impulse response) and CBF (the peak-height of the impulse response). The MTT is the ratio of CBV over CBF. An erroneous measurement of the area under the AIF, would not affect the quantitative value of the MTT, because both CBV and CBF scale equally with the area under the AIF. Therefore, it is sufficient to measure the correct shape of the AIF for MTT quantification. However, for correct quantification of CBF and CBV it is necessary to measure the AIF with both a correct shape and a correct peak-height (1, 7).

Although both the magnitude and phase of the DSC-MRI signal can be used for AIF measurements (8, 9), the magnitude of the MR signal is used most often. Voxels for the AIF are normally selected either manually (6) or automatically (10, 11). Most automatic and manual AIF selection methods are based on criteria, such as an early rise, small width, high peak-height and large area-under-the-curve. It is known that partial volume effects can affect both the shape and peak-height of the measured AIF, thereby leading to large quantification errors of CBF and CBV (12). Because these effects can also lead to more narrow curves or a higher maximum value, most selection procedures do not prohibit the inclusion of voxels that exhibit partial volume effects. For parallel-orientated arteries, such as the internal carotid artery, partial volume errors (PVEs) can be corrected (13), but in normal clinical practice the AIF is measured in the vicinity of the middle cerebral artery (MCA) because of its size and location close to brain tissue. Because the MCA is oriented approximately perpendicular to the main magnetic field, correction for PVEs is not possible, and distortions of the AIF can occur. A good theoretical basis for the proper criteria to select the optimum location to measure the AIF (e.g. exhibiting the correct shape and height) in the vicinity of the MCA is currently lacking.

The goal of this study is to provide a theoretical basis for AIF selection close to the MCA, using a numerical model validated using phantom experiments. The optimal location for

selecting the AIF in the vicinity of the MCA was identified for several different types of gradient echo sequences that are commonly used in DSC-MRI. Furthermore, the findings were tested in a clinical example of a patient who was scanned twice with different DSC-MRI sequences.

MATERIALS AND METHODS

The aim of this study is to find the optimal location for AIF selection in the vicinity of the MCA. For this purpose, a numerical model was developed that included both image formation and the dependence of the relaxation time and magnetic field distribution on the presence of contrast agent. Three commonly used DSC-MRI sequences, single shot echo planar imaging (EPI), dual echo-segmented EPI and PRESTO (Principles of echo-shifting with a train of observations) (14), were implemented in the numerical model and the model was validated by phantom experiments.

After validation using parameters representative for the experimental setup, the model was adjusted to resemble in vivo AIF measurements more closely: the passage of contrast agent through brain tissue surrounding the artery was included and relaxation rates and values were changed to in vivo values. This extended model will be referred to as the advanced model. The diameter of the vessel was varied in the advanced model to study the influence of the size of the MCA on the AIF measurements.

Numerical model

The MCA in the numerical model was modeled as an infinite cylinder perpendicular to the main magnetic field and parallel to the left and right axis. The reported diameter of the MCA varies from 2 to 4 mm (15, 16) and the average flow in the MCA is 2.6 ml/sec (17). For reasons of symmetry, only the plane whose normal is parallel to the vessel axis needs to be considered in the simulations. All results are therefore presented in a sagittal view, although the model represents acquisition of transverse slices.

Contrast agent properties

Gadolinium-based contrast agents (e.g. Gd-DTPA) affect magnetic susceptibility ($\triangle\chi = d\chi\,[Gd]$,, with $d\chi = 0.3209 \cdot 10^{-3}$ [l mol^{-1}] (13)), as well as longitudinal and transverse relaxation times. The dependence of the transverse relaxation rate on the concentration of Gd-DTPA is different for aqueous solutions, as used in the phantom experiments; and for whole blood, where the presence of red blood cells causes a quadratic relation between transverse relaxation rate and contrast agent concentration (18). Therefore, a linear relation between the transverse relaxation rate and concentration Gd-DTPA was used for comparisons with phantom experiments (5.3 and 5.2 l/mmol/sec at 1.5 T and 3 T respectively (19)). For the advanced model a quadratic relation between transversal relaxation rate (or relaxivity) of intravascular blood and concentration

Gd-DTPA was used (linear term 7.62 l/mmol/sec quadratic term 0.57 l^2/$mmol^2$/sec at 1.5 T (13)). When modeling the passage of contrast agent through the microvasculature of tissue a linear relation was used (44 and 87 l/mmol/sec at 1.5 T and 3 T (20)). The effect of the contrast agent on the longitudinal relaxation was only taken into account for the tissue passage assuming a single longitudinal relaxation rate for the tissue and microvascular components combined and assuming an intact blood-brain barrier (4.3 and 3.3 l/mmol/sec at 1.5 T and 3 T (19, 21)). T_1 effects inside the MCA were assumed negligible, because these will be minimal for relatively long repetition times because of inflow of fresh spins (22).

Magnetic field changes

An intravascular susceptibility change in a vessel perpendicular to the main magnetic field results in local field changes in and around the vessel. These local field changes were calculated using Maxwell equations taking into account the sphere of Lorenz (23):

$$B_{\text{int}} = \frac{\Delta\chi}{6}\left(3(\cos\theta)^2 - 1\right)B_0 \qquad [1]$$

$$B_{ext} = \left(\frac{\Delta\chi}{2}\left(\frac{a}{\rho}\right)^2 (\sin\theta)^2 \cos 2\varphi\right)B_0 \qquad [2]$$

with B_{int} the magnetic field change inside the vessel, B_{ext} the magnetic field change outside the vessel, B_0 the main magnetic field strength, $\Delta\chi$ the susceptibility difference between the intra- and extravascular compartment, a the radius of the vessel, ρ, θ, and φ spherical coordinates where ρ equals the distance from the grid point to the vessel center and θ the angle between the vessel and the main magnetic field B_0 (assumed to be 90° for the MCA). In the absence of contrast agent, it was assumed that there is no susceptibility difference between the interior and exterior of the MCA.

Image formation

Local magnetic field changes lead to distortions in MR images, especially when using fast imaging techniques such as EPI. Such image distortions were included in the model by simulating the image formation process. Frequency encoding was assumed parallel to the MCA. Imaging for EPI and segmented EPI was modeled using the expression:

$$S(k_m, z_i, [Gd]) = \sum_{j=1}^{N} M_0 \cdot \frac{\sin\alpha \cdot \left(1 - \exp\left(-\frac{TR}{T_1(x_j, z_i, [Gd])}\right)\right)}{\left(1 - \cos\alpha \cdot \exp\left(-\frac{TR}{T_1(x_j, z_i, [Gd])}\right)\right)} \cdot \exp\left(-\frac{T_m}{T_2^*(x_j, z_i, [Gd])}\right) \cdots$$

$$\exp(i \cdot 2 \cdot \pi \cdot k_m \cdot x_j) \cdot \exp(i \cdot \gamma \cdot \Delta B(x_j, z_i, [Gd]) \cdot T_m) \quad [3]$$

with M_0 the initial longitudinal magnetization, α the flip angle, TR the repetition time, T_1 the longitudinal relaxation (1.5 T: 0.95, 1.2 sec and 1.4 sec for tissue, $MnCl_2$ doped water and blood respectively (24)) and 3.0 T: 1.1 sec and 1.7 sec for tissue and blood (25, 26), T_m the time from excitation to read-out of each k-line (the time between each k-line (ΔT_m) is 0.74 and 0.97 msec, for EPI and segmented EPI, respectively), T_2^* is 0.1 sec at 1.5 T for tissue (24), $MnCl_2$ doped water and blood and approximately 0.07 sec at 3 T for tissue, k_m the m^{th} k-line, x the position within the slice and γ the gyromagnetic ratio. Equation 3 is similar to that of Duhamel et al. (27). Imaging parameters were taken from local perfusion protocols and were equal to the imaging parameters of the phantom experiments. Because PRESTO is commonly used as 3D sequence, Equation 3 is extended to two-phase encoding directions,

$$S(k_{m_1}, k_{m_2}, [Gd]) = \sum_{i=1}^{M} \sum_{j=1}^{N} M_0 \cdot \frac{\sin\alpha \cdot \left(1 - \exp\left(-\frac{TR}{T_1(x_j, z_i, [Gd])}\right)\right)}{\left(1 - \cos\alpha \cdot \exp\left(-\frac{TR}{T_1(x_j, z_i, [Gd])}\right)\right)} \cdot \exp\left(-\frac{T_m}{T_2^*(x_j, z_i, [Gd])}\right) \cdots$$

$$\exp(i \cdot 2 \cdot \pi \cdot k_{m_1} \cdot x_j) \cdot \exp(i \cdot 2 \cdot \pi \cdot k_{m_2} \cdot z_i) \cdot \exp(i \cdot \gamma \cdot \Delta B(x_j, z_i, [Gd]) \cdot T_m \quad [4]$$

with ΔT_m 0.73 msec. PRESTO uses large gradients for echo-shifting that crush the intravascular signal, and therefore the intravascular signal was set to zero.

The images from EPI and segmented EPI were reconstructed using 1D inverse discrete Fourier transformation; and those from PRESTO using 2D inverse discrete Fourier transformation. Before inverse Fourier transformation, windowing, using a Tukey window, and zerofilling was performed.

Implementation

The model was implemented in MATLAB (R2006b, Natick, MA, USA) and evaluated on a spatial grid of 250 μm except for PRESTO for which a grid of 500 μm was used because of computational limitations. To study the influence of the location of the vessel with respect to the simulated

voxels, the positions of the voxels was shifted in steps of 500 µm with respect to the vessel center in both directions perpendicular to the vessel. The simulated voxels have the same dimensions as the voxels of commonly used MR sequences, but the results of these simulations are depicted for each shift (e.g. at a 500 µm resolution). The shifts in the slice direction for EPI and segmented EPI were performed before calculating the local field changes. The shifts in the phase encoding direction were performed by adding a small phase to the signal before the inverse discrete Fourier transformation. For comparison with the phantom experiments, a linearly increasing concentration of Gd-DTPA, in steps of 0.9 mmol/l, was simulated.

The advanced model included not only an AIF-shaped passage of contrast agent through the MCA (28), but also the passage of contrast agent through the microvasculature of tissue surrounding the vessel. The tissue passage curve was created after convolving the concentration contrast agent profile of the AIF with an exponential residue function (CBF = 60 ml/100g/min, MTT = 4 sec, CBV = 4 ml/100g).

Magnetic resonance imaging experiments

Phantom experiments

The flow-phantom consisted of a tube (4 mm internal diameter and 0.25 mm thickness) oriented perpendicular to the main magnetic field. $MnCl_2$-doped water was circulated through the tube at a constant velocity of 2.8 ml/sec. The tube was surrounded by the same $MnCl_2$ solution to create a background signal representing the tissue signal. The concentration of Gd-DTPA (Magnevist, Schering, Germany) within the tube was increased in seventeen successive steps of 0.9 mmol/l.

All phantom experiments were performed at 1.5 T (Philips Achieva, Best, The Netherlands) using a standard quadrature head coil. The imaging sequences had the following settings: single shot EPI, data matrix (MA) 96x95 zerofilled to 128x128, TE/TR 41/1500 msec, FA = 80º, field of view (FOV) = 230x230 mm^2, 15 slices of thickness 6 mm with no interslice gap: dual echo-segmented EPI, MA 128x75 zerofilled to 128x128, TE_1/TE_2/TR 11/30/400 msec, FA = 53º, FOV 220x220 mm^2, 8 slices of 6 mm thickness with 1 mm gap, 5 segments: PRESTO, MA 64x63 zerofilled to 128x128, TE/TR 25/17 msec, FA = 7º, FOV 220x220 mm^2, 30 slices of thickness 3.5 mm, 90 segments.

The stack of slices was shifted in steps of 1 mm for the EPI and segmented EPI experiments and 0.5 mm for the PRESTO experiment in the slice direction in order to measure various locations of the vessel center inside an imaging slice.

In vivo example

Two DSC-MRI scans were performed in a patient (woman, 32 years) diagnosed with Systemic Lupus Erythematosus (13 months between the 2 MR examinations). In vivo experiments were performed at 3 T (Philips Achieva, Best, the Netherlands) using an 8-channel sense head coil,

0.1 mmol/kg-bodyweight Gd-DTPA was injected at 5 ml/sec followed by a saline chaser of 25 ml injected at the same speed. Perfusion scans were made as part of another research study. The imaging sequences had the following settings: first DSC-MRI scan, dual echo-segmented EPI: MA 96x94 zerofilled to 96x96, TE_1/TE_2/TR 11/31/600 msec, FA = 40°, FOV 220x220 mm^2, SENSE factor of 2.2, 10 slices of 6 mm thickness with 1 mm gap, EPI factor 21, 2 segments; second DSC-MRI scan, PRESTO: MA 64x53 zerofilled to 128x108, TE/TR 26/17 msec, FA = 5°, FOV 224x168 mm^2, SENSE factor of 2.4, 48 slices of 3.0 mm, EPI factor 21, 60 segments. The patient has given informed consent prior to the MRI examinations.

Image analysis

Numerical model validation

For each concentration of Gd-DTPA the set of transverse images that were shifted with respect to the vessel center were merged into a single image viewed in a sagittal orientation. Each pixel in this higher resolution image therefore represents a voxel with a larger volume (e.g. a typical volume encountered in clinical DSC-MRI scans) than depicted in the image. The ΔR_2^* was calculated using:

$$\Delta R_2^* = -(1/TE)\cdot \ln(S/S_0) \qquad [5]$$

with S the signal magnitude, S_0 the signal magnitude without contrast agent and TE the echo time.

The model was validated using the phantom measurements by visually comparing the distorted pattern of signal decrease in the magnitude images for all concentrations; and using the Pearson's correlation coefficient, a measure of correct shape, and relative signal strength (RSS), a measure of amplitude, for quantitative comparison. The RSS was defined as the regressing coefficient (in percent) between the measured ΔR_2^* and the expected ΔR_2^* (the concentration of the contrast agent multiplied by the relaxivity (5.3 l/mmol/sec)). The correlation was calculated using a Pearson's correlation method between the measured ΔR_2^* and the expected ΔR_2^*.

Advanced model

The advanced numerical model is used for predicting the optimal location for AIF selection near the MCA and is adjusted to closely resemble in vivo AIF measurements. The advanced model included the quadratic relation for relaxivity in the vessel and the contrast agent passage through tissue surrounding the MCA. The model was evaluated by the Pearson's correlation and the RSS; both quality measures were calculated from the beginning of the first pass of the AIF to the end of the recirculation.

Because the final outcome of AIF measurements will also depend on the applied postprocessing, three different postprocessing methods were studied: the first postprocessing method

uses a previously published calibration curve of contrast agent in whole human blood that shows a quadratic relation of ΔR_2^* as a function of the concentration contrast agent (13). This approach should therefore be valid for measurements inside the vessel. The second approach employs a linear relation between ΔR_2^* and concentration contrast agent, which is assumed to be valid for measurements outside the vessel. The final approach employs also a linear assumption, combined with subtraction of the tissue curve from the measured AIF (29). This method should correct the input function measurement for contamination with the passage of contrast agent through tissue surrounding the artery. The model was analyzed both in the absence of noise as well as by including noise (SNR of 25 defined in terms of Gaussian noise on real and imaginary part of the precontrast signal intensity). A single simulation (PRESTO, Ø 4 mm) was performed using 3.0 T literature values and analyzed for both out-vessel both with and without tissue curve subtraction. To visualize the optimal locations for AIF measurements near the MCA, the correlation was depicted for all voxels with a RSS larger than 25% and a correlation value higher than 0.97.

In vivo evaluation

The location of the M1 segment of MCA in the patient was determined in the T_1-weighted image. The coordinates were transformed to the PRESTO and dual echo-segmented EPI coordinates. The normalized ΔR_2^* profiles of the voxels in and around the MCA are presented without further postprocessing. Based on the findings of the simulation study, the most optimal locations were highlighted.

RESULTS

Numerical model validation by phantom experiments

The numerical model was validated using phantom experiments by comparing a sagittal view of the transverse acquired magnitude images at different concentrations of contrast agent (0 to 15 mmol/l Gd-DTPA) and using the Pearson's correlation and RSS for quantitative validation (Figures 1 and 2). The images of the model show good agreement with the images from the phantom experiments.

The acquisition voxel sizes of the simulation and phantom experiments are the same and similar to the voxel size of normal in vivo DSC-MRI protocol, although the pixel sizes in the images are different due to different shifting steps (0.5 mm in both directions in the simulations, and 1.0 mm (0.5 mm for PRESTO) in the slice direction in the phantom experiments). It was concluded that the simulations provide a correct representation of the MR signal processes around a vessel during the passage of contrast agent.

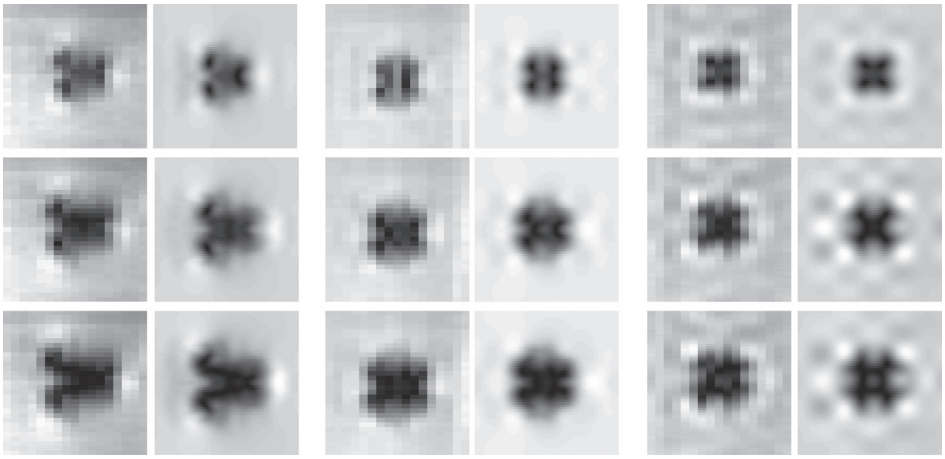

Figure 1: Merged magnitude images (sagittal-view) of the phantom experiments and the simulations for single shot EPI (left), segmented EPI (TE_2; middle) and PRESTO (right) at three concentrations of Gd-DTPA (4.4 mM, 8.8 mM and 13.2 mM). The phantom images are formed by merging several multi-slice acquisitions (acquired in a transverse plane) that are shifted in the slice selection direction. Therefore, each pixel in this image represents a larger acquisition voxel. The phase encoding is oriented anterior to posterior. In the phantom, the stack of slices was shifted in steps of 1 mm for both EPI acquisitions and in steps of 0.5 mm for the PRESTO experiment. In the simulation, the stack of slices was shifted for all three acquisitions in steps of 0.5 mm in the slice and phase encoding directions.

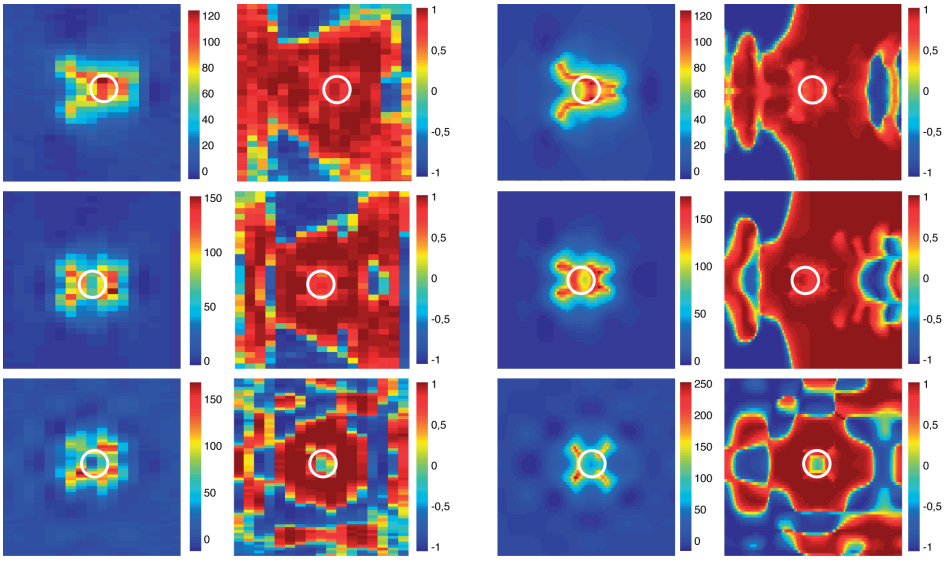

Figure 2: The relative signal strength (RSS in percent, first and third column) and correlation (second and fourth column) for the phantom experiments (first two columns) and the simulations (last two columns), with the vessel depicted as a white circle. From top to bottom: single shot EPI, segmented EPI (TE_2) and PRESTO.

Advanced model evaluation

Figure 3 shows the normalized ΔR_2^* profiles of voxels acquired using segmented EPI (TE_2) in and around the MCA grouped according to the correlation with respect to the ground truth. In the group with a correlation value between 0.7 and 0.8, peaks are observed on top of the passage curve that can be attributed to PVE. In this study we define a correct measurement of the shape of the AIF as a correlation between the measured AIF and the ground truth that is higher than 0.99 (correlation values based on noise free simulations).

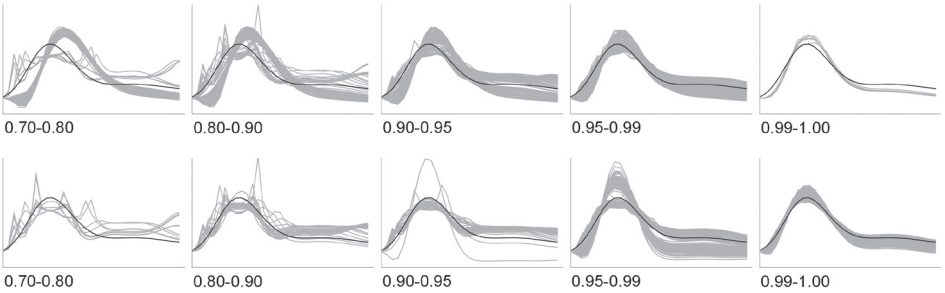

Figure 3: The measured AIF profiles of all simulated voxels for segmented EPI (TE_2) were normalized and grouped according to the correlation value with respect to the ground truth (between 0.7 and 0.8 (1st graph), between 0.8 and 0.9 (2nd graph), between 0.9 and 0.95 (3rd graph), between 0.95 and 0.99 (4th graph) and between 0.99 and 1 (5th graph)). Upper row shows curves without tissue subtraction; lower row shows curves with tissue subtraction.

Figure 4 shows the results for PRESTO using in-vessel strategy and both out-vessel strategies. Independent of the used postprocessing strategy, the most optimal locations for AIF measurements were always observed outside the MCA. Optimal locations were found diagonally from the vessel center at a distance of approximately 4 mm. Simulations were repeated, now with addition of Gaussian noise on top of the complex signals. This resulted in a lower correlation with the ground truth, whereas the signal strength remained unchanged.

Three diameters of the MCA were investigated with the out-vessel strategy and tissue curve subtraction employed for postprocessing (see figure 5). This resulted for single-shot EPI some feasible locations for AIF determination, but not every position of the MCA within the imaging slice provided voxels that passed our criterion for correct shape measurement (correlation higher than 0.99 with the ground truth). For large and medium-sized vessels, the optimal location is found in an area 3.5 to 6 mm posterior to the vessel center. Segmented EPI yields larger regions suitable for AIF selection. AIF selection using segmented EPI is less sensitive to the exact location of the vessel center within the imaging slice (see figure 5, 2nd and 3rd columns). Optimal locations are found all around the vessel (note that voxels located above the vessel are actually located in a slice superior to the slice through which the MCA runs). For the first echo time optimal locations are located relatively close to the vessel, but still outside the vessel, except for a small-sized MCA (Ø 2 mm), in this special case optimal locations are within a circle approximately 4 mm from the

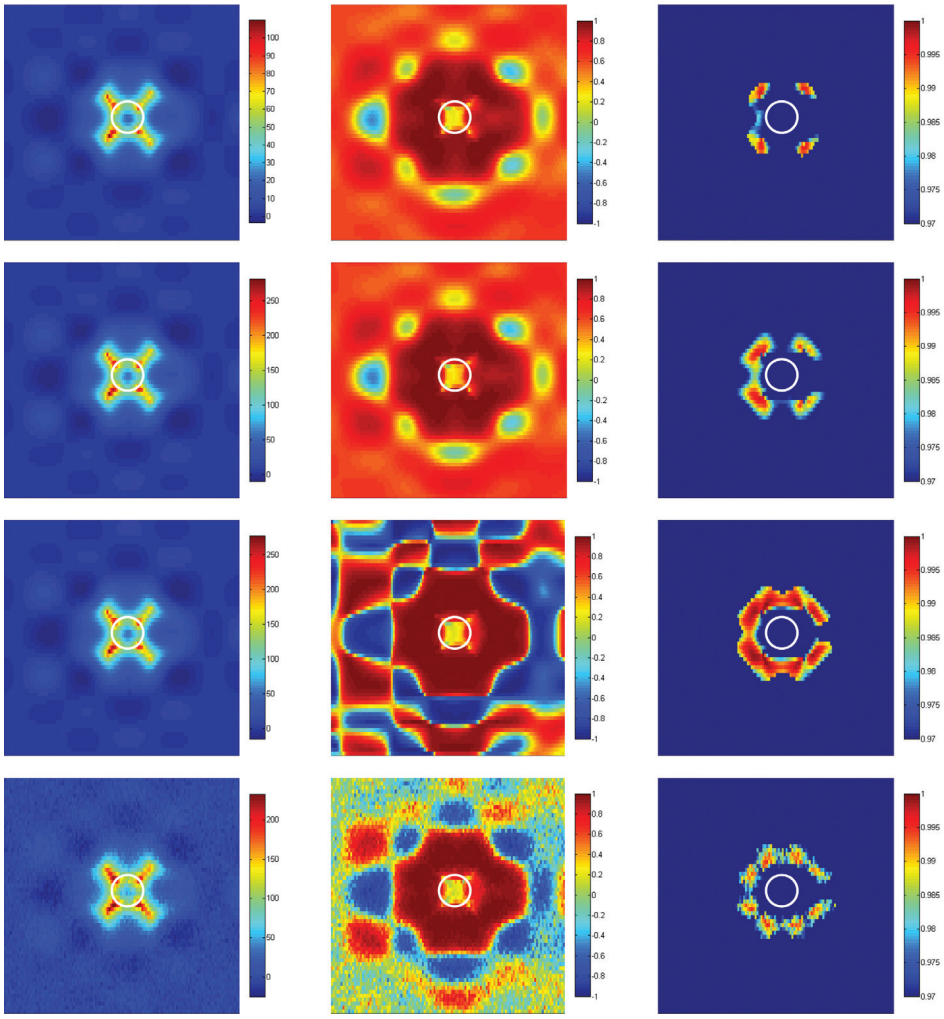

Figure 4: The relative signal strength (RSS in percent; left column), the correlation (middle column) and the RSS-thresholded correlation image (correlation coefficient larger than 0.97 and RSS larger than 25%; right column) for PRESTO at 1.5 Tesla using the in-vessel strategy (first row), out-vessel strategy (second row), out-vessel strategy with tissue subtraction (third row) and with noise included in the simulations (SNR=25 using out-vessel strategy with tissue curve subtraction; last row).

vessel center including voxels that are primarily sensitive to the intravascular signal.

For the longer echo time, optimal locations are found at a larger distance from the vessel center. Also for PRESTO, the optimal locations for AIF selection are found outside the vessel in the surrounding tissue, but here the optimal locations are found on the diagonal axis from the vessel center (see figure 5, 4th column). Figure 6 shows the results of the simulations performed using 3.0 T literature values for PRESTO image formation. The results are comparable to the findings of the 1.5 T simulations (compare to Figure 4).

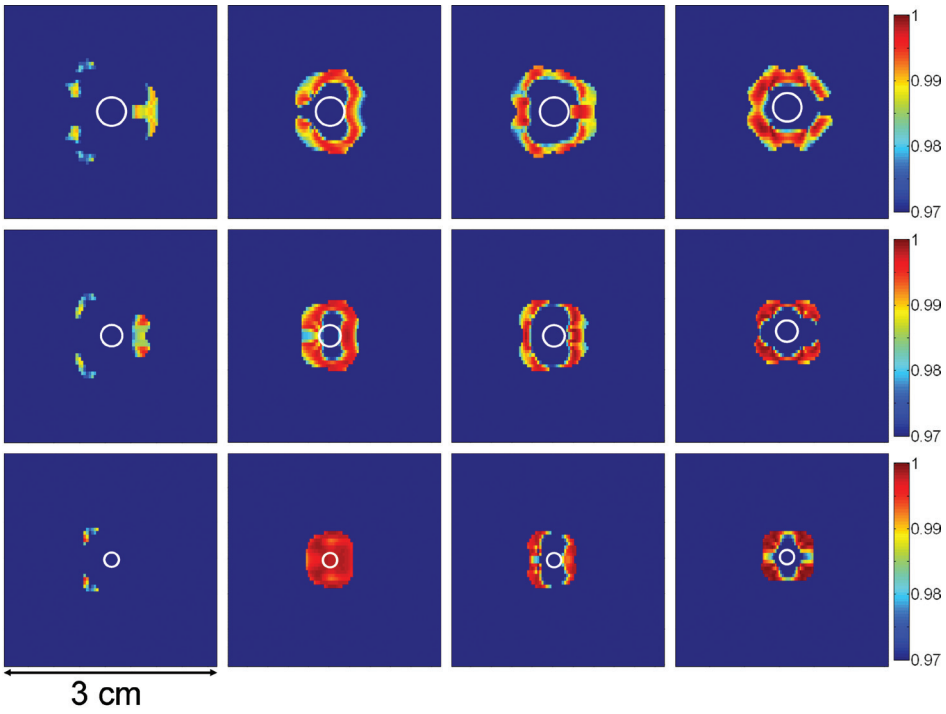

Figure 5: The RSS-thresholded correlation image (correlation coefficient larger than 0.97 and a voxel with greater than 25% RSS) for single shot EPI (1st column), segmented EPI (TE_1 and TE_2, 2nd and 3rd column respectively) and PRESTO (4th column) using the optimal strategy for measurements outside the vessel. Different rows represent different vessel sizes, diameters (respectively 4 mm, 3 mm and 2 mm).

In vivo example

Figure 7 shows the ΔR_2^* bolus-passage measured in the voxels close to the MCA (middle profile is encompassing the vessel). The thicker lines are the predicted optimal locations from the simulations for AIF selection. Notice, that signs of PVEs, like peaks on the ΔR_2^*-curves are almost absent in the selected curves. For the PRESTO sequence it is obvious that voxels closest to the vessel, show most artifacts. Voxels located superior or inferior from the MCA show still reasonable signal strength without erroneous peaks, although the SNR is lower than for voxels in and next to the MCA. The AIF measurements obtained from segmented EPI TE_1 (middle panel) show for a large region in and around the MCA curves with little to no shape errors. This is in good agreement with the simulations. However, the signal strength of the curves is higher outside the MCA than predicted from the simulations. For segmented EPI TE_2 (lower panel) the signal strength in the voxel encompassing the MCA is lower than the signal strength in the voxels located anterior or posterior from the MCA as expected from the simulations. The shape in the voxels directly anterior or posterior from the MCA is also free of peaks or signs of PVEs. This is also in agreement with the simulations.

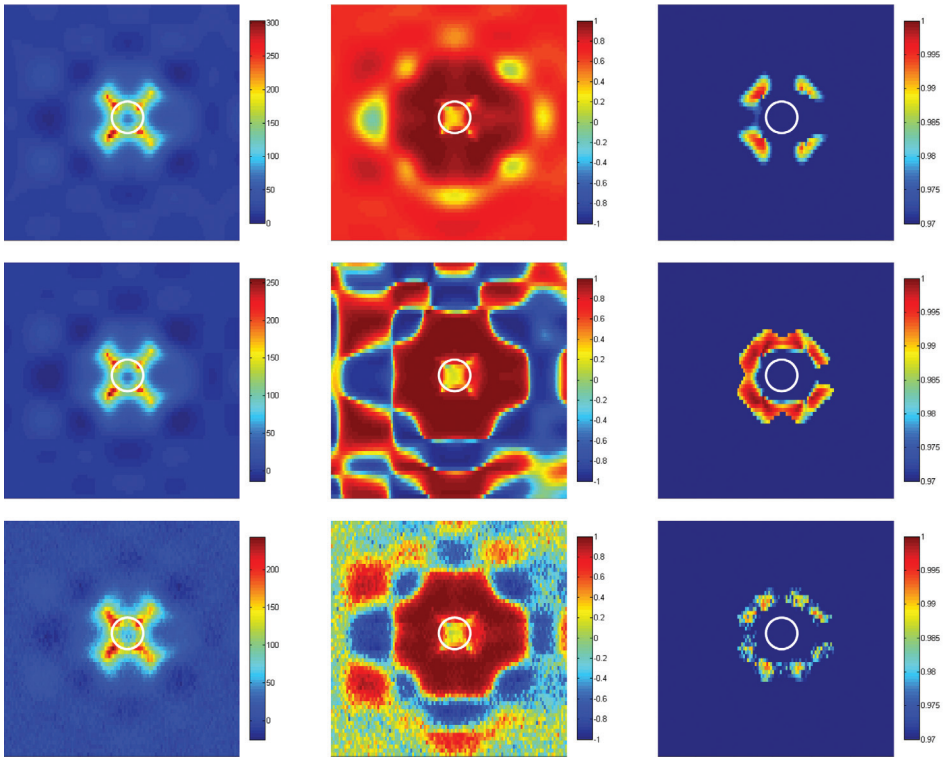

Figure 6: The relative signal strength (RSS in percent; left column), the correlation (middle column) and the RSS-thresholded correlation image (correlation coefficient larger than 0.97 and RSS larger than 25%; right column) for PRESTO at 3.0 Tesla using out-vessel strategy (first row), out-vessel strategy with tissue subtraction (second row) and with noise included in the simulations (SNR=25 using out-vessel strategy with tissue curve subtraction; last row).

DISCUSSION AND CONCLUSIONS

The main findings of this study are fourfold. First, AIF measurements near the MCA are best performed in voxels located completely outside the artery, within tissue surrounding the MCA. Second, a linear relation between ΔR_2^* and the concentration of Gd-DTPA is the best assumption when measuring the AIF in voxels that are not completely located inside the MCA. Third, the position with respect to the MCA that yields a correct AIF measurement depends on the particular imaging sequence, echo time and diameter of the MCA. Finally, AIF measurements can also be performed in voxels that encompass the MCA for a specific combination of small MCA and short echo time (TE_1) when using a segmented EPI readout.

In this study, we focused on finding the optimal location for AIF selection near the MCA based on theoretical modeling and evaluated this finding in an in vivo example. Using the MCA for AIF selection has several advantages; the MCA is almost always located inside the imaging

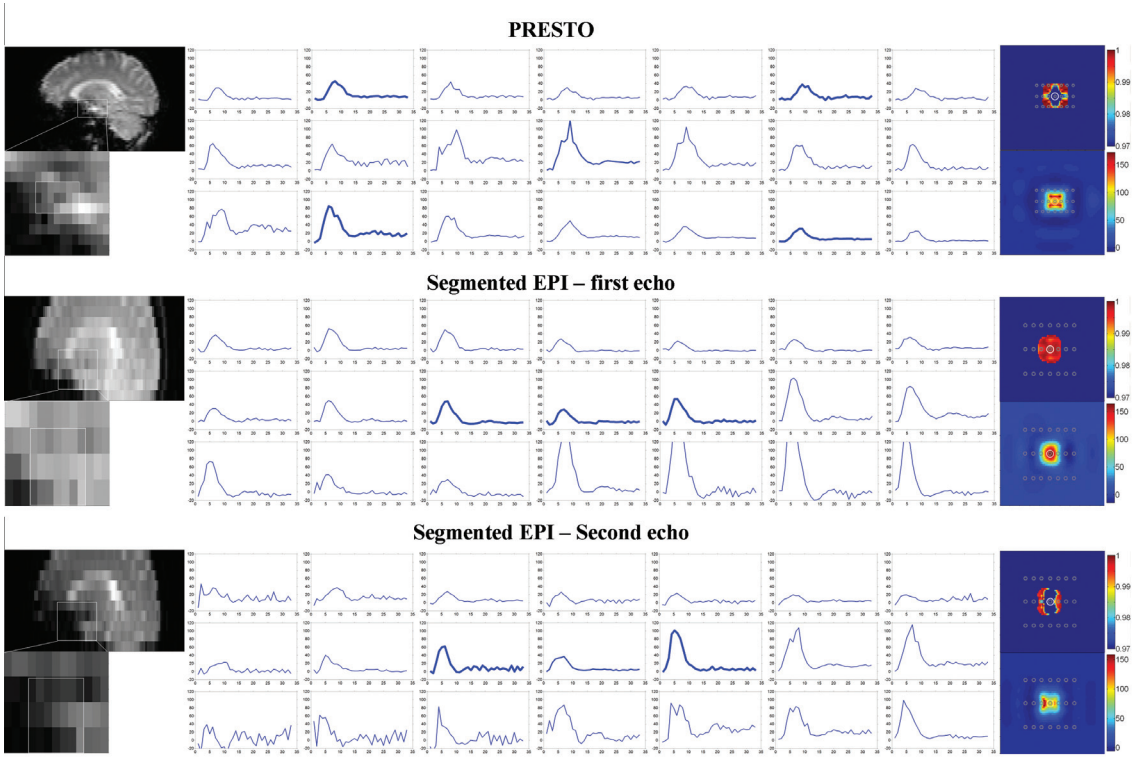

Figure 7: In vivo example of AIF selection near the MCA. A straight part of the MCA angulated perpendicular to the main magnetic field was visually identified on the 3D T_1-weighted scan and this location was transformed to the gradient echo images; PRESTO and dual echo segmented EPI. ΔR_2^*-curves were plotted for voxels located around the MCA for the PRESTO sequence and the first (TE_1) and second (TE_2) echo time of the segmented EPI sequence. The voxel on top of the MCA was indicated with a thicker than normal line. Based on the findings in the simulation study, the curves from the optimal location for AIF measurements were plotted with thickest lines. The corresponding simulation results are shown on the right side (thresholded correlation maps and relative signal strength), with the approximate location of the voxels indicated by gray circles.

volume, whereas AIF measurements in the ICA require the acquisition of an additional slice; second, the angle between the vessel axis and the main magnetic field is approximately 90°, resulting in maximal signal change in the surrounding tissue.

This study shows that AIF measurements are best performed in tissue near the MCA rather than in voxels that partly encompass the artery. This finding can be counterintuitive because in the brain, the contrast agent resides intravascular and therefore one may be tempted to assume that voxels within an artery provide the best opportunity for measuring the AIF. However, the presence of contrast agent within the MCA causes local magnetic field changes inside and outside the vessel and thus also affects the gradient echo MR-signal outside the vessel. Furthermore, AIF measurements encompassing or partly in the MCA are hampered by PVEs. When the bolus contrast agent passes through the artery and alters the relaxivity, this leads to a smaller transverse relaxation rate for the intravascular compartment and the phase of this compartment will change because of altered susceptibility. The presence of contrast agent within the MCA will also lead to magnetic field changes in the surrounding tissue. Averaging over the extravascular compartment will therefore lead to dephasing and a general shift in phase of the signal will occur.

When the total signal of partial volume voxels is formed, the contributions of the two compartments can add either constructively or destructively, depending on the relative phase difference between the two compartments. Destructive addition of the intra- and extravascular signal can lead to almost zero total signal, resulting in a high value of ΔR_2^*, showing as a sharp peak in the ΔR_2^* curves. Such peaks in the ΔR_2^* profiles can be observed in the simulation as well as in the in vivo AIF measurements (Figures 3 and 7). Figure 3 also shows that PVEs can lead to smaller widths or higher peaks in the ΔR_2^* profile, illustrating that AIF selection rules based on a small width or maximum height of the ΔR_2^* profile do not always exclude voxels that exhibit partial volume effects.

The effect of errors in shape of the measured AIF on CBF and the influence of the deconvolution technique has been studied by Calamante et al. (30). It was concluded that the influence of erroneous AIF measurement on the CBF was highly dependent on the type of shape changes of the AIF, e.g. a too steep rise of the AIF resulted in the highest errors in CBF (30). The advanced model simulations show correct measurements of shape of the AIF near the MCA as evidenced by high correlation values with the ground truth. It is difficult to relate the correlation with the expected errors in CBF measurements, since these will depend strongly on the used deconvolution technique (1, 2, 31), especially as each deconvolution techniques employs a different approach to suppress noise. To avoid the influence of a particular deconvolution technique on our results, it was chosen to use a quality parameter of the shape of the AIF instead. A correct shape of the AIF will yield correct relative CBF and CBV values, and correct absolute MTT values, because CBV and CBF scale equally with the amplitude of the AIF. When using an additional method for quantitative CBV measurements (e.g. Bookend-Method (32)) or quantitative CBF measurement (like arterial spin labeling, (33)) all perfusion measures can be quantified.

We used three different strategies for the conversion of MR-signal changes to the concentration of Gd-DTPA. In the first strategy a quadratic relation between ΔR_2^* and the concentration of contrast agent was used, which is in correspondence with the relation as measured in whole blood (13) (a strategy optimized for intravascular AIF measurements). The second strategy is optimized for AIF measurements in tissue in the direct vicinity of the artery. Traditionally, a linear relaxivity constant is used for AIF measurements outside the artery and this approach was therefore adopted for the second strategy. However, voxels located outside the MCA are not only subjected to signal changes caused by the presence of contrast agent within the MCA, but experience also signal changes due to the passage of contrast agent through the microvasculature of the tissue. Therefore a third strategy was employed using a previously proposed method to reduce the effect of the tissue passage (29). This approach is based on the subtraction of the ΔR_2^* curve of pure gray matter from the measured AIF. When our simulations were performed without noise, tissue subtraction resulted in almost complete elimination of the tissue passage curve from the measured AIF (Figure 3). However, for the simulation that included noise, tissue subtraction did not improve the shape and induce sometimes even undesired errors in shape. It can therefore be concluded that the out-vessel strategy without tissue curve subtraction provided the best opportunities for a correct AIF measurement, but improved tissue subtraction approach does certainly provide opportunities for even better AIF measurements. The simulations also show that a linear relation between ΔR_2^* and the concentration contrast agent is indeed the best assumption when converting MR signal changes into concentration-time curves for AIF measurements outside the MCA.

The exact location for optimal AIF measurement in the tissue surrounding the MCA differs for the various sequences that were studied. Voxels for AIF measurements using PRESTO should be selected above or beneath the vessel and posterior or anterior to the vessel. For single-shot EPI, the optimal location is found in tissue posterior to the vessel. For certain positions of the vessel center within the imaging slices none of the voxels fulfilled our criteria when using single-shot EPI. Segmented EPI showed more feasible locations for AIF measurements. For the second echo time, correct locations are found both anterior and posterior to the vessel, and are in some cases found in the slice superior or inferior to the MCA. When using the first echo time the best locations are found closer to the vessel. For a relatively small MCA (Ø 2 mm), short-echo segmented EPI also gives correct AIF measurements for voxels partly in the MCA.

Imaging using longer echo times causes larger signal drops both inside and outside the vessel. For these longer echo times, the intravascular signal drops into the noise level for relatively small concentrations of contrast agent. The relative contribution of the intra- versus extravascular compartments will therefore change significantly when measuring the AIF in voxels encompassing the MCA, leading to an erroneous shape. However, also the extravascular signal will at some point drop into the noise-level, at which point noise will dominate the ΔR_2^* measurement, thereby affecting the shape of the curve, especially the peak, dramatically. Therefore not only PVEs but also signal saturation and noise can lead to errors in the measured shape of

the AIF. The influence of the echo time on the occurrence of signal saturation can be observed in the results of the dual echo segmented EPI (Figure 5), which show optimal locations for AIF measurement much closer or even on top of the MCA for the small echo time compared to the longer echo time. This can be explained by the fact that the extent of the field inhomogeneities increase with longer echo times, leading to signal saturation at larger distances from the vessel center. The finding of correct AIF measurements, using segmented EPI with a short echo time, on top of the MCA could be useful for local AIF selection-methods, where AIF measurements are performed at the level of small arteries that supply the adjacent tissue with blood. However, further research is required to determine the effect of the orientation and the exact size of the small artery on the shape of the AIF measurements.

The findings from the simulations were subsequently applied to an in vivo example (Figure 7). Although in general the findings of the simulations were reproduced in this in vivo example, some discrepancies were observed. In our opinion, these differences can be explained by uncertainties in the exact location of the MCA in the DSC images, as movement of the patient and distortions of the MR images can lead to misidentification of the location of the MCA. However, several important observations can be made from this example. First, the short echo time of the segmented EPI sequence, did indeed lead to a large region around the MCA where the AIF can be measured without suffering from PVEs, like erroneous peaks on the AIF. When comparing the short echo time data with the second echo time, it is clear that the number of voxels showing correct AIF shape is much lower when using the longer echo time. Second, the PRESTO data (upper panel) show that AIF measurements can indeed better be performed in the slice above or below the MCA, as voxels in these curves show less erroneous deformations than the voxels located in the same slice as the MCA. Furthermore, it is clear that the SNR of a single voxel is too low when using it as input for the deconvolution analysis. In general, the SNR of the AIF can be improved by averaging a number of AIF measurements with correct shape, e.g. along the MCA or in voxels around the MCA (when using segmented EPI with a short echo time). However, care should be taken to avoid voxels where smaller arteries branch off the MCA.

All phantom experiments performed on 1.5 T resemble a concentration dose of 0.2 mmol/kg-bodyweight Gd-DTPA. The in vivo experiments performed at 3.0 T used 0.1 mmol/kg-bodyweight Gd-DTPA. The susceptibility changes, field strength and echo train length have the largest contribution to the pattern of signal decreases observed in and outside the vessel for gradient echo images. With double the field strength and half the concentration Gd-DTPA the signal decrease patterns will remain comparable, as both effects cancel out, although other differences (e.g. resulting from differences in relaxation rates and values) might lead to discrepancies. Nonetheless, when repeating the simulations for 3.0 Tesla with half the dose of contrast agent, the same optimal locations were found as observed in the simulations of 1.5 T (compare Figures 4 and 6).

The advanced numerical model was designed to closely resemble in vivo AIF selection in or near the MCA, still some assumptions had to be made. First, the MCA was modeled as an

infinite cylinder oriented perpendicular to the main magnetic field; therefore the conclusions only holds for a straight part of the MCA at least 4 times the diameter (34). The cardiac effects on the MCA were not taken into account. Imaging with single-shot EPI takes on the order of 0.1 seconds and can be considered as a snapshot compared to the cardiac cycle (approximately 0.8 sec). PRESTO was used as a 3D sequence and takes about 2 cardiac cycles (1.5 or 2 seconds), however the large gradients used for echo shifting crush the intravascular signal.

In summary, AIF measurements are best performed using the short echo time in combination with segmented EPI. For this setup a large area around the MCA provide AIF curves with little errors because of PVEs and signal depletion, leading to the best measurement of the shape of the AIF. In most situations, the AIF measurement is best performed in voxels located completely in tissue surrounding the MCA. Segmented readout sequences such as segmented EPI or PRESTO result in more possible locations for AIF selection and are less sensitive to the exact position of the vessel in the through-plane direction than single-shot EPI. For most sequences, the best location for AIF measurements is posterior to the vessel and is for some cases found in the slice superior to the MCA. Converting the profile to concentration is best performed using a linear relation when measuring outside the artery.

REFERENCES

1. Ostergaard L, Weisskoff RM, Chesler DA, Gyldensted C, Rosen BR. High resolution measurement of cerebral blood flow using intravascular tracer bolus passages .1. Mathematical approach and statistical analysis. Magnetic Resonance in Medicine 1996;36(5):715-725.
2. Rempp KA, Brix G, Wenz F, Becker CR, Guckel F, Lorenz WJ. Quantification of Regional Cerebral Blood-Flow and Volume with Dynamic Susceptibility Contrast-Enhanced Mr-Imaging. Radiology 1994;193(3):637-641.
3. Hakyemez B, Erdogan C, Bolca N, Yidirim N, Gokalp G, Parlak M. Evaluation of different cerebral mass lesions by perfusion-weighted MR imaging. Journal of Magnetic Resonance Imaging 2006;24(4):817-824.
4. Harris GJ, Lewis RF, Satlin A, English CD, Scott TM, Yurgelun-Todd DA, Renshaw PF. Dynamic susceptibility contrast MR imaging of regional cerebral blood volume in Alzheimer disease: A promising alternative to nuclear medicine. American Journal of Neuroradiology 1998;19(9):1727-1732.
5. Kluytmans M, van der Grond J, Eikelboom BC, Viergever MA. Long-term hemodynamic effects of carotid endarterectomy. Stroke 1998;29(8):1567-1572.
6. Sorensen AG, Copen WA, Ostergaard L, Buonanno FS, Gonzalez RG, Rordorf G, Rosen BR, Schwamm LH, Weisskoff RM, Koroshetz WJ. Hyperacute stroke: Simultaneous measurement of relative cerebral blood volume, relative cerebral blood flow, and mean tissue transit time. Radiology 1999;210(2):519-527.
7. Calamante F, Gadian DG, Connelly A. Delay and dispersion effects in dynamic susceptibility contrast MRI: Simulations using singular value decomposition. Magnetic Resonance in Medicine 2000;44(3):466-473.
8. Akbudak E, Conturo TE. Arterial input functions from MR phase imaging. Magnetic Resonance in Medicine 1996;36(6):809-815.
9. Perman WH, Gado MH, Larson KB, Perlmutter JS. Simultaneous Mr Acquisition of Arterial and Brain Signal Time Curves. Magnetic Resonance in Medicine 1992;28(1):74-83.
10. Carroll TJ, Rowley HA, Haughton VM. Automatic calculation of the arterial input function for cerebral perfusion imaging with MR imaging. Radiology 2003;227(2):593-600.
11. Mouridsen K, Christensen S, Gydensted L, Ostergaard L. Automatic selection of arterial input function using cluster analysis. Magnetic Resonance in Medicine 2006;55(3):524-531.
12. van Osch MJP, van der Grond J, Bakker CJG. Partial volume effects on arterial input functions: shape and amplitude distortions and their correction. Journal of Magnetic Resonance Imaging 2005;22(6):704-709.
13. van Osch MJP, Vonken EJPA, Viergever MA, van der Grond J, Bakker CJG. Measuring the arterial input function with gradient echo sequences. Magnetic Resonance in Medicine 2003;49(6):1067-1076.
14. Liu GY, Sobering G, Duyn J, Moonen CTW. A Functional Mri Technique Combining Principles of Echo-Shifting with A Train of Observations (Presto). Magnetic Resonance in Medicine 1993;30(6):764-768.
15. Monson KL, Goldsmith W, Barbaro NM, Manley GT. Significance of source and size in the mechanical response of human cerebral blood vessels. Journal of Biomechanics 2005;38(4):737-744.
16. Serrador JM, Picot PA, Rutt BK, Shoemaker JK, Bondar RL. MRI measures of middle cerebral artery diameter in conscious humans during simulated orthostasis. Stroke 2000;31(7):1672-1678.
17. van Osch MJP, Hendrikse J, Golay X, Bakker CJG, van der Grond J. Non-invasive visualization of collateral blood flow patterns of the circle of Willis by dynamic MR angiography. Medical Image Analysis 2006;10(1):59-70.
18. Akbudak, E, Hsu, RM, Li, Y, and Conturo, TE. $\Delta R2^*$ or $\Delta\varphi$ contrast agent perfusion effects in blood: quantitation and linearity assessment. In:Proceedings of the ISMRM 6th Annual Meeting, Sydney, 1998, p1197.

19. Pintaske J, Martirosian P, Graf H, Erb G, Lodemann KP, Claussen CD, Schick F. Relaxivity of gadopentetate dimeglumine (Magnevist), gadobutrol (Giadovist), and gadobenate dimeglumine (MultiHance) in human blood plasma at 0.2, 1.5, and 3 Tesla. Investigative Radiology 2006;41(3):213-221.
20. Kjolby BF, Ostergaard L, Kiselev VG. Theoretical model of intravascular paramagnetic tracers effect on tissue relaxation. Magnetic Resonance in Medicine 2006;56(1):187-197.
21. Morkenborg J, Taagehoj JF, Vaever PN, Frokiaer J, Djurhuus JC, Stodkilde-Jorgensen H. In vivo measurement of T-1 and T-2 relaxivity in the kidney cortex of the pig - Based on a two-compartment steady-state model. Magnetic Resonance Imaging 1998;16(8):933-942.
22. Calamante F, Vonken EJPA, van Osch MJP. Contrast agent concentration measurements affecting quantification of bolus-tracking perfusion MRI. Magnetic Resonance in Medicine 2007;58(3):544-553.
23. Haacke EM. MRI: basic principles and application. Wiley; 1999.
24. Pedersen M, Klarhofer M, Christensen S, Ouallet JC, Ostergaard L, Dousset V, Moonen C. Quantitative cerebral perfusion using the PRESTO acquisition scheme. Journal of Magnetic Resonance Imaging 2004;20(6):930-940.
25. Golay X, Petersen ET, Hui F. Pulsed star labeling of arterial regions (PULSAR): A robust regional perfusion technique for high field imaging. Magnetic Resonance in Medicine 2005;53(1):15-21.
26. Lu HZ, Clingman C, Golay X, van Zijl PCM. Determining the longitudinal relaxation time (T-1) of blood at 3.0 tesla. Magnetic Resonance in Medicine 2004;52(3):679-682.
27. Duhamel G, Schlaug G, Alsop DC. Measurement of arterial input functions for dynamic susceptibility contrast magnetic resonance imaging using echoplanar images: Comparison of physical simulations with in vivo results. Magnetic Resonance in Medicine 2006;55(3):514-523.
28. van Osch MJP, Vonken EJPA, Wu O, Viergever MA, van der Grond J, Bakker CJG. Model of the human vasculature for studying the influence of contrast injection speed on cerebral perfusion MRI. Magnetic Resonance in Medicine 2003;50(3):614-622.
29. Thornton RJ, Jones JY, Wang ZYJ. Correcting the effects of background microcirculation in the measurement of arterial input functions using dynamic susceptibility contrast MRI of the brain. Magnetic Resonance Imaging 2006;24(5):619-623.
30. Calamante F. DSC-MRI: How accurate does the arterial input function need to be in practice? In: Connelly A, editor. Pro. Int. Soc. Mag. Reson. Med. 15; 2007.
31. Vonken EJPA, van Osch MJP, Bakker CJG, Viergever MA. Simultaneous quantitative cerebral perfusion and Gd-DTPA extravasation measurement with dual-echo dynamic susceptibility contrast MRI. Magnetic Resonance in Medicine 2000;43(6):820-827.
32. Sakaie KE, Shin W, Curtin KR, McCarthy RM, Cashen TA, Carroll TJ. Method for improving the accuracy of quantitative cerebral perfusion imaging. Journal of Magnetic Resonance Imaging 2005;21(5):512-519.
33. Williams DS, Detre JA, Leigh JS, Koretsky AP. Magnetic-Resonance-Imaging of Perfusion Using Spin Inversion of Arterial Water. Proceedings of the National Academy of Sciences of the United States of America 1992;89(1):212-216.
34. Bhagwandien R, Moerland MA, Bakker CJG, Beersma R, Lagendijk JJW. Numerical-Analysis of the Magnetic-Field for Arbitrary Magnetic-Susceptibility Distributions in 3D. Magnetic Resonance Imaging 1994;12(1):101-107.

Chapter 4: Phase-based arterial input function measurements for dynamic susceptibility contrast MRI

Egbert JW Bleeker, Mark A van Buchem, Andrew G Webb, and Matthias JP van Osch

ABSTRACT

In dynamic susceptibility contrast (DSC-) MRI arterial input function (AIF) measurements using the phase of the MR signal are traditionally performed inside an artery. However, phase-based AIF selection is also feasible in tissue surrounding an artery such as the middle cerebral artery (MCA), which runs approximately perpendicular to B_0, since contrast agents also induce local field changes in tissue surrounding the artery. The aim of this study was to investigate whether phase-based AIF selection is better performed in tissue just outside the MCA than inside the artery. Additionally, phase-based AIF selection was compared to magnitude-based AIF selection. Both issues were studied theoretically and using numerical simulations, producing results which were validated using phantom experiments. Finally, an in vivo experiment was performed to illustrate the feasibility of phase-based AIF selection. Three main findings are presented: first, phase-based AIF selections are better made in tissue outside the MCA rather than within the MCA, since in the latter approach partial volume effects affect the shape of the estimated AIF. Second, optimal locations for phase-based AIF selection are similar for different clinical DSC-MRI sequences. Third, phase-based AIF selection allows more locations in tissue to be chosen which show the correct AIF than does magnitude-based AIF selection.

Published in Magnetic Resonance in Medicine (2010) Aug; 64(2):358-68

INTRODUCTION

First-pass perfusion MRI, also termed dynamic susceptibility contrast MRI (DSC-MRI), is used in clinical practice to diagnose brain disease and to stage its severity (1, 2). DSC-MRI provides a set of hemodynamical parameters such as cerebral blood flow (CBF), cerebral blood volume (CBV), mean transit time (MTT), time of arrival (TA) and time to peak (TTP), (3, 4). However, the values of CBF, CBV and MTT obtained with DSC-MRI are qualitative rather than quantitative. One of the key elements currently missing is an accurate measurement of the arterial input function (AIF), an estimate of the concentration of contrast agent as it passes through an artery close to the brain tissue.

The AIF can be measured using the change in magnitude or the phase ($\Delta\varphi$) of the MR-signal. Signal processing involves the magnitude of this signal change being transformed to ΔR_2^*. Phase-based AIF selection within a brain-feeding artery was first proposed more than a decade ago (5), but up to now clinical applications have been limited. Phase-based AIF measurements have several potential advantages over magnitude-based AIF measurements. First, the phase is linearly related to the concentration of contrast agent in blood, and the linearity is independent of the hematocrit level (6, 7), whereas for magnitude-based AIF measurements there is a quadratic relation between ΔR_2^* of whole blood and the concentration of contrast agent with the quadratic component dependent on the hematocrit level (8, 9). Second, the phase-based AIF measurement is expected to be more precise with a ten-fold signal-to-noise (SNR) increase compared to magnitude-based AIF selection averaged over the entire curve (10).

The original studies of Akbudak and Conturo were limited to phase-based AIF measurements within the artery (5), although phase-based AIF measurements can also be performed in surrounding tissue, since magnetic field changes are also induced outside arteries that are not oriented parallel to B_0 by the presence of contrast agent within the vessel (11). Furthermore, several potential advantages can be anticipated for phase-based AIF measurements outside the artery. First, voxels located completely in tissue are not affected by partial volume effects with the arterial signal, whereas partial volume effects between artery and tissue often lead to errors in the shape of the AIF profile (12, 13). Second, outside the artery signal dephasing is less severe, resulting in an increased precision of the phase-determination since the noise in the phase of the MR-signal depends inversely on the magnitude of the signal. A potential drawback for phase-based AIF measurements in tissue could be the contamination of the AIF with the passage of the contrast agent through the capillaries (also referred to as the tissue response) as has been observed in magnitude-based AIF measurements in tissue (14). However, it is expected that for phase-based AIF measurements this effect will be minimal, since capillaries in a given voxel are likely to be oriented randomly and phase effects therefore cancel.

The aim of this study is to determine whether phased-based AIF measurements in tissue are advantageous compared to phase-based AIF measurements in an artery. Additionally, extravascular phase-based AIF measurements are compared to extravascular magnitude-based AIF measurements. This study focuses on AIF measurements in the vicinity of the middle cerebral

artery (MCA), which is ideally suited for AIF determination due to its size, location in the brain and the orientation perpendicular to the main magnetic field. Equations for susceptibility effects in and around straight vessels were used to create a numerical model. Different effects that can lead to errors in the shape of the AIF such as partial volume, signal cancellation, image distortions (including the apparent vessel shift), and the point spread function of the particular imaging sequence were investigated using this numerical model. The numerical model has previously been validated for magnitude-based AIF measurements (15) and in the current study the numerical model is evaluated for phase-based AIF measurements. The findings obtained from the simulations are confirmed using an in vivo DSC-MRI exam.

THEORY

Contrast agents employed in DSC-MRI have a higher susceptibility than blood and change both the longitudinal and transverse relaxation times of nearby water. The intravascular susceptibility is linearly related to the concentration of contrast agent and changes the local magnetic field (9, 16). For an infinite cylinder,

$$\Delta B_{\text{int}} = \frac{\delta\chi \cdot [Gd]}{6}\left(3\cos^2\theta - 1\right)B_0 \qquad [1]$$

$$\Delta B_{ext} = \frac{\delta\chi \cdot [Gd]}{2}\left(\left(\frac{a}{\rho}\right)^2 \sin^2\theta \cdot \cos 2\varphi\right)B_0 \qquad [2]$$

where ΔB_{int} is the magnetic field change inside the vessel, ΔB_{ext} is the magnetic field change outside the vessel, $\delta\chi$ is the susceptibility difference per mole per liter of gadolinium between the intra- and extravascular compartments, [Gd] is the concentration of gadolinium, a is the radius of the vessel, ρ is the distance from any given point (p) to the vessel center, θ is the angle between the vessel axis and B_0, and φ is the angle of p in the plane perpendicular to the vessel axis.

From these formulae, it can be seen that intravascular phase-based AIF measurements of arteries such as the internal carotid artery, which are oriented parallel to the main magnetic field, have twice the induced contrast compared to intravascular phase-based AIF measurements inside arteries, such as the MCA, which are oriented perpendicularly. However, the magnetic field in the tissue surrounding the perpendicular-oriented artery is also affected and at some locations these magnetic field changes are even larger than the intravascular field changes for a parallel oriented artery. Larger magnetic field changes lead to larger phase changes and therefore to higher SNR in the phase difference images, assuming that the temporal phase changes can still be accurately unwrapped. The phase signal change between two time points is dependent on three factors: the echo time, change in contrast agent concentration, and the

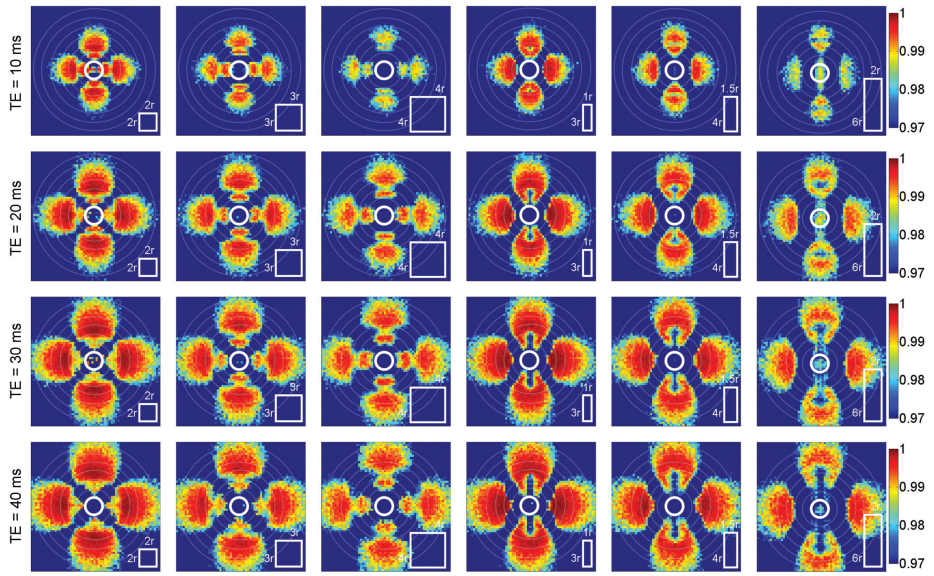

Figure 1: Assessment of the shape errors in the phase-based AIF measurements based on the theoretical equations of magnetic field changes around an infinite cylinder (Eq 1, 2). Shown are the optimal locations for phase-based AIF measurements for several echo times based on the correlation with the ground truth (the absolute value of the correlation greater than 0.97). The columns correspond to different relative voxel sizes with respect to the radius of the vessel while assuming an ideal point spread function. The gray circles show the distance from the vessel center in steps of the radius. The white rectangles depict the voxel size.

distance from the vessel center (see equation 2). Due to the dependence on the change in concentration, the phase signal change is also dependent on the dynamic scan time.

Acquisition of DSC-MRI is characterized by a relatively coarse spatial resolution due to the necessity of a high temporal resolution. Therefore, partial volume effects will occur in the neighborhood of the MCA and a set of numerical simulations using the theory for an infinite cylinder oriented perpendicular to the main magnetic field (see equations 1 and 2) was used to gain insight into how partial volume effects affect phase-based AIF measurements. Gaussian noise was added to the real and imaginary part of the complex signal with an SNR of 50:1 and an ideal point spread function was assumed. In figure 1 the absolute correlation with the "ground truth" of the concentration profile derived from a modeled AIF (17) is presented for different voxel sizes, and for different echo times (10, 20, 30, 40 msec). Longer echo times allow measurements of the AIF more distant from the cylinder, up to 6 times the radius for an echo time of 40 msec, in comparison to 4 times the radius for an echo time of 10 msec. Voxels partly encompassing the cylinder have partial volume effects, which corrupt the shape of the estimated AIF. For smaller voxel sizes, the AIF measurements with the correct shape can be found closer to the arterial wall. In general, the locations for correct AIF measurements are superior, posterior, inferior and anterior to the cylinder.

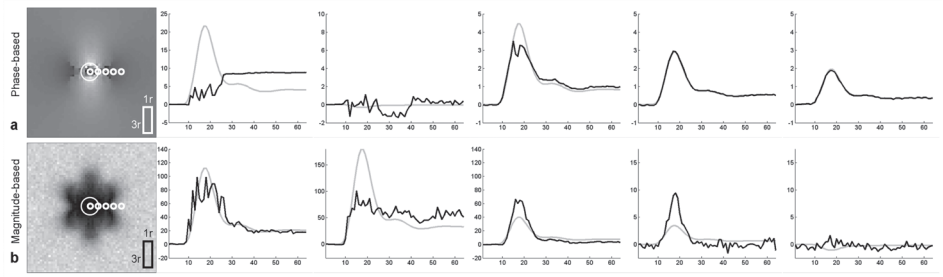

Figure 2: Simulated AIF measurements for phase-based (Δφ) AIF measurements (**a**) and magnitude-based (ΔR_2^*) AIF measurements (**b**); the left panel shows the phase and magnitude image at the peak contrast agent concentration. The sign of the phase-based profiles is reversed so that the phase change is positive. The first two profiles of the phase-based and magnitude-based AIF measurement show partial volume effects because these are partly encompassing the MCA. The third profile is suffering from signal saturation, which corrupts the peak concentrations. The fourth and fifth profiles of the phase-based AIF measurement have the correct shape of the concentration profile but the SNR is reduced. In all graphs, the ground truth rescaled to the area-under-the-curve of each profile is shown in gray.

A series of phase-based and magnitude-based AIF shapes are presented in figure 2. The voxels close to the center of the cylinder have large shape errors. The voxels more distant from the center have reduced scaling.

METHODS

In a previous report a numerical model described magnitude-based AIF selection in and near the MCA (15). The numerical model has been validated for magnitude-based AIF selection, and in the current study, the numerical model was evaluated for phase-based AIF selection.

An extended numerical model was used for in vivo prediction using numerical values more appropriate to the in vivo case. This "in vivo" model was employed to study magnitude-based and phase-based AIF selection in and near the MCA. Finally, an example of an in vivo experiment was used to confirm the results from the simulations.

Numerical models including imaging effects

The M1 segment of the MCA was modeled as an infinite cylinder perpendicular to the main magnetic field and parallel to the left/right axis. Partial volume effects and dephasing were modeled using a 250 μm high resolution 2D grid for 2D acquisition and a 500 μm 2D grid for 3D acquisition. Phase encoding was modeled explicitly to include image distortions, whereas frequency encoding was assumed to be instantaneous and ignored in the numerical model. Single shot EPI (voxel size 2.4x2.4x6 mm^3 zerofilled to 1.8x1.8x6 mm^3, TE 41 msec) and segmented double-echo EPI (voxel size 1.7x2.9x6 mm^3 zerofilled to 1.7x1.7x6 mm^3, TE_1/TE_2 11/30 msec) were modeled as 2D sequences, whereas PRESTO (Principles of echo-shifting with a train of observations (18))

was modeled as a 3D sequence (voxel size 3.4x3.5x3.5 mm^3 zerofilled to 1.7x1.7x3.5 mm^3, TE 25 msec). The numerical model was implemented in MATLAB (R2007b, Natick, MA, USA).

The basic model is based on bolus passage properties encountered in phantom experiments, whereas the "in vivo" model resembles in vivo AIF selection by including the passage of contrast agent through surrounding tissue and using relevant tissue parameters (whole blood transverse relaxivity $r_{2,blood}^{*}$ with a linear term 7.62 l/mmol/sec and a quadratic term 0.57 $l^2/mmol^2$/sec (9); the longitudinal relaxivity in tissue $r_{1,tissue}$ 4.3 l/mmol/sec (19); the transverse relaxivity in tissue $r_{2,tissue}^{*}$ 44 l/mmol/sec (20)). Gaussian noise was added to the real and imaginary part of the MR-signal to study the influence of noise on the shape of the AIF measurements. The baseline signal-to-noise ($SNR_{baseline}$) was set to 50:1, which is typical for clinical experiments.

Since the results do not depend on the position along the vessel, all results are presented in a sagittal view (although the model "acquires" transverse slices). In the model, the vessel center was shifted in small steps (500 µm) in both phase-encoding and slice direction. This shifting was performed to study the effect of the exact location of the vessel inside a voxel; the vessel center is shifted in smaller steps that the voxel size (see figure 3). These stacks with different locations of the vessel center were merged into a single image. Therefore, the resolution of this image appears to be higher but the pixels in the image actually represent normal clinical voxel sizes.

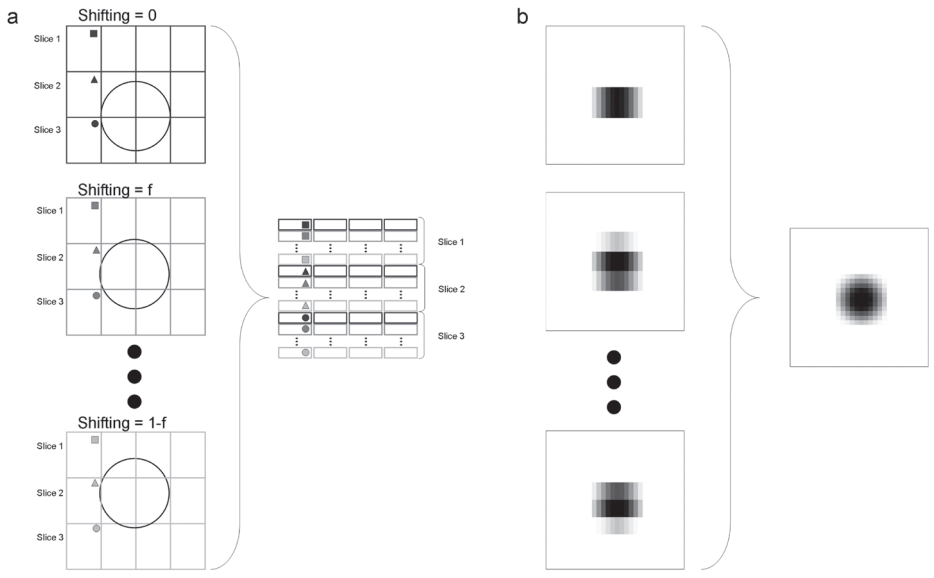

Figure 3: A schematic representation (**a**) is shown of shifting and merging in the slice direction; the different shifts are depicted in grayscales and slices are indicated by a symbol. In this example, the stacks of slices are shifted with a step size a quarter of the slice thickness. The merged image shows how the image is built up from the different shifts. The resolution appears to be higher for the merged image but each pixel reflects a voxel with original slice thickness. The image representation (**b**) of the shifting shows that the shifting leads to blurring of the underlying magnetization.

Post processing

The phase difference was calculated with respect to φ_0, the initial phase without contrast agent. For evaluation of the model three metrics were computed for each voxel and a fourth was constructed from the combination of two of these values. These metrics were:

1) The Pearson correlation coefficient (ρ), a measure for shape/accuracy with respect to the ground truth, defined as the expected intravascular phase change obtained from the analytical expression:

$$\Delta\varphi = 2\pi \cdot \gamma \cdot B_0 \cdot \delta\chi \cdot F_e \cdot TE \cdot [Gd], \qquad [3]$$

with $\gamma = 42.58$ MHz T^{-1} and $\delta\chi = 0.3209\ 10^{-3}$ l mol^{-1} (9), $F_e = -1/6$ for vessels perpendicular to the main magnetic field and TE the echo time.

2) The regression with the ground truth intravascular signal in percent, a measure for the relative scaling of $\Delta R_2^*(t)$ or $\Delta\varphi(t)$ with respect to the ground truth.
3) The SNRs of the contrast agent passage curve (SNR_{curve}) calculated as the ratio of the maximum of $\Delta R_2^*(t)$ or $\Delta\varphi(t)$ divided by the standard deviation of the pre-contrast agent images.
4) The values of the correlation and the SNR_{curve} were used to form a single image that shows locations in which a correct AIF measurement, that is with the correct shape and high SNR, could be obtained. Based on previous results, the cutoff value for the correlation to represent a correct shape was set to 0.97 (15). The SNR_{curve} was used to determine the locations with high precision; the threshold was set at 25 for both magnitude-based and phase-based AIF measurements.

Phantom experiments

The flow-phantom consisted of a tube (inner diameter 4 mm, wall thickness 0.25 mm) oriented perpendicular to the main magnetic field. $MnCl_2$-doped water was circulated through the tube at a constant volume flow rate of 2.8 ml/sec, which is close to the blood volume flow through the MCA (21). The T_1 value of the solution was close to the T_1 value of blood at 1.5 T. The tube was surrounded by the same $MnCl_2$ solution to create a background signal representing the tissue. In the solution within the tube, the concentration of Gd-DTPA (Magnevist, Schering, Germany) was increased in seventeen successive steps of 0.9 mM.

All phantom experiments were performed at 1.5 T (Philips Achieva, Best, The Netherlands) using a standard quadrature head coil. The imaging sequences had the following settings: single shot EPI, data matrix 96x95 zerofilled to 128x128, TE/TR 41/1500 msec, flip angle (FA) 80°, field of view (FOV) 230x230 mm^2, 15 slices of 6 mm thickness without interslice gap; dual echo segmented EPI, matrix 128x75 zerofilled to 128x128, TE_1/TE_2/TR 11/30/400 msec, FA 53°, FOV 220x220 mm^2, 8 slices of 6 mm thickness with 1 mm gap, 5 segments; PRESTO, matrix 64x63 zerofilled to 128x128, TE/TR 25/17 msec, FA 7°, FOV 220x220 mm^2, 30 slices of thickness 3.5 mm, 90 segments.

The stack of slices was shifted in steps of 1 mm (double the step size of the simulations) for the EPI and segmented EPI experiments and 0.5 mm for the PRESTO experiment in the slice direction in order to measure various locations of the vessel center within the imaging slice.

The phantom experiments were evaluated by the same procedure as the numerical models, although limited to the first two evaluation measures (Pearson correlation and regression with the ground truth).

In vivo experiment

As an in vivo example, a DSC-MRI experiment of a patient diagnosed with arteriovenous malformation (AVM) was used. The protocol was approved by the local ethics committee. Imaging was performed at 3 T (Philips Achieva, Best, The Netherlands) using a PRESTO sequence, matrix 96 x 87, zerofilled to 128 x 128, 30 slices 3.5 mm thick with no interslice gap, FOV 240 x 190 mm^2, 75 dynamic scans, scan duration 118 sec, TE/TR 30/20 msec, FA 8°, EPI factor 15, SENSE factor 2, phase encoding was set from right to left.

The locations of both left and right MCAs were determined (and found to be distant from the malformation) using the DSC-MRI data. The unwrapped phase AIF measurements and the magnitude-based AIF measurements in and around the arteries are presented, together with the results of the simulations. Because the exact concentration profile of the contrast agent is unknown, only qualitative evaluation can be performed.

RESULTS

First, the numerical model for phase-based AIF measurements was evaluated by means of phantom experiments (see figure 4). The sagittal images displayed are formed from several sets of transverse slices, which are shifted in the slice direction to study the influence of the location of the vessel inside the imaging volume. Figure 4a compares the $\Delta\varphi$ images of both model and phantom experiments at three different concentrations of contrast agent for the three sequences investigated. A visual comparison between the phantom results and simulations for single shot EPI (left two columns) and segmented EPI (middle two columns) show good agreement. When comparing the phantom measurements and simulations for PRESTO imaging a small discrepancy can be observed for voxels encompassing the vessel. This can probably be attributed to incomplete crushing of the intravascular signal by the gradients used for echo-shifting, whereas the model assumed complete crushing. Additionally, a quantitative evaluation was performed using the correlation and regression with the ground truth of the intravascular signal in percent, which is presented in figure 4b. These both show good agreement between model and phantom experiments although at large distance from the vessel differences can be observed, which can be explained by a small global phase drift. For single shot EPI, this global drift is more pronounced and results in a clear offset in the regression.

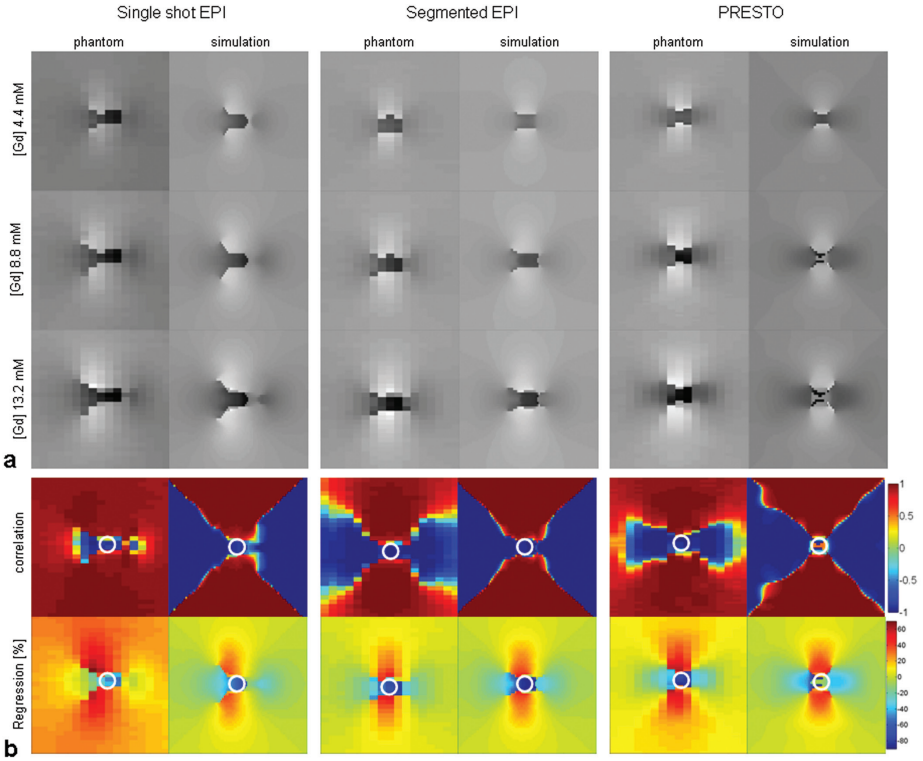

Figure 4: **a**) Merged Δφ images (sagittal view; FOV 30 x 30 mm) of the phantom experiments and the simulations for single shot EPI (left), segmented EPI (middle) and PRESTO (right) at three concentrations of Gd-DTPA (4.4 mM, 8.8 mM and 13.2 mM). **b**) Correlation (first row) and regression in percent with the ground truth, the expected intravascular signal, (second row) of phantom and simulations with the tube depicted as a white circle. The phantom images are formed by merging several stacks of transverse images into a single image and therefore each pixel represents a larger voxel. The phase encoding is oriented anterior to posterior. In the phantom experiments, the stack of slices was shifted in steps of 1 mm (single shot EPI and segmented EPI) and 0.5 mm (PRESTO). For the simulation, the stack of slices is shifted in all cases in steps of 0.5 mm and, in addition, the stack was also shifted in steps of 0.5 mm in the phase encoding direction. Although the resolution for the phantom and simulations appear different, the simulated and acquired voxel sizes are the same: the apparent resolution is different due to the smaller shifting step size of the simulation experiments.

The "in vivo" model was used for determining the optimal locations for AIF selection, as defined by a correct shape and high SNR_{curve}. Figure 5 shows a series of simulation data from a single shot EPI readout that describe the AIF measurement for both magnitude-based and phase-based AIF selection. The SNR_{curve} for phase-based AIF measurement is higher, which is in agreement with the results of Kotys et al. (10). For the magnitude-based AIF selection very few locations provide a correct AIF measurement, and all of these locations are outside the vessel. For phase-based AIF measurements, voxels with a correct shape and high SNR_{curve} are also located in tissue. In voxels more distant from the vessel, noise corrupts the shape of the

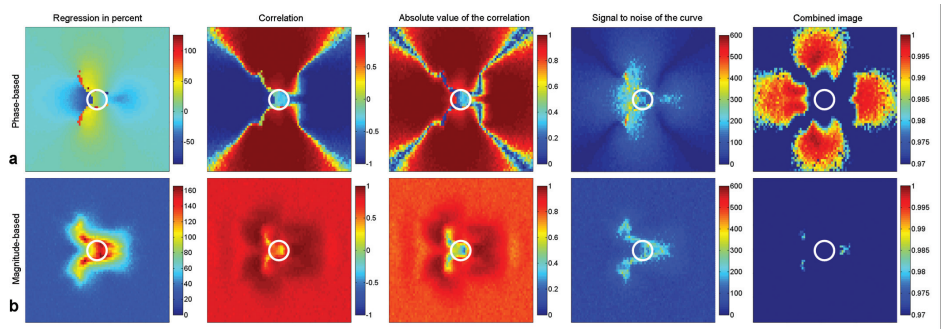

Figure 5: The regression with the ground truth in percent, correlation with the ground truth, absolute value of the correlation, SNR_{curve} (averaged over ten simulation runs) and combined image of correlation and SNR_{curve} (shown is a correlation larger than 0.97 in combination with an SNR larger than 25) for the phase-based AIF selection (**a**) and magnitude-based AIF selection (**b**).

AIF measurement, and when located more than 1.5 cm from the vessel center the SNR_{curve} becomes very low.

Different fast imaging sequences were investigated, each with different voxel sizes and exhibiting different distortion patterns (see figures 4 and 6). For both phase-based AIF selection as well as magnitude-based AIF selection, the locations with correct shape and high SNR_{curve} are in the tissue surrounding the MCA for all sequences studied. Furthermore, phase-based AIF selection results in a greater number of locations than magnitude-based AIF selection. The optimal locations for phase-based AIF selection are approximately the same for each of the different fast imaging sequences investigated. Shorter echo times induce less phase difference and therefore the area of bordering voxels is reduced (see figure 6) and the AIF measurement is thus more sensitive to the exact location of the vessel center inside the slice. For single shot and segmented EPI the optimal locations for AIF measurements are approximately three voxels (7.5-10 mm) posterior or anterior to the voxel encompassing the center of a 4 mm diameter MCA, and for the superior and inferior location the optimal locations are in the slice directly above or beneath the MCA. For a 2 mm diameter MCA the optimal location is approximately two voxels (5 mm) from the center of the MCA. For PRESTO with 3.5 mm isotropic voxels the optimal locations are closer to the MCA. For a 4 mm MCA the optimal locations are approximately two voxels (5-10 mm) posterior, anterior, inferior or superior to the center of the MCA and for a 2 mm MCA one voxel (2.5-5 mm) from the center of the MCA.

A PRESTO exam of a patient suffering from AVM was used for in vivo evaluation (see figure 7 and 8). In figure 7 negative phase changes are observed posterior and anterior to the MCA and positive phase changes are observed superior and inferior; this is in agreement with both theory and simulations. Diagonally to the vessel, there are no phase changes; this is also in agreement with theory and this shows that the tissue response of the signal phase is indeed close to zero. For both the left and right MCA there are partial volume effects, which hinder AIF measurements close to the artery (see figure 7). The AIF measurements near the right MCA also

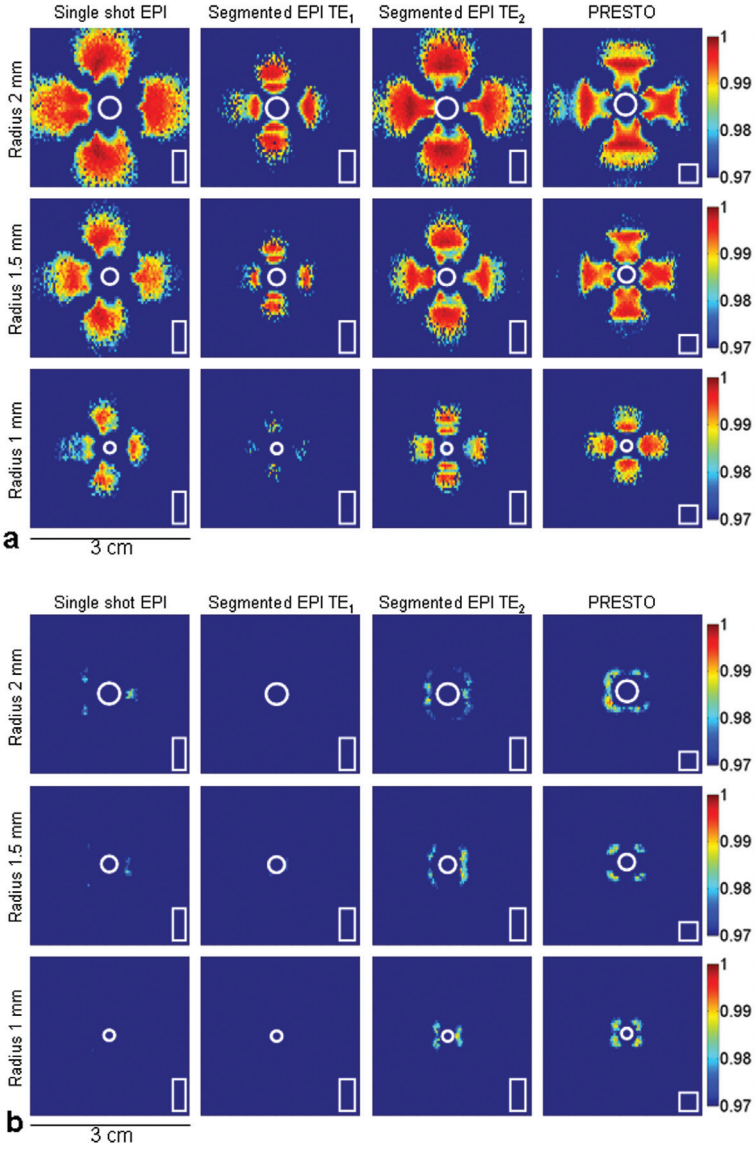

Figure 6: The optimal locations for **a**) phase-based AIF selection and **b**) magnitude-based AIF selection based on numerical modeling. The optimal locations were determined with SNR_{curve} thresholded correlation images (the absolute value of the correlation greater than 0.97 and a voxel with SNR_{curve} larger than 25). Respectively are shown single shot EPI (1st column), segmented EPI TE_1 (2nd column), segmented EPI TE_2 (3rd column) and PRESTO (4th column), for different diameters from top row to bottom row 4 mm, 3 mm and 2 mm. The white circle represents the location of the MCA. The white rectangle shows the true voxel size without zerofilling.

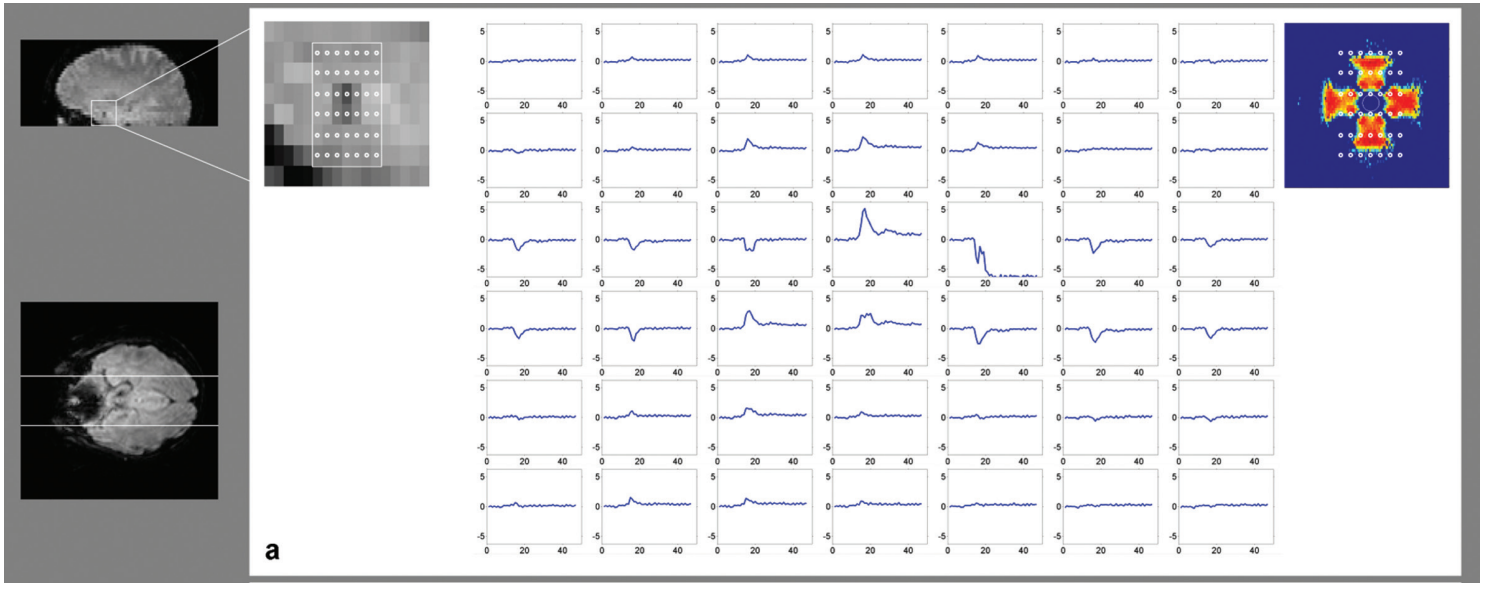
a

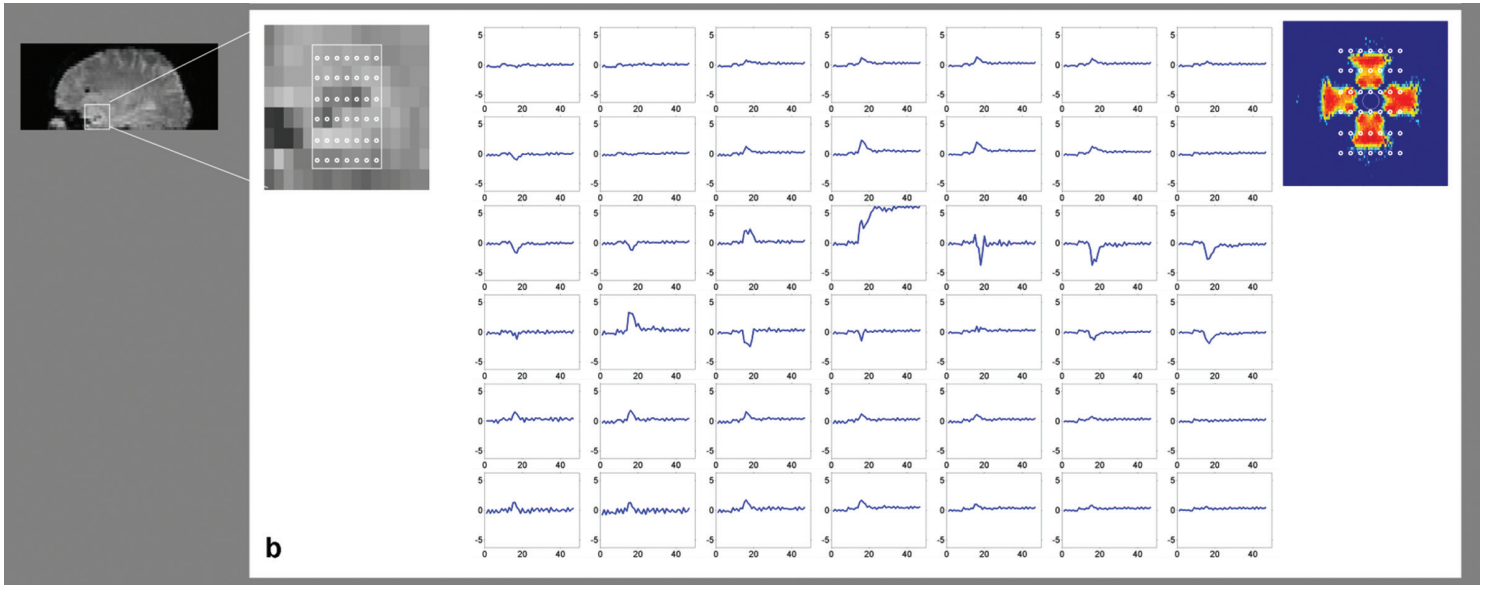

Figure 7: PRESTO DSC-MRI exam of a patient with arteriovenous malformation. Both left and right MCA were selected and the voxels in and around the MCA were used to plot the Δφ profiles for comparison with the findings of the "in vivo" model (presented right). The small white circles depict the estimated locations of the center of the voxel. The AIF measurements in the diagonal from the vessel center show very little phase change, which is in agreement with the assumption that phase changes in tissue are negligible. Voxels superior and inferior to the MCA have positive phase changes and anterior and posterior have negative phase changes, which is also in agreement with the simulations.

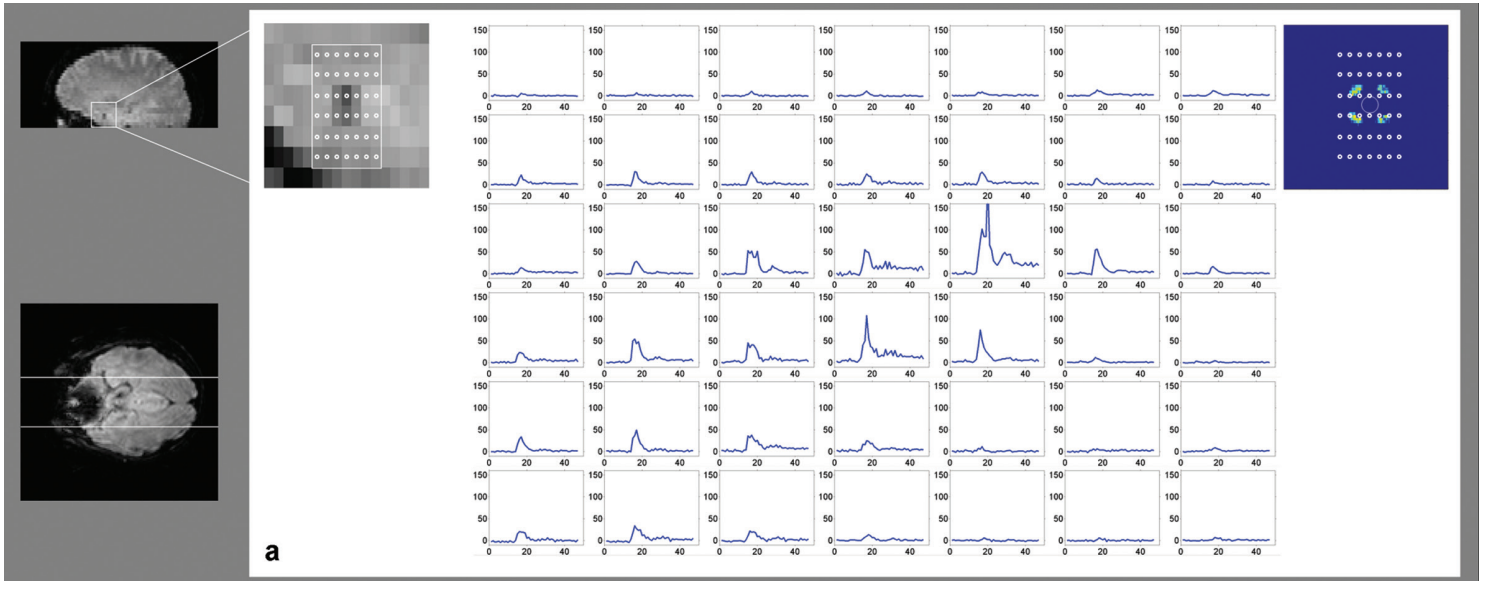
a

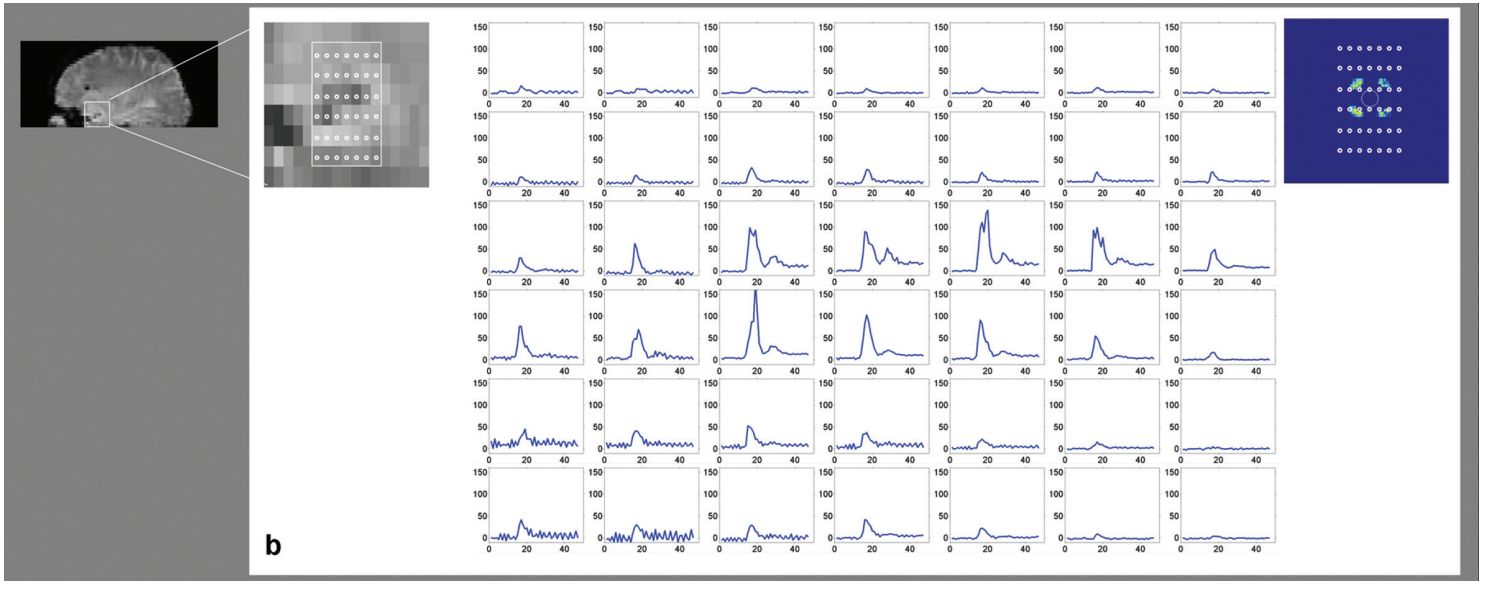

Figure 8: PRESTO DSC-MRI exam of a patient with arteriovenous malformation. Both left and right MCA were selected and the voxels in and around the MCA were used to plot the ΔR_2^* profiles for comparison with the findings of the "in vivo" model (presented right). The small white circles depict the estimated locations of the center of the voxel. The AIF measurements on top of the MCA show large shape errors (double peaks) these can be attributed to partial volume effects.

show that accurate AIF measurement can be made more difficult by the presence of anatomical structures; in this case by a small artery branching from the main MCA segment, which affects the anterior AIF measurement. Figure 8 shows the magnitude-based AIF measurements for the same voxels as in figure 7. The voxels in the center (within the MCA) clearly show partial volume effects corrupting the shape of the AIF profile.

DISCUSSION AND CONCLUSIONS

There are three main findings from this study. The first is that phase-based AIF measurements in tissue near the MCA are superior to those made inside the MCA. Second, the optimal locations for phase-based AIF selection are approximately the same for different fast-imaging sequences. Third, phase-based AIF selection results in more voxels having the correct shape of the AIF compared to magnitude-based AIF selection.

The first aim of this study was to investigate whether phase-based AIF selection in tissue surrounding the MCA is advantageous compared to inside the MCA. AIF selection based on the phase of the MR-signal was proposed more than a decade ago, although it was limited to intravascular AIF measurements (5). In that study, AIF selection was performed in the largest arteries, combined with a high spatial resolution to avoid partial-volume effects. However, in DSC-MRI, voxel sizes are normally larger than the arteries and therefore partial-volume effects will always be present. Since the phase of the tissue and arterial compartment of a partial-volume voxel depends differently on the concentration of contrast agent, the sum of the complex signals may be greater or less than the individual components, thereby leading to changes in the shape of both magnitude-based and phase-based AIF measurements (12, 13). However, for parallel oriented vessels there are no local field changes in tissue and therefore partial volume effects can be corrected (12). Correction for such shape errors is not feasible for arteries, which are not oriented parallel to B_0. The theory and the results from the numerical model in this present study show that no voxel encompassing the MCA passed our shape criteria based on correlation and SNR_{curve} (see figures 1 and 6a). This is in contrast to extravascular phase-based AIF measurements, where several voxels located completely in tissue did pass our shape criteria. Insensitivity to the exact vessel location is observed in figures 1 and 6a, where four large clusters of voxels pass the shape criteria.

The optimal locations for AIF selection are superior, inferior, anterior and posterior from the MCA in voxels located completely outside the MCA. The inferior and anterior locations will sometimes be hindered by the lack of homogeneous tissue. The in vivo example also showed that small branches of the MCA can hinder the AIF measurements (see figures 7 and 8). Figures 1 and 6a show that in voxels located more distant from the vessel center the observed phase changes are very small and noise hinders the accuracy of the AIF measurement. Close to the vessel wall, signal depletion and image distortion can corrupt the AIF measurement. The theory

shows that voxels approximately two vessel diameters from the vessel center have the correct shape. The simulations show that for the specific imaging sequences considered here the AIF measurements should be 2-3 voxels from the vessel center depending on the vessel size. The noise in the phase of the MR-signal depends inversely on the magnitude of the MR-signal, leading to poor SNR in the phase measurements when severe dephasing of the MR-signal occurs. Since the strongest dephasing occurs close to the vessel wall, phase-based AIF measurements should not be performed in this region (see figure 6a). The phase of the MR-signal is also dependent on the echo time. The echo time affects the SNR of the phase-based AIF measurement in two ways. First, longer echo times reduce the magnitude of the baseline MR-signal and therefore reduce the SNR_{curve} of the phase of the MR-signal. Second, longer echo times result in stronger phase effects, thereby increasing the SNR_{curve}. The simulations clearly showed the beneficial effect of stronger induced phase changes, as can be seen in figures 1 and 6a (however, the effect of decreased baseline magnitude on the SNR_{curve} was not taken into account). The effect of echo time on the SNR_{curve} has been studied extensively in a previous study (10).

The most important findings of the numerical model for phase-based AIF selection are also observed in the in vivo example. Intravascular AIF measurements in both the left and right MCAs show very large shape errors (see figures 7 and 8). At the optimal location predicted by the simulation the AIF profiles do indeed have the shapes that most closely represent the "correct" AIF profiles. Unfortunately, the ground truth is unknown and therefore the shape of the AIF measurements could only be assessed qualitatively. The in vivo experiment shows that the best locations for AIF measurements are outside the artery and that the phase changes behave in a similar pattern compared to the simulations: anterior and posterior negative phase changes occur, whereas superior and inferior positive phase changes are found; in between very small phase changes occur (see figure 7).

The second aim of the study was to compare phase-based AIF measurements with magnitude-based AIF selection in tissue surrounding the MCA, and determine whether phase-based AIF selection is advantageous. In the current study, the simulations show that the SNR_{curve} of magnitude-based AIF measurements is lower than the SNR_{curve} of the phase-based AIF measurements (see figure 5). A more extensive study has been performed by Kotys et al., and they found that the SNR per time point can be 4 to 80 times higher depending on contrast agent dose and the time at which data are acquired. Over the entire curve a tenfold increase in SNR_{curve} has been observed at the optimal contrast dose (10).

The second advantage is that more voxels with correct AIF measurement (according to our shape criteria) were found for phase-based compared to magnitude-based AIF measurements. This leads also to less dependence on the exact location of the vessel center within the imaging slice. This can be observed in figures 1 and 6 where the large clusters of voxels with correctly shaped AIF measurements imply that one or two good voxels in these areas can always be found independent of the exact location of the vessel center inside the imaging volume. Since more voxels represent correctly shaped AIF measurements, averaging over several voxels can be

performed to boost the SNR. For both types of EPI scans, this averaging will be best performed in-plane and for PRESTO with its thinner voxels averaging in the slice-select direction should also be possible. Note that averaging phase-based AIF profiles requires changing the sign of the anterior and posterior selected AIF profiles. Voxels selected at a location more distant from the artery are hindered by low SNR_{curve}: however, the simulation showed that the underlying profile remains correct. The more distant locations for magnitude-based AIF measurement are also affected by low SNR_{curve}, but the major cause of the incorrect shape of the AIF is the contamination from the tissue response.

The insensitivity to the tissue response is the third advantage of phase-based AIF measurements over magnitude-based AIF measurements. For magnitude-based AIF measurements contamination with the tissue response can in theory be compensated for using tissue curve subtraction (14), but due to noise in the tissue response the benefit can be limited. In phase-based AIF selection, the tissue response is close to zero because the overall phase effect of randomly oriented vessels is very small and therefore, under the assumption of random vessel orientation, there is almost no contamination of the AIF measurement. The lack of tissue response was also observed in the in vivo example diagonally above the MCA (see figure 7) where voxels show almost no phase changes over time.

Somewhat surprisingly, our results show that the optimal locations for magnitude-based AIF selection and phase-based AIF selection are different. This can be explained by the fact that the large signal drops lead to less precise estimations of the phase. Nonetheless, both phase-based AIF selection and magnitude-based AIF selection are best performed in tissue completely outside the vessel where partial volume effects do not hinder the measurement. A disadvantage for phase-based AIF measurements is that scanner drift can affect the phase images as also observed in the phantom experiments (see figure 4).

One of the reasons why an accurate AIF is important is that deconvolution techniques, such as singular value decomposition (SVD) (3), Fourier deconvolution (4) and maximum likelihood estimation (MLEM) (22), are used to calculate CBV and CBF values from the AIF and the tissue passage curves. Noise in the AIF curves and the fact that deconvolution is an ill-posed problem means that regularization of the deconvolution process is necessary. Partial volume effects lead to non-linear errors in the shape of the AIF measurement, which can result in for example sharp spikes on top of the profile as observed in our previous study (15). Since each deconvolution technique handles noise differently, incorrect AIF profiles will produce different perfusion values depending on the choice of the deconvolution and regularization method. For correct relative values, the deconvolution requires an AIF with the correct shape, which is why we chose to use the shape of the AIF measurement as an important evaluation parameter and did not include deconvolution techniques, which would be too dependent on the exact implementation. The influence of deviations in the shape of the AIF on CBF has been studied previously, and showed that the upslope of the bolus passage curve, in particular, influences the CBF measurement (23).

In conclusion, phase-based AIF selection near the MCA is best performed in tissue superior, inferior, posterior and anterior to the middle cerebral artery. The optimal locations are approximately the same for different fast imaging sequences. Finally, phase-based AIF selection provide more opportunities for AIF selection and has higher SNR_{curve} compared to magnitude-based AIF selection near the MCA.

REFERENCES

1. Emblem KE, Zoellner FG, Tennoe B, Nedregaard B, Nome T, Due-Tonnessen P, Hald JK, Scheie D, Bjornerud A. Predictive modeling in glioma grading from MR perfusion images using support vector machines. Magnetic Resonance in Medicine 2008;60(4):945-952.
2. Christensen S, Mouridsen K, Wu O, Hjort N, Karstoft H, Thomalla G, Rother J, Fiehler J, Kucinski T, Ostergaard L. Comparison of 10 Perfusion MRI Parameters in 97 Sub-6-Hour Stroke Patients Using Voxel-Based Receiver Operating Characteristics Analysis. Stroke 2009.
3. Ostergaard L, Weisskoff RM, Chesler DA, Gyldensted C, Rosen BR. High resolution measurement of cerebral blood flow using intravascular tracer bolus passages .1. Mathematical approach and statistical analysis. Magnetic Resonance in Medicine 1996;36(5):715-725.
4. Rempp KA, Brix G, Wenz F, Becker CR, Guckel F, Lorenz WJ. Quantification of Regional Cerebral Blood-Flow and Volume with Dynamic Susceptibility Contrast-Enhanced Mr-Imaging. Radiology 1994;193(3):637-641.
5. Akbudak E, Conturo TE. Arterial input functions from MR phase imaging. Magnetic Resonance in Medicine 1996;36(6):809-815.
6. Conturo TE, Barker PB, Mathews VP, Monsein LH, Bryan RN. Mr Imaging of Cerebral Perfusion by Phase-Angle Reconstruction of Bolus Paramagnetic-Induced Frequency-Shifts. Magnetic Resonance in Medicine 1992;27(2):375-390.
7. Conturo TE, Akbudak E, Kotys MS, Chen ML, Chun SJ, Hsu RM, Sweeney CC, Markham J. Arterial input functions for dynamic susceptibility contrast MRI: Requirements and signal options. Journal of Magnetic Resonance Imaging 2005;22(6):697-703.
8. Akbudak, E, Hsu, RM, Li, Y, and Conturo, TE. $\Delta R2^*$ or $\Delta\varphi$ contrast agent perfusion effects in blood: quantitation and linearity assessment. In:Proceedings of the ISMRM 6th Annual Meeting, Sydney, 1998, p1197.
9. van Osch MJP, Vonken EJPA, Viergever MA, van der Grond J, Bakker CJG. Measuring the arterial input function with gradient echo sequences. Magnetic Resonance in Medicine 2003;49(6):1067-1076.
10. Kotys MS, Akbudak E, Markham J, Conturo TE. Precision, signal-to-noise ratio, and dose optimization of magnitude and phase arterial input functions in dynamic susceptibility contrast MRI. Journal of Magnetic Resonance Imaging 2007;25(3):598-611.
11. Albert MS, Huang W, Lee JH, Patlak CS, Springer CS. Susceptibility Changes Following Bolus Injections. Magnetic Resonance in Medicine 1993;29(5):700-708.
12. van Osch MJP, van der Grond J, Bakker CJG. Partial volume effects on arterial input functions: shape and amplitude distortions and their correction. Journal of Magnetic Resonance Imaging 2005;22(6):704-709.
13. Kjolby BF, Mikkelsen IK, Pedersen M, Ostergaard L, Kiselev VG. Analysis of Partial Volume Effects on Arterial Input Functions Using Gradient Echo: A Simulation Study. Magnetic Resonance in Medicine 2009;61(6):1300-1309.
14. Thornton RJ, Jones JY, Wang ZYJ. Correcting the effects of background microcirculation in the measurement of arterial input functions using dynamic susceptibility contrast MRI of the brain. Magnetic Resonance Imaging 2006;24(5):619-623.
15. Bleeker EJ, van Buchem MA, van Osch MJ. Optimal location for arterial input function measurements near the middle cerebral artery in first-pass perfusion MRI. J Cereb Blood Flow Metab 2009;29(4):840-852.
16. Haacke EM. MRI: basic principles and application. Wiley; 1999.
17. van Osch MJP, Vonken EJPA, Wu O, Viergever MA, van der Grond J, Bakker CJG. Model of the human vasculature for studying the influence of contrast injection speed on cerebral perfusion MRI. Magnetic Resonance in Medicine 2003;50(3):614-622.
18. Liu GY, Sobering G, Duyn J, Moonen CTW. A Functional Mri Technique Combining Principles of Echo-Shifting with A Train of Observations (Presto). Magnetic Resonance in Medicine 1993;30(6):764-768.

19. Morkenborg J, Taagehoj JF, Vaever PN, Frokiaer J, Djurhuus JC, Stodkilde-Jorgensen H. In vivo measurement of T-1 and T-2 relaxivity in the kidney cortex of the pig - Based on a two-compartment steady-state model. Magnetic Resonance Imaging 1998;16(8):933-942.
20. Kjolby BF, Ostergaard L, Kiselev VG. Theoretical model of intravascular paramagnetic tracers effect on tissue relaxation. Magnetic Resonance in Medicine 2006;56(1):187-197.
21. van Osch MJP, Hendrikse J, Golay X, Bakker CJG, van der Grond J. Non-invasive visualization of collateral blood flow patterns of the circle of Willis by dynamic MR angiography. Medical Image Analysis 2006;10(1):59-70.
22. Vonken EPA, Beekman FJ, Bakker CJG, Viergever MA. Maximum likelihood estimation of cerebral blood flow in dynamic susceptibility contrast MRI. Magnetic Resonance in Medicine 1999;41(2):343-350.
23. Calamante F, Connelly A. DSC-MRI: How accurate does the arterial input function need to be in practice? Pro. Int. Soc. Mag. Reson. Med. 15; 2008.

Chapter 5 A new criterion to aid manual and automatic selection of the arterial input function in dynamic susceptibility contrast MRI

Egbert JW Bleeker, Matthias JP van Osch, Alan Connelly[1,2], Mark A van Buchem, Andrew G Webb, Fernando Calamante[1,2]

1) Brain Research Institute, Florey Neuroscience Institutes (Austin), Melbourne, Australia
2) Department of Medicine, University of Melbourne, Melbourne, Australia

ABSTRACT

Dynamic susceptibility contrast MRI requires an arterial input function (AIF) to obtain cerebral blood flow, cerebral blood volume (CBV) and mean transit time. The current AIF selection criteria discriminate venous, capillary and arterial profiles based on shape- and timing-characteristics of the first passage. Unfortunately, partial volume effects (PVEs) can lead to shape errors in the bolus passage, including a narrower and higher peak, which might be selected as a "correct" AIF. In this study, a new criterion is proposed that detects shape errors based on tracer kinetic principles for computing CBV. This criterion employs the ratio of the steady-state value to the area-under-the-curve of the first passage, which should result in an equal value for tissue and arterial responses. By employing a reference value from tissue, PVEs-induced shape errors of the AIF measurement can be detected. Different factors affecting the ratio were investigated using simulations. These showed that the new criterion should only be used in studies with T_1-insensitive acquisition. In vivo data were used to evaluate the proposed approach. The data showed that the new criterion enables detection of shape errors, although false positives do occur, which could be easily avoided when combined with current AIF selection criteria.

Published in Magnetic Resonance in Medicine (2011) Feb; 65(2):448-456

INTRODUCTION

Dynamic susceptibility contrast (DSC)-MRI is a valuable clinical tool to aid in the diagnosis and staging of many brain diseases (1). DSC-MRI provides a set of hemodynamic parameters such as cerebral blood flow (CBF), cerebral blood volume (CBV) and mean transit time (MTT) (2, 3). These three parameters can be obtained after deconvolution of the tissue response (the passage of contrast agent through the capillaries in tissue) with the arterial input function (AIF, the passage of contrast agent through a brain-feeding artery).

The AIF is often selected manually by a trained expert, but a number of automatic AIF selection procedures have been proposed (4-9). The major advantages of automatic selection are operator independence and speeding up of the analysis resulting in fast, standardized and reproducible results. Fast analysis is especially important for clinical decision-making in acute stroke as evidenced by the frequently used slogan "time is brain" (10). Automatic selection is often performed using criteria such as early time-to-peak, steep rise, low first moment, high peak-height and small full-width-half-maximum (FWHM) (4-7, 9) or a metric using a set of these criteria combined with a gamma-variate fit through the first passage (8). With these criteria, venous, capillary and arterial profiles can be discriminated.

Unfortunately, AIF measurements are susceptible to partial volume effects (PVEs) due to the relatively low spatial resolution of the acquisitions, and these PVEs alter the shape of the AIF measurement (11-13). Ideally, automatic procedures would only select AIF profiles unaffected by PVEs. However, some specific shape errors, such as a narrower peak with a higher peak-height than the true shape (13), fulfill the currently used AIF selection criteria and could therefore easily be selected as a "correct" AIF measurement. Therefore, we propose an additional criterion for automatic AIF selection, which could also be useful for guiding manual AIF selection. This criterion relies on the fact that, theoretically, perfusion parameters cannot only be measured from the first passage but also from the second passage. This would however, require that the signal-versus-concentration relation is linear and this condition fails for AIFs that exhibit shape changes due to PVEs (12, 13). Shape errors could therefore be detected by comparing perfusion parameters obtained from the first and second passage. The second passage is, however, difficult to determine due to the overlap with the first and subsequent passage. The theory, described in this manuscript, shows that the first passage in combination with the steady-state (or post-bolus equilibrium) can be used in a similar manner to detect shape errors in the AIF. Therefore, we propose to use the ratio of the mean steady-state value to the area-under-the-curve (AUC) of the first passage of contrast agent as a metric to detect PVEs in AIF measurements. This metric is compared to a reference value obtained from tissue in the same DSC-MRI data, since linearity of the signal versus concentration contrast agent has been proven for brain tissue (14).

The purpose of this study is to describe a new AIF selection criterion based on tracer kinetic theory that can detect AIF measurements corrupted by PVEs. AIF selection guided by the new

proposed criterion was studied by means of numerical simulations and evaluated using six in vivo exams. Both the reference ratio value of tissue and the ratio value of AIF measurements (with and without PVEs) were investigated.

METHODS

Partial volume effects

The presence of contrast agent in an artery will lead, except for arteries at the magic angle (54.7°) or parallel to the main magnetic field B_0, to a homogenous magnetic field change inside the artery and a lobular shaped pattern of magnetic field changes outside the artery (15). For a partial volume voxel, this implies that the total complex MRI signal from that voxel is made up of several components that show different phase changes for a particular contrast agent concentration. The amplitude of the total signal will therefore depend on how much the different components are in-phase or out-of-phase. For different concentrations of contrast agent, the same voxel may show different gradations of in- or out-of-phase contributions, thereby leading to non-linear shape changes of the estimated contrast concentration profile. Different manifestations of PVEs were simulated using the Maxwell equations corrected for the sphere of Lorenz by shifting of a voxel partly encompassing a cylinder oriented perpendicular to the main magnetic field (described in more detail in the Methods section Simulations). Subsequently,

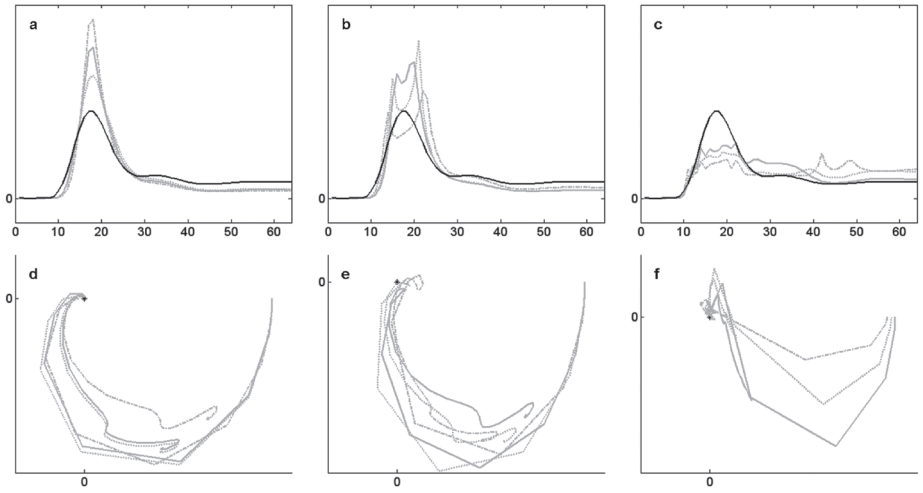

Figure 1: Different manifestations of partial volume effects manually grouped into three groups. A group with narrower and higher peaks in the first passage than the true shape (**a**), a group with two peaks in the first passage in close succession (**b**) and a third group with almost no first passage peak (**c**). The black line is the ground truth and all profiles are rescaled to have equal area-under-the-curve. The corresponding complex trajectory of the ΔR_2^* profiles in (**a**, **b** and **c**) are respectively (**d**, **e** and **f**).

the curves were manually grouped according to common shape features as presented in figure 1. Figure 1a, 1b and 1c show the ΔR_2^* profiles together with the ground truth, these profiles were scaled according to their area-under-the-curve. Figure 1d, 1e and 1f show the corresponding complex trajectories of the ΔR_2^* profiles in 1a, 1b and 1c respectively. The first group (Figure 1a), consists of curves showing a narrower and higher peak than the true shape. The high and narrow peak in ΔR_2^* is formed when, at the maximum concentration, all components add destructively (see Figure 1d). This leads to an underestimation of the amplitude of the MR signal, resulting in a severe overestimation of ΔR_2^* (12, 13). The second group of curves (Figure 1b) show, instead of a single peak in the first passage, two peaks in close succession. This occurs when the complex signal passes close to the zero for a concentration lower than the maximum concentration (see Figure 1e). The third group (Figure 1c) shows curves with almost no peak in the first passage and a high post-bolus equilibrium. Automatic AIF selection criteria are likely to exclude AIF measurements suffering from partial volume errors of the second and third group, but AIF measurements with PVEs such as those in the first group are not excluded, because these curves have a small width, early time-to-peak and high peak-height.

The proposed criterion

The aim of the proposed criterion is to identifying voxels with minimal shape distortions due to PVEs. The proposed metric is the ratio of the mean steady-state value to the area-under-the-curve (AUC) of the first passage of contrast agent, further referred to as "SS:AUC^{1st} ratio". This metric follows from tracer kinetic principles to calculate CBV. The CBV can be calculated, using the area-under-the-curve of the different passages or the steady-state concentration (16), by taking the ratio of the tissue response to the AIF:

$$CBV = \frac{\int_{1st\ passage} C(t)dt}{\int_{1st\ passage} C_{AIF}(t)dt} = \frac{\int_{2nd\ passage} C(t)dt}{\int_{2nd\ passage} C_{AIF}(t)dt} = \frac{C(t_{ss})}{C_{AIF}(t_{ss})} \quad [1]$$

where C(t) is the concentration contrast agent in tissue, $C_{AIF}(t)$ is the concentration contrast agent in the brain-feeding artery, t_{ss} is the time at which the concentration of contrast agent is in steady-state (17, 18). Rewriting equation 1 results in three ratios that are constant for arterial and tissue concentration-versus-time profiles of a single experiment:

$$\frac{\int_{2nd\ passage} C(t)dt}{\int_{1st\ passage} C(t)dt} = \frac{\int_{2nd\ passage} C_{AIF}(t)dt}{\int_{1st\ passage} C_{AIF}(t)dt} = \text{constant} \quad [2]$$

$$\frac{C(t_{ss})}{\int_{1st\ passage} C(t)dt} = \frac{C_{AIF}(t_{ss})}{\int_{1st\ passage} C_{AIF}(t)dt} = \text{constant} \quad [3]$$

$$\frac{C(t_{ss})}{\int_{2nd\ passage} C(t)dt} = \frac{C_{AIF}(t_{ss})}{\int_{2nd\ passage} C_{AIF}(t)dt} = \text{constant} \quad [4]$$

These relations are only valid when C(t) reflects the true concentration-time curve, although a general scaling factor would not affect the validity of these relations. In DSC-MRI the MR-signal changes are converted to ΔR_2^*. The ΔR_2^* profiles of the AIF measurements in or close to a brain-feeding artery are often hampered by PVEs. These PVEs lead to scaling errors and more importantly to shape errors with respect to the true concentration-versus-time profile. When such shape errors are present the SS:AUC^{1st} ratio of the AIF measurement deviates from the ground truth SS:AUC^{1st} ratio. The reference value reflecting the ground truth SS:AUC^{1st} ratio can be determined in tissue, because the ΔR_2^* profile in tissue is linear with respect to the concentration of contrast agent under the assumption that the arterioles and capillaries are randomly oriented (14).

Two of the three metrics were not investigated because of practical considerations: (i) the second passage has lower signal-to-noise than the first passage (where SNR is defined as the signal difference between pre-bolus and peak concentration over the noise at baseline), and (ii) the gamma-variate fit through the second passage is more difficult to determine than the steady-state due to its overlap with the first and subsequent bolus passages (see Figure 2).

In this study, the mean steady-state level was determined by averaging the last ten dynamics of the perfusion scan. The AUC of the first passage was determined using a gamma-variate fit through the first passage (see Figure 2). Good starting values are important for preventing the fit to end up in a local minimum. The starting values for the simulations were obtained from

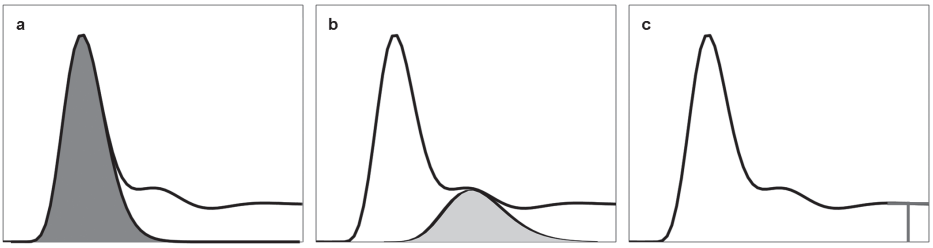

Figure 2: The gamma-variate estimation of the first (**a**) and second passage (**b**) and the steady-state estimation (**c**). The gamma-variate fit through the first passage is feasible but the gamma-variate fit through the second passage only contains a few data points due to the overlap with the first and subsequent tissue passage. Two of these three measurements can be used to determine the ratio, which assesses the shape error in the AIF due to PVEs.

the gamma-variate fitting values through the simulated tissue curve (to reflect closer the in vivo situation, see below); the tissue curve was calculated from the first passage of the ground truth AIF convolved with an exponential residue function.

Simulations

All simulations were implemented in MATLAB (R2007b, Natick, MA, USA). In the simulations, a modeled AIF (19) and a modeled tissue response were used. The tissue contrast agent concentration was created after convolving the modeled AIF with an exponential residue function (CBF = 60 ml/100g/min, MTT = 4 sec, CBV = 4 ml/100g).

Partial volume effects simulations

The numerical model to study partial volume shape errors in the AIF measurements included local magnetic field changes and relaxation rate changes due to the passing contrast agent. For these simulations, only the contrast agent passage within the artery is modeled. The artery is assumed to be a cylinder (diameter = 4 mm) oriented perpendicular to B_0 and the artery is surrounded by tissue. The longitudinal, transverse relaxation times and the relaxivity values were set to in vivo values at 1.5 T (which are used for all other simulations): T_1 is 0.95 sec and 1.4 sec for tissue and blood respectively (20), T_2^* is 0.1 sec for tissue and blood (20), transverse relaxivity of the contrast agent in arterial blood with a linear term 7.62 l/mmol/sec and a quadratic term 0.57 l^2/$mmol^2$/sec (21). The local field changes, resulting from the susceptibility difference (molar susceptibility $\chi_m = 0.3209 \cdot 10^{-3}$ l/mol (21)), were calculated using the Maxwell equations corrected for the sphere of Lorenz on a spatial grid of 250 µm. The double-dose experiment at 1.5 T is also representative for a single-dose experiment at 3 T (11). A rectangle voxel with a size of 1x3 times the radius of the cylinder was used (due to symmetry in the direction of the vessel, only two dimensions need to be included). This voxel was shifted over the local field map and the gradient-echo signal was calculated taking in account the relaxivity effects of the contrast agent within the artery. The shifting generates a large range of PVEs that can occur when there is a linear phase effect inside the artery and a blooming effect outside the artery. The simulated AIF profiles were studied and three groups were manually selected (see Figure 1).

Factors affecting the SS:AUC^{1st} ratio

The effects of T_1 relaxation changes on SS:AUC^{1st} ratio of the tissue response for a gradient-echo MR-signal were studied using the modeled tissue response. The effect of T_1 relaxation changes on the arterial response is expected to be minimal due to fresh inflow of spins and were not further studied. The flip angle and repetition time were varied in the simulations, since these two parameters influence the T_1-effect in tissue the most (22). Gradient echo signals with TE/TR 31/1500 msec and TE/TR 31/600 msec were simulated and the flip angle was varied from 5° to 90° in steps of 5° using a longitudinal relaxivity (r_1) of 4.3 l/mmol/sec (23).

The second factor that can affect the SS:AUC^{1st} ratio is the SNR, since the ratio measured in the AIF and the reference ratio obtained from the tissue response are subject to noise. The effect of noise on the SS:AUC^{1st} ratio was studied using the modeled tissue response. Four different SNR levels were simulated (20:1, 30:1, 40:1 and 50:1) with 10000 random noise repeats. From these simulations the mean value and the standard deviation of the SS:AUC^{1st} ratio were calculated.

It has been shown that AIF measurements are best selected in locations where PVEs do not corrupt the measurements (11, 12). These locations are, for example, in homogenous tissue close to but completely outside the middle cerebral artery (MCA) (11). Unfortunately, AIF measurements performed in tissue are hampered by the tissue response. Therefore, the third factor studied is the contamination of the AIF measurement by the tissue response. The influence of the tissue response on the extravascular susceptibility induced contrast was studied using a previously published numerical model (11). This model, which was validated using phantom experiments, simulates AIF measurements in and near a cylinder that is oriented perpendicular to B_0 (a model for arteries such as the MCA). The model is based on the numerical model used to study PVEs (see above), but is extended and includes also imaging effects such as the phase-shifts and distortions from the EPI readout train as well as a tissue passage of the contrast agent in the surrounding. The imaging settings for the simulations were the following: segmented EPI, matrix size 96x96, TE/TR 31/600 msec, flip angle (FA) 40°, field of view (FOV) 220x220 mm^2, 10 slices of 6.2 mm thickness with 1 mm gap, number of echoes per echo-train 21. The SS:AUC^{1st} ratios of the simulated AIF measurements were calculated, the difference with the ground truth in percent was determined and the AUC of the first passage was used as a measure for SNR.

In vivo

In vivo DSC-MRI exams of six patients (1 man, 5 women; mean age 36, range 16-46) suffering from Systemic Lupus Erythematosus were used for evaluation of both the reference SS:AUC^{1st} ratio obtained from the tissue response and measured AIF SS:AUC^{1st} ratio in and around the MCA. In vivo experiments were performed at 3 T (Achieva, Philips, Best, The Netherlands) using an 8-channel receive array head coil, 0.1 mmol/kg-bodyweight Gd-DTPA was injected at 5 ml/sec followed by a saline chaser of 25 ml injected at the same speed. The imaging sequence had the following settings: dual-echo segmented EPI: data matrix 96x96, TE_1/TE_2/TR 11/31/600 msec, FA 40°, FOV 220x220 mm^2, SENSE factor of 2.2, 10 slices of 6.2 mm thickness with 1 mm interslice gap with one additional slice through the carotid artery just above the bifurcation, number of echoes per echo-train 21. The study was approved by the local ethics committee.

In vivo post processing

The in vivo DSC-MRI exams were acquired with two echo times. By using a dual-echo sequence, correction for T_1-relaxation effects (caused by the passage of contrast agent) is possible (24, 25):

$$\Delta R_2^*(t) = \frac{1}{TE_2 - TE_1}\left(\ln\left(\frac{S_{TE_1}(t)}{S_{TE_2}(t)}\right) - \ln\left(\frac{S_{TE_1}(0)}{S_{TE_2}(0)}\right)\right) \quad [5]$$

where TE is the echo time and S(t) is the magnitude of the MR-signal.

To segment gray matter, white matter and vessels, a relative CBV was calculated using the AUC of the ΔR_2^*-curves. The CBV value intervals for the segmentation were empirically determined and the resulting gray and white matter segmentation was compared to the pre-bolus T_2^* image. Furthermore, a lobular mask was used to segment the tissue in the following lobes and areas: the frontal, parietal, occipital and temporal lobe, the cerebellum, the insula and a combined area of thalamus, caudate nucleus and putamen (26). Before segmentation, the dataset was normalized using an EPI template in SPM 5 (Wellcome Trust Centre for Neuroimaging, Institute of Neurology, UCL, London UK – http://www.fil.ion.ucl.ac.uk/spm). The average tissue response was determined for the gray matter and white matter part of the different lobe-areas. The SS:AUC^{1st} ratio was determined and a two-sided paired t-test was used to compare the SS:AUC^{1st} ratio obtained from gray matter and white matter. The mean value and the standard deviation of the SS:AUC^{1st} ratios for the different gray matter and white matter areas of the lobular mask were calculated. The acceptance range for the SS:AUC^{1st} ratio was defined as the mean value plus or minus two times the standard deviation (referred to as "range of acceptance"). The in vivo DSC-MRI exams were also used to evaluate AIF measurements near the MCA, and to illustrate whether PVEs can be detected in vivo.

RESULTS

Simulations: The influence of T_1-effects, noise and the tissue passage curve on the proposed criterion

Figure 3 shows the influence of T_1-effects on the SS:AUC^{1st} ratio of the tissue response. The T_1-effects for relatively short repetition times (as used in segmented EPI) are large for normal flip angles. Flip angles close to the Ernst angle result in a post-bolus equilibrium around zero and therefore the SS:AUC^{1st} ratio is close to zero. For flip angles around 5° the T_1-effect is reduced and the SS:AUC^{1st} ratio is close to the ground truth, but with such small flip angles the SNR of the acquisition is reduced. Single shot EPI with its longer repetition time is less sensitive to T_1-effects, as shown in figure 3c and d. Nevertheless, flip angles around the Ernst angle reduce the SS:AUC^{1st} to around 50% of the ground truth. These results show that the error in the SS:AUC^{1st} ratio due to T_1-effects is large for techniques that are T_1-sensitive. The dual-echo approach can make the acquisition T_1-insensitive and for this reason, T_1-effects were ignored in further simulations.

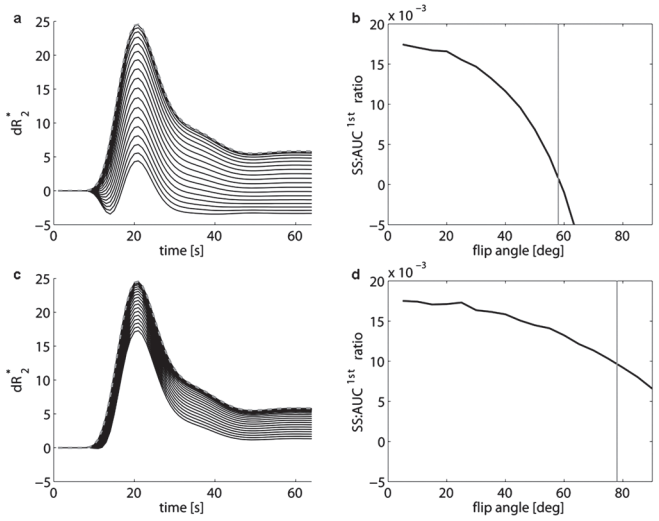

Figure 3: The influence of T_1-effects. Top: segmented EPI (TE/TR 31/600 msec), bottom: single shot EPI (TE/TR 31/1500 msec). The various curves in (**a**) and (**c**) correspond to the different flip angles simulated (bottom curve = 90º; upper curve = 5º); the gray dashed line corresponds to the curve in the absence of T_1-effects. Left: the profiles of ΔR_2^*, right: the SS:AUC^{1st} ratio versus the flip angle (the ground truth for this case is 0.0176). The vertical gray line in (**b**) and (**d**) correspond to the Ernst angle.

The influence of noise on determining the SS:AUC^{1st} ratio was studied using repeated simulations with random noise. The SNR was varied from 20:1 to 50:1 in steps of 10:1, and the results are presented in table 1 (the ground truth of the SS:AUC^{1st} ratio for this simulated case was 0.0176). The standard deviation of the SS:AUC^{1st} estimation reduces with increasing SNR. However, a single voxel AIF measurement with a typical SNR of 50:1 still has a 95% confidence interval of the mean value ± 7.6%.

The third factor influencing the SS:AUC^{1st} ratio is the contamination of the AIF with the tissue response. Figure 4a shows the SS:AUC^{1st} ratio for the simulated AIF measurements in and around the MCA (presented as a sagittal section); the ground truth is 0.0176. The % deviation from the ground truth better shows the accuracy of the SS:AUC^{1st} ratio (see Figure 4b). Figure 4b shows that the SS:AUC^{1st} ratio is higher than the ground truth in voxels encompassing the MCA. Furthermore, it can be seen that the tissue remote from the vessel in the superior-inferior

Table 1: The mean SS:AUC1st ratio, the standard deviation (SD) and the standard deviation as percent of the mean value for the modeled AIF with different SNR levels and 10000 random noise repeats. Ground truth for this case: 0.0176

SNR	Mean	SD	SD [%]
20:1	0.0175	0.0015	8.8
30:1	0.0176	0.0011	6.1
40:1	0.0176	0.0008	4.7
50:1	0.0176	0.0007	3.8

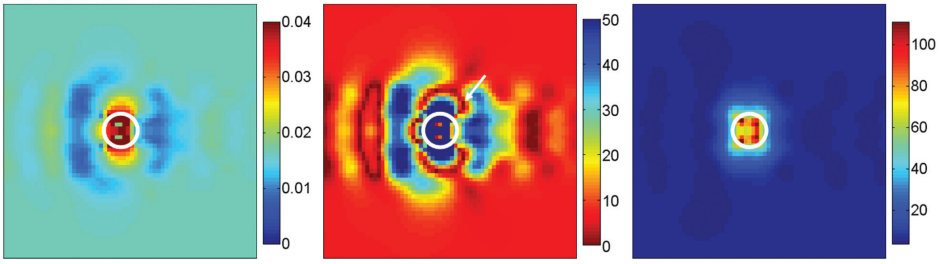

Figure 4: The three figures show **a**) the SS:AUC^{1st} ratio (ground truth is 0.0176) for simulated AIF measurements in and near a perpendicular oriented cylinder (model for the middle cerebral artery), **b**) the percentage difference from the ground truth value for the simulated AIF measurements and **c**) the AUC of the first passage. Note that the superior and inferior tissue response has a ratio value close to the ground truth and that a rim (indicated with a white arrow) around the perpendicular cylinder (indicated with a white circle) provides the same SS:AUC^{1st} ratio.

direction has a SS:AUC^{1st} ratio close to the ground truth. However, in this region, the AUC of the first passage is low (see figure 4c). More importantly, Figure 4b shows that AIF measurements in the vicinity of the MCA also have a correct SS:AUC^{1st} ratio, but only in a narrow rim because further anterior and posterior the SS:AUC^{1st} ratio reduces to a value lower than the ground truth. The AUC of the first passage indicates regions with high SNR and low SNR; high SNR is found in voxels encompassing the MCA and low SNR is found in tissue.

In vivo: Evaluation of the proposed criterion

The reference SS:AUC^{1st} ratio was determined for different lobes and areas in the segmented gray and white matter, since averaging over a large number of voxel increases the SNR substantially and hence improves the accuracy. Unfortunately, for small regions (such as the insula) averaging over a number of voxels did not provide particularly high SNR, SNR values were as low as 26:1 for gray matter and 16:1 for white matter. However, the average SNR over all regions and patients is high with an average SNR value of 169:1 for gray matter and 126:1 for white matter. The average SS:AUC^{1st} ratio and the standard deviation over the different lobes and areas are presented in table 2.

Table 2: The mean SS:AUC^{1st} ratio for gray matter (GM) and white matter (WM), the standard deviation (SD) and the standard deviation in percent of the mean value for 6 patients based on the gray matter and white matter segmentation and averaged over the different brain lobes.

	Mean GM	SD	SD [%]	Mean WM	SD	SD [%]
patient 1	0.0236	0.0022	9.3%	0.0211	0.0038	17.8%
patient 2	0.0208	0.0014	7.0%	0.0194	0.0019	9.8%
patient 3	0.0262	0.0025	9.6%	0.0234	0.0016	7.0%
patient 4	0.0363	0.0036	10.0%	0.0319	0.0018	5.5%
patient 5	0.0261	0.0023	8.9%	0.0240	0.0018	7.6%
patient 6	0.0349	0.0034	9.7%	0.0317	0.0023	7.4%

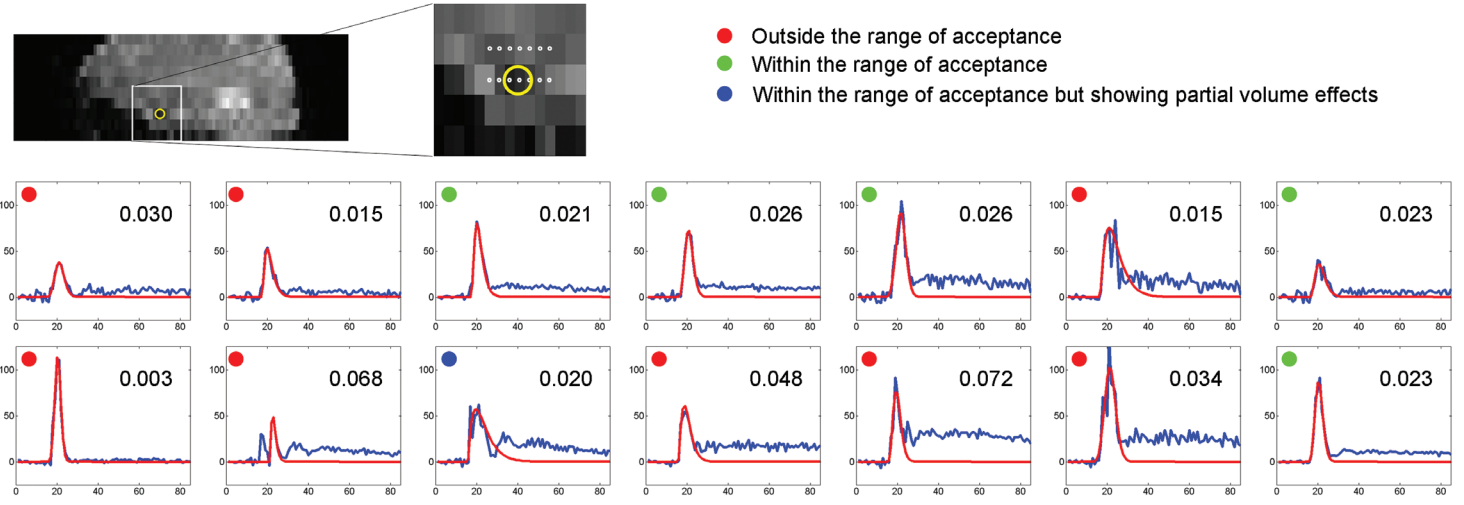

Figure 5: AIF measurements in and around the MCA of an in vivo example (patient 1). The profiles within the MCA, as well as the profile touching the artery, show partial volume effects. The profile anterior to the MCA shows a high and narrow peak resulting in a low SS:AUC^{1st} ratio. The metric can also provide AIF measurements with minimal PVEs, these are located outside the MCA which is in agreement with the simulations.

The mean SS:AUC^{1st} ratio of the tissue response varies over subjects; the SS:AUC^{1st} ratio for patients 4 and 6, for example, are much higher for both gray matter and white matter than the other patients. This could be due to a different fraction of blood flowing to the brain vasculature. The mean SS:AUC^{1st} ratio of the gray matter is significantly higher than the white matter SS:AUC^{1st} ratio ($p<0.005$) for each patient. The standard deviation (in percent of the mean value) for gray matter as calculated from different lobes is not larger than 10%; using this value the range of acceptance is formed with an interval of the mean value ± 20%. This range of acceptance was used to evaluate the SS:AUC^{1st} ratio of AIF measurements in and around the MCA. The profiles of one patient are presented in figure 5; the range of acceptance for this patient (patient 1) is [0.019 0.028]. The individual profiles of the AIF measurements partly encompassing the MCA have SS:AUC^{1st} ratios that fall outside the range of acceptance (see red dots in Figure 5) except for one profile. That profile has a first passage that is distorted and the gamma-variate model is not the right model to fit this first passage. The first passage of the second plot on the bottom row in figure 5 also has a different shape than the gamma-variate function, but here the result is that the SS:AUC^{1st} ratio falls outside the range of acceptance. It is therefore important to test whether the gamma-variate fit is the right model to fit the first passage. A profile with a very high peak and a small width is observed in the bottom row first plot; it should be noted that the sharp peak of this profile is similar to the first group of the simulated PVEs. Therefore, this profile may not necessarily be recognized as distorted by previously proposed automatic AIF selection algorithms; however, the SS:AUC^{1st} ratio falls outside the range of acceptance since the mean steady-state value is close to zero and the AUC of the first passage is high. A number of voxels with SS:AUC^{1st} ratios that fall inside the range of acceptance (see green dots in Figure 5) are superior to the vessel and posterior to the vessel, which is in agreement with predictions from a previous study (11).

DISCUSSION AND CONCLUSIONS

The most important findings of this study are four-fold. First, a new criterion based on tracer kinetic theory can detect non-linear shape errors due to PVEs in the estimated evolution of the AIF (measured using the ΔR_2^*) using a reference value obtained from tissue. Second, for correct use of the ratio approach, T_1-insensitive techniques should be employed for the DSC-MRI acquisition, because T_1-effects predominantly affect the steady-state of the tissue response, leading to different SS:AUC^{1st} ratios for AIF versus tissue. Third, we suggest that the best reference SS:AUC^{1st} ratio is obtained from the gray matter tissue. Finally, the proposed criterion should be used as an additional criterion in automatic AIF selection procedures and not as a stand-alone criterion.

In this study, a new criterion is proposed to aid in the AIF selection to exclude shape errors arising from PVEs. The criterion uses a metric that is based on tracer kinetic principles. The

metric is the ratio of the mean steady-state (determined using a number of time-points of the post-bolus equilibrium) to the AUC of the first passage (determined using a gamma-variate fit through the time-points of the first passage). The SS:AUC^{1st} ratio for the AIF measurement is guided by the reference SS:AUC^{1st} ratio obtained from tissue. The gray matter voxels, which are used for the reference SS:AUC^{1st} ratio, can for example be selected by a simple gray matter segmentation based on the relative CBV determined using the AUC of the tissue response. We determined a range of acceptance for the SS:AUC^{1st} ratio based on in vivo data. The in vivo example in figure 5 confirms that AIF measurements with severe PVEs fall outside the range of acceptance (the mean value ± 20%). In particular, it was found that PVEs voxels with high and narrow peaks do occur in vivo (see figure 5, bottom row left; compare figure 1(a)); such peaks would be selected as good examples of AIF voxels using most automated approaches, but they can be identified and excluded using the proposed additional criterion.

There are, however, a number of factors that influence the SS:AUC^{1st} ratio either of the AIF, the tissue reference value or both. T_1 relaxation effects affect the shape of the tissue response and, especially, the steady-state signal, which in turn affect the SS:AUC^{1st} ratio. In general, T_1-effects lead to an underestimation of the reference SS:AUC^{1st} ratio. The simulations showed that for segmented EPI, with its relatively short repetition time, the T_1-related error in SS:AUC^{1st} ratio is large. Using a very small flip angle can reduce T_1-effects (22), but this also reduces the baseline SNR. Acquiring segmented EPI with two echo times makes correction for T_1-effects possible, and is therefore advantageous over normal segmented EPI acquisition. Single shot EPI does also suffer from T_1-effects although in a lesser extent. When there is fresh inflow of spins, such as in arteries, these T_1-effects can be ignored. Finally, it could be studied whether the influence of T_1-effects on the SS:AUC^{1st} ratio of tissue could be corrected for e.g. by assuming a certain average steady-state concentration.

We suggest that the reference SS:AUC^{1st} ratio is best obtained from gray matter in areas distant from arteries and veins. In vivo, differences in reference SS:AUC^{1st} ratio were observed between the gray and white matter, which is not in line with the findings of Kjølby et al. (14), who predicted, based on simulations and analytical models, a linear relation between ΔR_2^* and concentration of contrast agent for both white and gray matter. Although the reason is not fully understood, this difference could be because the area of dephased signal from a particular vessel touches the dephasing area of other vessels for the higher concentrations of contrast agent in gray matter. The overlapping dephasing areas would induce a leveling off of the ΔR_2^* versus gadolinium concentration curve, thereby indeed leading to a higher SS:AUC^{1st} ratio for gray matter than white matter as was observed. The theoretical model of Kjølby et al. assumes that each vessel can be treated as a separate object, not influencing or influenced by other vessels and this leveling-off effect is therefore not included. An alternative reason could be that the static dephasing regime is not valid for low concentrations that occur in the steady-state of white matter (27, 28), or the fact that the mesoscopic structure of the gray matter is different from that of the white matter, or the fact that diffusion is more anisotropic in white matter (29).

Contamination of white matter voxels in the gray matter average would lower the reference ratio value. This effect is however expected to be small due to the small difference between the white and gray matter values.

Since the SS:AUC^{1st} is determined over a region of interest with many voxels, the SNR is increased compared to a single voxel. However, the SNR for a small ROIs (e.g. the insula) in the lobular mask had low SNR values resulting in reduced accuracy of that specific SS:AUC^{1st} ratio. The simulations show that for these low SNR values (approximately 20:1) the 95% confidence interval is the true value ± 18%. However, the average SNR over all ROIs and all patients is high for gray and white matter. In addition, the frontal and temporal areas show for all patients a higher SS:AUC^{1st} ratio than the occipital and parietal areas (data not shown). These regional differences together with the inaccuracy due to low SNR of a few regions lead to the approximately 10% standard deviation in the ratio estimation of gray matter. It can be expected that averaging the total gray matter would further reduce this source of error.

The new proposed selection criterion is not designed as a stand-alone criterion, but as an additional selection criterion for automatic AIF selection or for guiding manual AIF selection. Errors can occur when the gamma-variate fit no longer describes the first passage accurately. Estimation of the SS:AUC^{1st} ratios for the AIF measurement shows false positives for some partial volume errors. However, these false positives could be easily avoided by including boundary constraints on the gamma-variate fit through the first passage, or by using an additional standard criterion, such as a small FWHM. Alternatively, more specialized methods for first passage extraction can also be used to improve the ratio estimation (27, 30, 31).

Errors in the SS:AUC^{1st} ratio can also occur when there are motion artifacts. In the post-bolus equilibrium, motion artifacts can lead to a sudden increase, sudden decrease or sharp transient peaks (data not shown). When incorporating the proposed criterion in an automatic AIF selection program, these motion artifacts should be detected. In addition, the post-bolus equilibrium should have a sufficient number of time-points, therefore the acquisition of the DSC-MRI exam should be long enough to properly characterize the tail of the bolus passage. Moreover, since the SS:AUC^{1st} ratio is highly dependent on the AUC$^{1st\ passage}$, having proper starting values for the gamma-variate fit is of high importance. We used as starting values for the simulation the fitting values of the fit through the ground truth, and as starting values for the in vivo ratio estimates the fitting values of the whole brain average, which is primarily weighted to the tissue response. Both approaches led to appropriate fitting of the first passage.

Since the new criterion aims at detecting PVEs, AIF measurements that are only hampered by noise will not be excluded. Noise originating from physiological pulsations or instrumental noise can alter the AIF profile to produce a wider peak and a smaller peak-height. Including these AIF measurements is crucial for unbiased averaging. Less stringent criteria concerning the first passage can aid in unbiased averaging of several "correct" AIF measurements.

Although the simulations are only performed for an artery perpendicular to B_0, the generic pattern of a linear phase effect inside and a blooming phase effect outside the artery is typical

for all angles except arteries at the magic angle or parallel to B_0. The shifting of the voxel in steps smaller than the voxel size generated a large range of PVEs. We expect that the shape errors encountered in the simulations are representative for shape errors of arteries with other orientations.

In conclusion, we propose a metric that can aid in either manual or automatic AIF selection. The metric checks whether the AIF is corrupted by PVEs. Having an AIF that is not corrupted by PVEs greatly improves the quantification of the hemodynamic parameters. Since the proposed approach is a post-processing method, the ratio can also be used retrospectively in previously acquired data with sufficient sampling of the post-bolus equilibrium.

REFERENCES

1. Rowley HA, Roberts TP. Clinical perspectives in perfusion: neuroradiologic applications. Top Magn Reson Imaging 2004;15(1):28-40.
2. Ostergaard L, Weisskoff RM, Chesler DA, Gyldensted C, Rosen BR. High resolution measurement of cerebral blood flow using intravascular tracer bolus passages .1. Mathematical approach and statistical analysis. Magnetic Resonance in Medicine 1996;36(5):715-725.
3. Rempp KA, Brix G, Wenz F, Becker CR, Guckel F, Lorenz WJ. Quantification of Regional Cerebral Blood-Flow and Volume with Dynamic Susceptibility Contrast-Enhanced Mr-Imaging. Radiology 1994;193(3):637-641.
4. Murase K, Kikuchi K, Miki H, Shimizu T, Ikezoe J. Determination of arterial input function using fuzzy clustering for quantification of cerebral blood flow with dynamic susceptibility contrast-enhanced MR imaging. Journal of Magnetic Resonance Imaging 2001;13(5):797-806.
5. Mlynash M, Eyngorn I, Bammer R, Moseley M, Tong DC. Automated method for generating the arterial input function on perfusion-weighted MR imaging: Validation in patients with stroke. American Journal of Neuroradiology 2005;26(6):1479-1486.
6. Bjornerud A, Emblem KE. A fully automated method for quantitative cerebral hemodynamic analysis using DSC-MRI. J Cereb Blood Flow Metab 2010;30(5):1066-78.
7. Carroll TJ, Rowley HA, Haughton VM. Automatic calculation of the arterial input function for cerebral perfusion imaging with MR imaging. Radiology 2003;227(2):593-600.
8. Kim J, Leira EC, Callison RC, Ludwig B, Moritani T, Magnotta VA, Madsen MT. Toward fully automated processing of dynamic susceptibility contrast perfusion MRI for acute ischemic cerebral stroke. Comput Methods Programs Biomed 2010;98(2):204-13.
9. Mouridsen K, Christensen S, Gydensted L, Ostergaard L. Automatic selection of arterial input function using cluster analysis. Magnetic Resonance in Medicine 2006;55(3):524-531.
10. Saver JL. Time is brain - Quantified. Stroke 2006;37(1):263-266.
11. Bleeker EJ, van Buchem MA, van Osch MJ. Optimal location for arterial input function measurements near the middle cerebral artery in first-pass perfusion MRI. J Cereb Blood Flow Metab 2009;29(4):840-852.
12. Kjolby BF, Mikkelsen IK, Pedersen M, Ostergaard L, Kiselev VG. Analysis of Partial Volume Effects on Arterial Input Functions Using Gradient Echo: A Simulation Study. Magnetic Resonance in Medicine 2009;61(6):1300-1309.
13. van Osch MJP, van der Grond J, Bakker CJG. Partial volume effects on arterial input functions: shape and amplitude distortions and their correction. Journal of Magnetic Resonance Imaging 2005;22(6):704-709.
14. Kjolby BF, Ostergaard L, Kiselev VG. Theoretical model of intravascular paramagnetic tracers effect on tissue relaxation. Magnetic Resonance in Medicine 2006;56(1):187-197.
15. Haacke EM. MRI: basic principles and application. Wiley; 1999.
16. Speck O, Chang L, Itti L, Itti E, Ernst T. Comparison of static and dynamic MRI techniques for the measurement of regional cerebral blood volume. Magnetic Resonance in Medicine 1999;41(6):1264-1268.
17. Perkio J, Aronen HJ, Kangasmaki A, Liu YW, Karonen J, Savolainen S, Ostergaard L. Evaluation of four postprocessing methods for determination of cerebral blood volume and mean transit time by dynamic susceptibility contrast imaging. Magnetic Resonance in Medicine 2002;47(5):973-981.
18. Sakaie KE, Shin W, Curtin KR, McCarthy RM, Cashen TA, Carroll TJ. Method for improving the accuracy of quantitative cerebral perfusion imaging. Journal of Magnetic Resonance Imaging 2005;21(5):512-519.
19. van Osch MJP, Vonken EJPA, Wu O, Viergever MA, van der Grond J, Bakker CJG. Model of the human vasculature for studying the influence of contrast injection speed on cerebral perfusion MRI. Magnetic Resonance in Medicine 2003;50(3):614-622.

20. Pedersen M, Klarhofer M, Christensen S, Ouallet JC, Ostergaard L, Dousset V, Moonen C. Quantitative cerebral perfusion using the PRESTO acquisition scheme. Journal of Magnetic Resonance Imaging 2004;20(6):930-940.
21. van Osch MJP, Vonken EJPA, Viergever MA, van der Grond J, Bakker CJG. Measuring the arterial input function with gradient echo sequences. Magnetic Resonance in Medicine 2003;49(6):1067-1076.
22. Calamante F, Vonken EJPA, van Osch MJP. Contrast agent concentration measurements affecting quantification of bolus-tracking perfusion MRI. Magnetic Resonance in Medicine 2007;58(3):544-553.
23. Morkenborg J, Taagehoj JF, Vaever PN, Frokiaer J, Djurhuus JC, Stodkilde-Jorgensen H. In vivo measurement of T-1 and T-2 relaxivity in the kidney cortex of the pig - Based on a two-compartment steady-state model. Magnetic Resonance Imaging 1998;16(8):933-942.
24. Perman WH, Gado MH, Larson KB, Perlmutter JS. Simultaneous Mr Acquisition of Arterial and Brain Signal Time Curves. Magnetic Resonance in Medicine 1992;28(1):74-83.
25. Vonken EJPA, van Osch MJP, Bakker CJG, Viergever MA. Measurement of cerebral perfusion with dual-echo multi-slice quantitative dynamic susceptibility contrast MRI. Jmri-Journal of Magnetic Resonance Imaging 1999;10(2):109-117.
26. Admiraal Behloul F, Olofsen H, van den Heuvel DM, Schmitz N, Reiber JH, van Buchem MA. Fully automatic lobe delineation for regional white matter lesion load quantification in a large scale study. Pro. Int. Soc. Mag. Reson. Med. 11; 2003.
27. Gall P, Mader I, Kiselev VG. Extraction of the first bolus passage in dynamic susceptibility contrast perfusion measurements. Magnetic Resonance Materials in Physics Biology and Medicine 2009;22(4):241-249.
28. Kiselev VG. On the theoretical basis of perfusion measurements by dynamic susceptibility contrast MRI. Magnetic Resonance in Medicine 2001;46(6):1113-1122.
29. Kiselev VG. Transverse relaxation effect of MRI contrast agents: A crucial issue for quantitative measurements of cerebral perfusion. Journal of Magnetic Resonance Imaging 2005;22(6):693-696.
30. Smith M, Salluzzi M, Frayne R. A novel approach to remove the effect of recirculation in arterial input functions. Pro. Int. Soc. Mag. Reson. Med. 15; 2007. 1447.
31. Wu Y, An HY, Krim H, Lin WL. An independent component analysis approach for minimizing effects of recirculation in dynamic susceptibility contrast magnetic resonance imaging. Journal of Cerebral Blood Flow and Metabolism 2007;27(3):632-645.

Chapter 6: Evaluation of signal formation in local arterial input function measurements of dynamic susceptibility contrast MRI

Egbert JW Bleeker, Andrew G Webb, Marianne AA van Walderveen, Mark A van Buchem, and Matthias JP van Osch

ABSTRACT

Correct arterial input function (AIF) measurements in dynamic susceptibility contrast-MRI are crucial for quantification of the hemodynamic parameters. Often a single global AIF is selected near a large brain-feeding artery. Alternatively, local AIF measurements aim for voxel-specific AIFs from smaller arteries. Because local AIFs are measured higher in the arterial-tree, it is assumed that these will reflect the true input of the microvasculature much better. However, do the measured local AIFs reflect the true concentration-time curves (CTC) of small arteries? To answer this question, a 3D numerical model that simulated partial-volume effects (PVEs) in local AIF measurements was created and the simulated local AIFs were compared to the ground truth. In addition, in vivo data were used to evaluate local AIF candidates selected using two angiograms. The findings are two-fold. First, the simulations show that PVEs in the local AIF measurements lead to broader CTCs than the ground truth AIF due to extravascular susceptibility effects and the contrast agent passing through surrounding microvasculature. Second, the in vivo data showed that the shape-characteristics of local AIFs are similar to the shape-characteristics of gray matter CTCs. These findings suggest that local AIF measurements do not reflect the true CTC in small arteries.

Under revision

INTRODUCTION

Dynamic susceptibility contrast (DSC-) MRI measures brain-perfusion by monitoring the passage of a bolus of contrast agent through the brain-vasculature. Voxel-based measurements of the bolus passage in tissue give information about local cerebral blood flow (CBF), cerebral blood volume (CBV) and subsequently the mean transit time (MTT) (1, 2). These local perfusion estimates are useful, for example, for staging tumors and assessing the tissue at risk of permanent damage after a stroke (3, 4). However, the tissue response needs to be calibrated via deconvolution with an arterial input function (AIF) i.e., the passage of contrast agent through a brain-feeding artery. Most DSC-MRI studies use a single (often manually selected) global AIF for all voxels.

Alternatively, it has been suggested that local or regional AIF measurements can improve determination of the perfusion parameters (5-7). These local AIFs are measured closer to the capillaries of the brain tissue compared to global AIF measurements. Deconvolution with a local AIF produces residue functions that are less affected by delay and dispersion effects due to the transport of the contrast agent from the location of the AIF determination to the beginning of the capillary bed (8). The former can be corrected for by using delay-insensitive deconvolution techniques, but dispersion corrupts the perfusion estimates (2, 9, 10). In addition, local AIF measurements are flow territory specific, which can be especially beneficial when there is a stenosed or occluded large artery, since such large vessel pathologies lead to additional delay and dispersion in the corresponding flow territory (11). The use of a global AIF measured contralaterally from the stenosis or occlusion would create perfusion estimates for the flow territory of the stenosed artery that include the dispersive properties of the stenosis, leading to underestimation of CBF (12).

However, such local AIF measurements are performed with voxels larger than the small brain-feeding arteries from which the AIF is obtained. The MR-signal from such a voxel will be influenced by the contrast agent within the artery, the magnetic field changes outside the artery induced by the intravascular contrast agent and by the contrast agent passing through the microvasculature of the tissue surrounding the artery (tissue response). The combination of the relaxation effects and local field changes can lead to shape changes in the AIF due to differences in phase evolution of the different compartments. For larger arteries, such non-linear partial-volume effects (PVEs) have been shown to lead to erroneous perfusion estimates (13-15).

Validation of local AIF measurements is ideally performed by comparing the measured local AIF with the true concentration-time curve (CTC) within the small brain-feeding artery. However, blood sampling cannot be performed at that point in the brain-vasculature. Therefore, previous validations of local AIF measurements have been performed by comparing the perfusion maps (and sometimes the CTCs) from local AIF measurements to those obtained from manually selected global AIF measurements (5-7, 16, 17). A single report showed additional

comparison to PET perfusion maps (16). When validating local AIF methods one should keep in mind that all methods to automatically select (local) AIFs are based on features of a "proper" AIF, such as small width, early time-of-arrival (TA), high peak-height, etc, and the selected curves will therefore always exhibit exactly these properties (6, 7, 18-21). The important question in validation is: do the curves of the local AIF measurements really reflect the true CTC of small arteries? A previous simulation study by Kjølby and coworkers reported that the contribution of the tissue response to an AIF measured in or near a large artery can lead to broadening of the measured bolus passage inside the artery, although the simulations only modeled two orientations (parallel and perpendicular to the main magnetic field) and in vivo verification was absent (14).

In this study, the properties of the bolus passage curves in voxels located on top of small arteries are compared to curves obtained in the gray matter. The properties of these two collections of voxels should differ, with a much higher percentage of AIF-like curves in the first group required to justify a local AIF approach. In addition to the in vivo study, numerical simulations of partial-volume effects in local AIF measurement were used to investigate the influence of the tissue passage and extravascular magnetic field changes on the shape of local AIFs.

METHODS

Simulations

A small brain-feeding artery was modeled as a cylinder at different orientations to the main magnetic field and different locations within the voxel. Intra- and extravascular MR-signal was modeled using Maxwell equations and normal gradient echo signal formation formulas, including relaxation changes and dephasing due to the local field changes. Local AIF measurements were modeled for single shot EPI and PRESTO (an ultra fast T_2^*-weighted 3D acquisition with echo shifting (22)) sequences. Single shot EPI with voxels of 2x2x6 mm^3 was simulated on a high-resolution 3D grid, with 250 µm interspacing, spanning 12x12 mm^2 by 24 mm. The imaging settings, TE/TR 25/1500 msec and FA= 75°, were set to resemble typical in vivo settings. The PRESTO simulations consisted of voxels of 2.5x2.5x3.5 mm^3 on a high-resolution 3D grid, with 250 µm interspacing, spanning 15x15 mm^2 by 14 mm. The imaging settings, TE/TR 30/20 msec and FA= 8°, were set the same as the in vivo settings employed in this study. Distortions due to the long echo train were ignored in the simulations due to computational limitations (13, 23). In order to generate a larger range of partial-volume effects in the simulations all voxels were shifted over the 3D grid in steps of 250 µm in all three directions. The numerical model was implemented in MATLAB (R2007b, Natick, MA, USA).

The orientation of the cylinder with spherical angles θ (angle between the vessel axis and the direction of the main magnetic field) and φ varied for θ from 0° to 90° in steps of 15°, and

for φ from 0° to 45° in steps of 15°. The vessel size was set to have a radius of 0.5 mm, 1.0 mm and 1.5 mm.

Inside the cylinder the arterial CTC is simulated with a modeled AIF (24), outside the cylinder the tissue response is simulated by the same modeled AIF but convolved with an exponential residue function (CBF= 60 ml/100 g/min, MTT= 4 sec, CBV= 4 ml/100 g).

The relaxation times were set to resemble blood and tissue at 3 Tesla (T_1 blood 1.7 sec (25), T_2 blood 70 msec, T_1 tissue 1.1 sec (26), T_2 tissue 70 msec). A quadratic relation taken from 1.5 Tesla experiments and rescaled to 3 Tesla was used for the relation between the intravascular ΔR_2^* and the concentration of gadolinium (linear term 15.24 l/mmol/sec, quadratic term 2.28 $l^2/mmol^2/sec$ (27)). The relaxivity in tissue was set to 87 l/mmol/sec (28), longitudinal relaxivity was ignored. The local field changes, resulting from the susceptibility difference (molar susceptibility of the contrast agent $\chi_m = 0.3209 \cdot 10^{-3}$ l/mol (27)), were calculated using the Maxwell equations corrected for the sphere of Lorenz.

To study the effect of the tissue response inside the voxel on local AIF measurements, simulations were performed with and without the tissue response in the surroundings of the small artery. In addition, the effect of crushing the intravascular signal in PRESTO due to the large gradients employed for echo shifting was investigated by setting the intravascular signal to zero.

Simulation post processing

The simulated signals were transformed to ΔR_2^*. Profiles were excluded from further analysis when a reference point on top of the axis of the simulated artery was not located within the simulated voxel, because otherwise the signal changes induced by the arterial passage are too minimal. The middle of the volume was chosen as the abovementioned reference point. The different orientations, radii and shifts for PVEs, all experienced some degree of partial-volume effects, and were treated as one group. Profiles with severe partial-volume shape errors were excluded using the steady state to the area-under-the-curve (AUC) of the first passage ratio ($SS:AUC^{1st}$) criterion (29). This $SS:AUC^{1st}$ criterion used the modeled tissue response as a reference and a gamma variate fit was used to determine the AUC of the first passage. Additional exclusion of profiles was based on the time-to-peak (exclusion of too high TTPs, defined as ground truth AIF TTP value +2*standard deviation (SD) over all TTPs of the simulated profiles). The profiles were compared to the ground truth using the Pearson correlation coefficient.

For evaluation of the shape-characteristics of the simulated local AIFs three metrics were used. Two metrics (TA and relative TTP (rTTP=TTP-TA)) were determined using the gamma variate fit and one metric (full-width-at-half-maximum (FWHM)) was determined using the ΔR_2^* profile. The histograms were evaluated and the mean values of the metrics were compared to the metrics of the ground truth.

In vivo experiments

In vivo DSC-MRI exams (five in total) of three patients suffering from arteriovenous malformation were employed in this study. One patient was scanned three times; the other two were scanned a single time. In vivo experiments were performed at 3 Tesla (Achieva, Philips, Best, The Netherlands) using an 8-channel receive array head coil, 0.1 mmol/kg-bodyweight Gd-DTPA was injected at 5 ml/sec followed by a saline chaser of 25 ml injected at the same speed. The imaging sequences had the following settings: PRESTO, data matrix 96x87, zerofilled to 128x101, 30 slices 3.5 mm thick with no interslice gap, FOV 240x190 mm^2, 75 dynamic scans, scan duration 120 sec, TE/TR 30/20 msec, FA 8°, EPI factor 15, SENSE factor 2.2, phase encoding was set from right to left; time-of-flight (TOF), data matrix 512x325, zerofilled to 512x488, 220 slices 0.6 mm thick, FOV 180x172 mm^2, TE/TR 3.5/23 msec, FA 15°; T1TFE, data matrix 192x192, zerofilled to 256x256, 130 slices 1.2 mm thick, FOV 220x175 mm^2, TE/TR 4.6/10 msec, FA 8°. The study was approved by the local ethics committee.

In vivo post processing

In vivo data were all post processed using SPM5 (Wellcome Trust Centre for Neuroimaging, Institute of Neurology, UCL, London UK – http://www.fil.ion.ucl.ac.uk/spm) and MATLAB. The entire hemisphere affected by the AVM was excluded. Local AIF candidates were determined using two different angiograms: one based on the TOF angiogram and another based on the pre- and post-contrast T_1-weighted images. A small artery TOF mask was created by thresholding the TOF to such a level that the cortex and skull were excluded. In addition, a separate large artery TOF mask was created using an empirical threshold approximately twice the threshold for the small artery mask. Both small artery mask and large artery mask were coregistered to the first T_2^*-weighted DSC-MRI image and the large arteries were subsequently removed from the small artery mask.

The small artery T_1-based mask was constructed by subtracting the pre-contrast T_1-weighted image from the coregistered post-contrast T_1-weighted image. The T_1-based mask was coregistered to the first T_2^*-weighted DSC-MRI image using the T_1 pre-contrast image.

In addition, a gray matter mask was created as a reference dataset to compare the CTCs of the small artery masks to. This gray matter mask was created using empirically thresholded rCBV values that were formed using the area under the ΔR_2^* profile. Skull stripping was performed on both small artery masks and the gray matter mask based on an image of the maximum difference of the contrast agent passage that was smoothed and subsequently eroded.

From all ΔR_2^* profiles selected by the small artery masks and the gray matter mask severe partial-volume shape errors were excluded using the SS:AUC^{1st} ratio criterion (29). Additional exclusions of profiles were based on the TTP (larger than the mean value +2*SD), TA (larger than the mean value +2*SD) and relative (r)CBV (smaller than lower-threshold of the gray matter mask). To evaluate the shape-characteristics of the local AIF candidates and the gray matter profiles the same three metrics (TA, rTTP, FWHM) as used in the evaluation of the simulation

data were calculated. First, the metric-histograms of the small arteries masks and gray matter mask were compared. In addition, the average for each metric was computed. The metrics of the local AIF candidates were compared to the metrics of the gray matter profiles and to each other using a paired t-test over the five DSC-MRI scans using $\alpha = 0.05$ corrected for multiple comparison using Bonferroni correction (3 variables) leading to $p_{bonf} < 0.0167$ (one-sided) and $p_{bonf} < 0.0083$ (two-sided).

RESULTS

The results of the shape-characteristics of the local AIFs in the numerical simulations are presented in Table 1 and Figures 1-4. Figure 1 shows the histograms of the different metrics for the simulated PRESTO data with tissue passage and crushing. The three metrics have approximately a Gaussian distribution. Figure 2 shows the mean value and SD of the three timing metrics TA, rTTP, FWHM for the ground truth AIF, the simulated tissue passage, and the different simulations of EPI and PRESTO. As shown in Table 1 and Figure 2, the TA of all simulations are closer to the TA of the ground truth AIF than the TA of the ground truth tissue response. Furthermore, including the tissue response (wT) in the simulations did not significantly delay TA for the two investigated sequences. The addition of the tissue response in the local AIF voxel does, however, increase the rTTP for both sequences. Whereas, the rTTP of the simulations without the tissue response in the surrounding are similar to the rTTP of the ground truth AIF, the rTTP of the simulations with tissue response is delayed and even close to the rTTP of the ground truth of the tissue response. The FWHM of the simulations is larger than the FWHM of the ground truth AIF and close to the FWHM of the ground truth of the tissue response, except for PRESTO without the tissue response (woT). The addition of the tissue response has a small effect on the FWHM for single shot EPI and a relatively large effect for PRESTO. In PRESTO without the tissue response, the intravascular signal is crushed and therefore only the susceptibility effects in the

Table 1: Shape-characteristic metrics used for evaluating the simulations of single shot EPI and PRESTO. Simulations were performed with the tissue response (wT) and without the tissue response (woT). In addition, the PRESTO simulations were performed with crushing (woT, wT) and without crushing of the intravascular signal due to the large gradients employed for echo shifting (wT woC). The ground truths (GT) of the AIF and the tissue response are presented as well. The timing metrics are in seconds and SD is the standard deviation over the group of local AIFs.

	GT		EPI				PRESTO					
	AIF	tissue	woT		wT		woT		wT		wT woC	
			mean	SD	mean	SD	mean	SD	mean	SD	mean	SD
TA	9,5	11,1	9,8	0,2	9,8	0,2	9,9	0,3	9,9	0,3	9,9	0,3
rTTP	8,1	9,7	7,6	0,3	8,9	0,5	7,5	0,4	8,5	0,6	8,7	0,6
FWHM	9,8	12,5	12,7	1,8	13,3	1,6	11,2	1,8	12,5	1,7	12,8	1,8

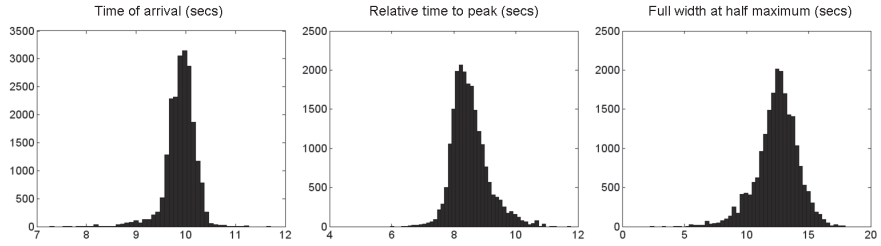

Figure 1: The histograms of the time-of-arrival (TA), relative time-to-peak (rTTP) and full-width-at-half-maximum (FWHM) of the simulated local AIFs. All distributions are close to Gaussian distributions.

surrounding of the small artery can explain the increase in FWHM. The effect of crushing the intravascular signal in PRESTO on the TA and rTTP compared to PRESTO without crushing (wT woC) is minimal.

Subdividing the group of local AIF profiles (of PRESTO (wT)) by artery size shows that smaller arteries have a larger rTTP compared to the rTTP of the larger arteries, although the effect is small (see Figure 3). Note that the ground truth AIF of these simulations were the same for small and large arteries, that is the diameter of the simulated arteries was the only difference. The small arteries also have a broader profile compared to the larger arteries (see Figure 3). Figure 4 shows the histograms of the correlation of the ΔR_2^* profiles with the ground truth for the different simulations. This figure shows that the distribution of the correlation with the ground truth is shifted to higher correlation values for the simulations without the tissue passage. The correlation of the ground truth tissue response with the ground truth AIF is 0.81.

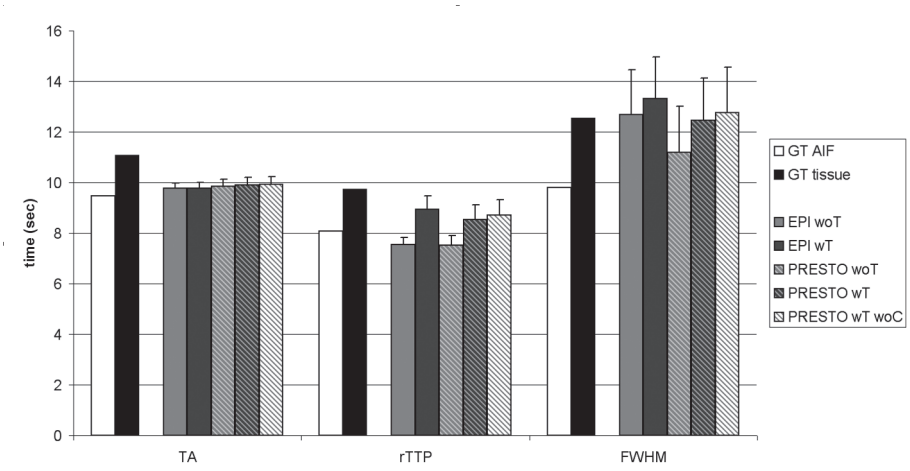

Figure 2: Three timing characteristics (time-of-arrival (TA), relative time-to-peak (rTTP) and full-width-at-half-maximum (FWHM)) in seconds to compare the simulated local arterial input functions (AIFs) (of single shot EPI and PRESTO) with the ground truth AIF (white bar) and ground truth tissue response (black bar). Without tissue response (woT), with tissue response (wT) and without crushing (woC).

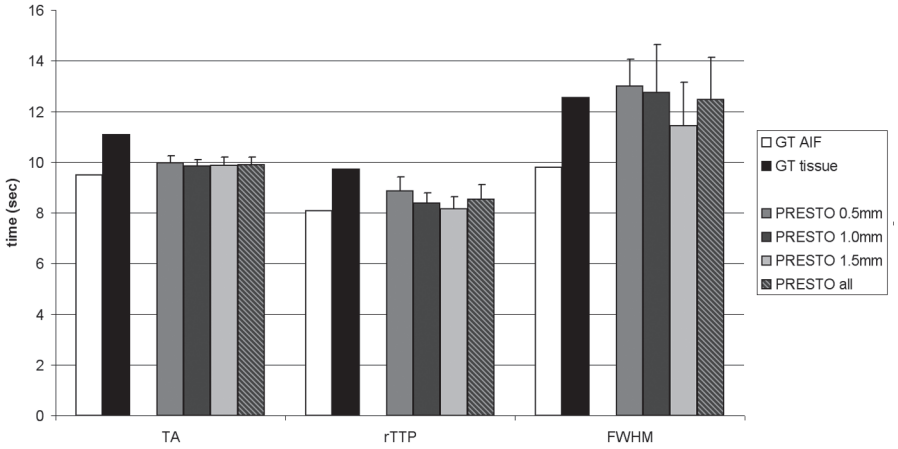

Figure 3: Division of the simulated local arterial input functions (AIFs) of PRESTO by artery radius with tissue response and crushing (wT). Shown are the ground truth AIF (white bar), the ground truth tissue response (black bar), the three radii and the group average for each timing characteristics (time-of-arrival (TA), relative time-to-peak (rTTP) and full-width-at-half-maximum (FWHM)).

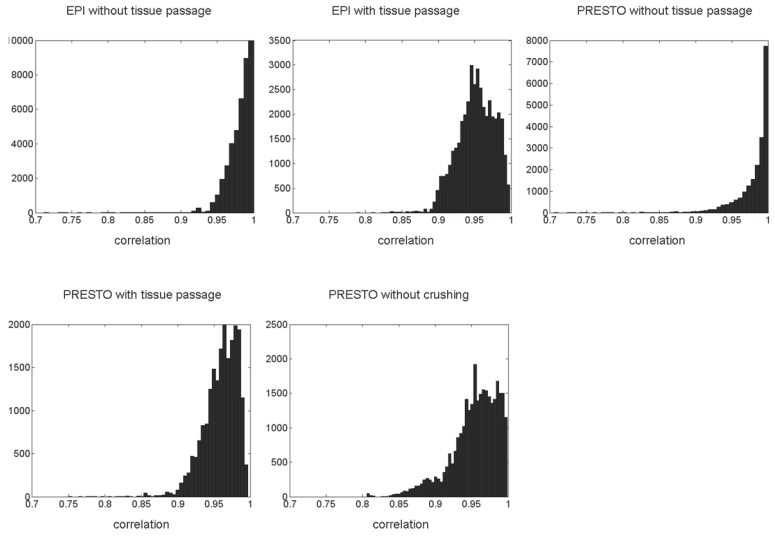

Figure 4: Histograms of the correlation with the ground truth arterial input function (AIF) for the different simulations. The correlation of the ground truth tissue response with the ground truth AIF is 0.81.

Table 2 and Figure 5 show the in vivo metrics of gray matter (GM) and the local AIF candidates based on the two angiograms. GM has the latest TA but the value is very close to the TA of the T_1-based local AIF candidates. The TA of the TOF-based local AIF candidates are significantly lower than GM and significantly lower than the T_1-based local AIF candidates. The average rTTP of the TOF-based local AIF candidates is larger than the rTTP of gray matter although not

Table 2: Shape-characteristic metrics used for evaluating the in vivo local AIF candidates based on two angiograms (TOF and T_1). The metric values are compared to gray matter (GM), since the ground truth is unknown.

	GM		TOF		T1		GM vs TOF		GM vs T1		T1 vs TOF	
	mean	SD	mean	SD	mean	SD	diff	p-value	diff	p-value	diff	p-value
TA	25,4	1,0	24,8	1,0	25,3	1,0	-0,6	0,0075	-0,1	0,5529	-0,5	0,0008
rTTP	4,9	0,2	5,2	0,4	5,4	0,4	0,3	0,0343	0,5	0,0050	-0,2	0,0028
FWHM	6,3	0,6	6,3	0,5	6,8	0,7	0,0	0,8605	0,5	0,0039	-0,5	0,0109

significantly, whereas the average rTTP of the T_1-based local AIF candidates is significantly larger than the average rTTP of gray matter. The TOF-based local AIF candidates have ΔR_2^* profiles as broad as GM, as measured with the average FWHM. The T_1-based local AIF candidates have a significantly larger FWHM than the average FWHM of GM. The distributions of the in vivo metrics are shown in Figure 6; all show a distribution close to a Gaussian distribution. Furthermore, there is much overlap between the distributions of the shape-characteristics of GM and the local AIF candidates. Moreover, the distribution in the lower tails for the three timing metrics differ little in absolute numbers between GM and the local AIF candidates.

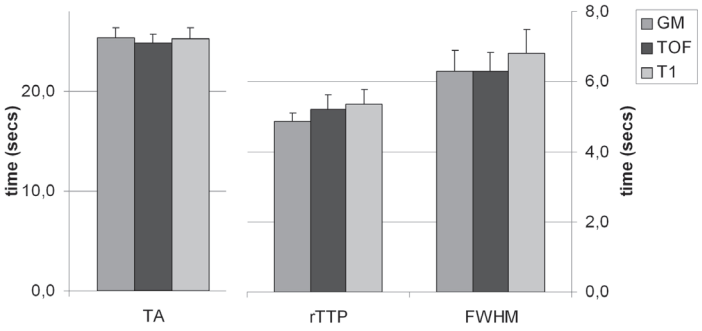

Figure 5: Shown are three timing characteristics (time-of-arrival (TA), relative time-to-peak (rTTP) and full-width-at-half-maximum (FWHM)) of the in vivo local arterial input function candidates (TOF-based and T_1-based) together with gray matter (GM) metric values.

DISCUSSION AND CONCLUSIONS

The aim of this study was to investigate whether automatic local AIF measurements would reflect the true concentration-time curve of small brain-feeding arteries, since partial-volume effects in the local AIF measurement can lead to broadening of the measured ΔR_2^* profile (14). For this purpose, a 3D numerical model was created that simulates local AIF measurements with single shot EPI and PRESTO acquisition at different orientations and with different artery sizes. In addition, in vivo data were used to identify true local AIF candidates using two different

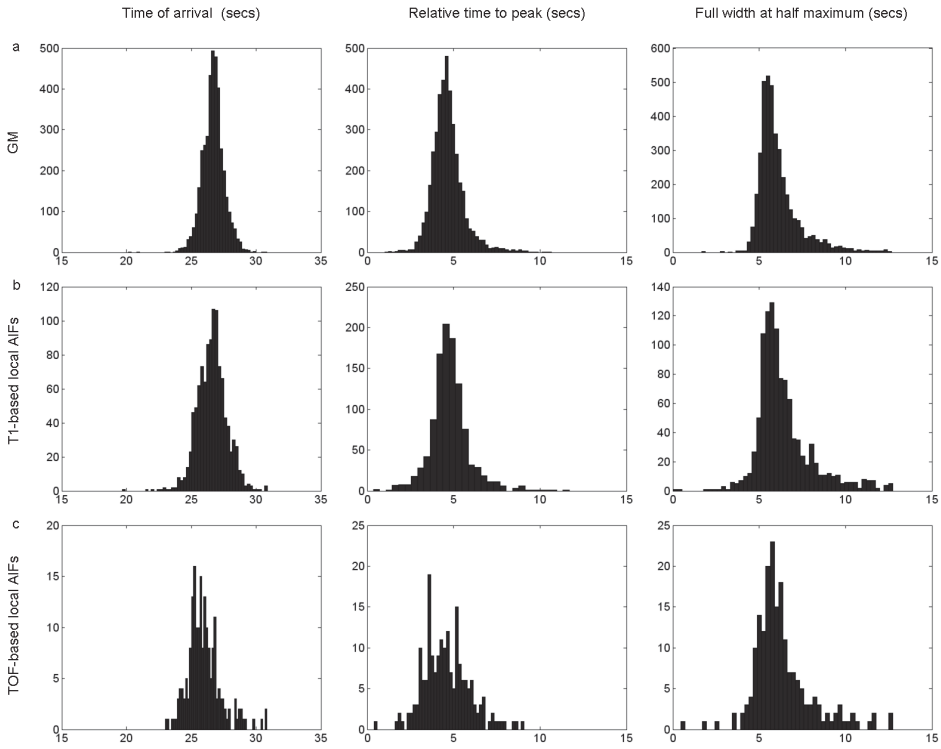

Figure 6: Histograms of the shape-characteristic metrics for gray matter (a) for T_1-based local arterial input function (AIF) candidates (b) and TOF-based local AIF candidates (c). The distributions are close to Gaussian distributions and the lower tail of the timing metrics shows a large degree of overlap. Note that the number of voxels in the gray matter (GM) mask is much larger than the two small artery masks.

angiograms and the shape-characteristics from these candidates were compared to gray matter CTC shape-characteristics. The findings of this study are two-fold. First, the simulations show that partial-volume effects in local AIF measurements lead to erroneously broader measured AIFs. The broadening is both caused by the tissue response and the extravascular local field changes. Second, in vivo data shows (based on shape-characteristics of the measured ΔR_2^* profiles) that local AIF selection do not have a higher number of AIF-like profiles than GM profiles. Therefore, local AIF measurements using shape-criteria cannot reliably measure the CTC in small arteries, since the overlap in the distributions of GM and local AIF candidates is too high.

The simulations show that partial-volume effects lead to broader local AIF profiles. For single shot EPI the FWHM was even larger than the FWHM of the ground truth of the tissue response. For single shot EPI, the broadening is caused by extravascular susceptibility effects and intravascular relaxation changes, because the simulations with and without tissue response show little difference in FWHM. For PRESTO, separation between extravascular susceptibility effects and intravascular relaxation changes was made by simulating the sequence with and

without crushing of the intravascular signal. These simulations showed that the influence of the intravascular signal on the broadening of the simulated local AIF is small. The simulations of PRESTO (with crushing) with and without tissue response show that the tissue response causes, on average, broadening of the simulated local AIFs as do the extravascular susceptibility effects. The fraction between the effect of tissue response and extravascular susceptibility effects on the broadening is likely to change for different orientations, but on average, both effects lead to comparable broadening. The TA of the simulated local AIFs are close to the TA of the ground truth AIF. The rTTP is sensitive to the tissue response and for the simulation without the tissue response, the rTTP is close to the rTTP of the ground truth AIF. For the simulations with the tissue response, the rTTP is close to the rTTP of the ground truth of the tissue response. Subdividing the simulated local AIF profiles by vessel radius showed that smaller arteries result in more erroneous broadening of the local AIF measurement compared to the larger arteries. The largest studied arteries with a radius of 1.5 mm, however, result in local AIF measurements still broader than the ground truth AIF. The simulations show that these smaller arteries show later TA (note that the ground truth AIF is the same) and longer FWHM.

The in vivo data were used to investigate local AIF candidates based on angiogram information and, because the ground truth is unknown, the shape-characteristics of the local AIF candidates are compared to gray matter CTCs. For this purpose, two different angiograms were used (TOF angiogram and T_1 pre- and post-contrast angiogram). The properties of angiogram-based local AIF candidates should differ from the properties of the GM profiles, with a much higher number of AIF-like curves in the first group to justify a local AIF approach. The results show that the TA is significantly lower for the TOF-based local AIFs compared to GM and compared to T_1-based local AIFs (one sided t-test was used since larger TA were not expected). This suggests that the TOF-based local AIF candidates are likely to be more upstream than the local AIF candidates determined with the T_1 pre- and post-contrast images. The local AIF candidates of the TOF angiogram have an average FWHM equal to the FWHM value of GM. The T_1-based local AIF candidates have a significantly larger FWHM than the FWHM of GM. Note that these findings confirm the observation of the simulations where FWHM were observed equal or larger than the ground truth of the tissue response FWHM value. The distributions of the shape metrics angiogram local AIF candidates and GM overlap. One should take in account that the number of voxels in the GM mask is much larger than the small artery masks. Therefore, the absolute number of voxels in the lower tail of the shape-characteristics plays a role in determining whether the chance of selecting a local AIF candidate is higher for the angiogram-based local AIFs compared to GM profiles. Since there is a large overlap, differentiation between GM profiles and local AIF candidates will be difficult. This is supported by the simulations that show that the rTTP and FWHM of the simulated local AIF (with tissue response) are close to the rTTP and FWHM of the ground truth of the tissue response.

In the TOF-based artery mask large arteries were removed and small arteries selected. The pre- and post-contrast agent T_1- based angiogram reveals predominantly small arteries (since

the large arteries are subtracted due to fresh inflow) and possibly small veins. Therefore, it is possible that the T_1-based small arteries mask is contaminated with small veins and this would result in longer TA, rTTP and FWHM. However, the distribution of the T_1-based small artery mask is approximately Gaussian and does not show two peaks. In summary, the TOF-based small artery mask reflects more the arterial side of the vasculature, but does not show the smallest vessels, whereas the T_1-based angiogram selects smaller vessels but at risk of including veins.

The current study simulated PVEs in local AIF measurements for a large range of orientations and for different vessel radii. A previous simulation study reported that the broadening of the measured AIF profile in local AIF measurements is caused by the tissue response (14). This study shows that the broadening is not only caused by the tissue response in the surrounding but also by extravascular susceptibility effects and to a smaller extent by intravascular relaxation changes.

A broader AIF than the true AIF corrupts the perfusion estimates, and is likely to result in an overestimation of CBF. When comparing the CTCs of global AIFs to local AIFs, local AIFs are more delayed and more dispersed. The observed broadening is, however, much larger than one would expect based on the dispersion resulting from the transport properties of the vascular network.

The numerical model used in this study models the small brain-feeding artery as an infinite straight cylinder. The infinite cylinder is valid for a straight section at least four times the diameter of the vessel (30). Small arteries, however, often curve and can have branches. The orientation of the cylinder affects the extravascular susceptibility effects the most. Because the orientation is often unknown a full range of orientations were simulated and subsequently analyzed as a single group. Because the cylinder was simulated at different orientations, only the central voxels (that encompassed the middle of the vessel axis) of the volume were selected for local AIF measurements. This implies that voxels completely outside the small brain-feeding artery were not selected, because ΔR_2^* changes are too small in such voxels, since the extravascular effect drops off with distance.

In conclusion, partial-volume effects in local AIF measurements lead to broader ΔR_2^*-curves. These broader local AIFs will lead to errors in the perfusion estimates. Furthermore, automatic local AIF selections will not be able to select local AIF candidates without including gray matter profiles.

REFERENCES

1. Ostergaard L, Weisskoff RM, Chesler DA, Gyldensted C, Rosen BR. High resolution measurement of cerebral blood flow using intravascular tracer bolus passages .1. Mathematical approach and statistical analysis. Magnetic Resonance in Medicine 1996;36(5):715-725.
2. Rempp KA, Brix G, Wenz F, Becker CR, Guckel F, Lorenz WJ. Quantification of Regional Cerebral Blood-Flow and Volume with Dynamic Susceptibility Contrast-Enhanced Mr-Imaging. Radiology 1994;193(3):637-641.
3. Christensen S, Mouridsen K, Wu O, Hjort N, Karstoft H, Thomalla G, Rother J, Fiehler J, Kucinski T, Ostergaard L. Comparison of 10 Perfusion MRI Parameters in 97 Sub-6-Hour Stroke Patients Using Voxel-Based Receiver Operating Characteristics Analysis. Stroke 2009.
4. Emblem KE, Zoellner FG, Tennoe B, Nedregaard B, Nome T, Due-Tonnessen P, Hald JK, Scheie D, Bjornerud A. Predictive modeling in glioma grading from MR perfusion images using support vector machines. Magnetic Resonance in Medicine 2008;60(4):945-952.
5. Calamante F, Morup M, Hansen LK. Defining a local arterial input function for perfusion MRI using independent component analysis. Magnetic Resonance in Medicine 2004;52(4):789-797.
6. Mouridsen K, Christensen S, Gydensted L, Ostergaard L. Automatic selection of arterial input function using cluster analysis. Magnetic Resonance in Medicine 2006;55(3):524-531.
7. Murase K, Kikuchi K, Miki H, Shimizu T, Ikezoe J. Determination of arterial input function using fuzzy clustering for quantification of cerebral blood flow with dynamic susceptibility contrast-enhanced MR imaging. Journal of Magnetic Resonance Imaging 2001;13(5):797-806.
8. Calamante F, Gadian DG, Connelly A. Delay and dispersion effects in dynamic susceptibility contrast MRI: Simulations using singular value decomposition. Magnetic Resonance in Medicine 2000;44(3):466-473.
9. Vonken EPA, Beekman FJ, Bakker CJG, Viergever MA. Maximum likelihood estimation of cerebral blood flow in dynamic susceptibility contrast MRI. Magnetic Resonance in Medicine 1999;41(2):343-350.
10. Wu O, Ostergaard L, Weisskoff RM, Benner T, Rosen BR, Sorensen AG. Tracer arrival timing-insensitive technique for estimating flow in MR perfusion-weighted imaging using singular value decomposition with a block-circulant deconvolution matrix. Magnetic Resonance in Medicine 2003;50(1):164-174.
11. Calamante F, Yim PJ, Cebral JR. Estimation of bolus dispersion effects in perfusion MRI using image-based computational fluid dynamics. Neuroimage 2003;19(2):341-353.
12. Thijs VN, Somford DM, Bammer R, Robberecht W, Moseley ME, Albers GW. Influence of arterial input function on hypoperfusion volumes measured with perfusion-weighted imaging. Stroke 2004;35(1):94-98.
13. Bleeker EJ, van Buchem MA, van Osch MJ. Optimal location for arterial input function measurements near the middle cerebral artery in first-pass perfusion MRI. J Cereb Blood Flow Metab 2009;29(4):840-852.
14. Kjolby BF, Mikkelsen IK, Pedersen M, Ostergaard L, Kiselev VG. Analysis of Partial Volume Effects on Arterial Input Functions Using Gradient Echo: A Simulation Study. Magnetic Resonance in Medicine 2009;61(6):1300-1309.
15. van Osch MJP, van der Grond J, Bakker CJG. Partial volume effects on arterial input functions: shape and amplitude distortions and their correction. Journal of Magnetic Resonance Imaging 2005;22(6):704-709.
16. Lee JJ, Bretthorst GL, Derdeyn CP, Powers WJ, Videen TO, Snyder AZ, Markham J, Shimony JS. Dynamic Susceptibility Contrast MRI with Localized Arterial Input Functions. Magnetic Resonance in Medicine 2010;63(5):1305-1314.
17. Lorenz C, Benner T, Chen PJ, Lopez CJ, Ay H, Zhu MW, Menezes NM, Aronen H, Karonen J, Liu YW, Nuutinen J, Sorensen AG. Automated perfusion-weighted MRI using localized arterial input functions. Journal of Magnetic Resonance Imaging 2006;24(5):1133-1139.

18. Bjornerud A, Emblem KE. A fully automated method for quantitative cerebral hemodynamic analysis using DSC-MRI. J Cereb Blood Flow Metab 2010;30(5):1066-78.
19. Carroll TJ, Rowley HA, Haughton VM. Automatic calculation of the arterial input function for cerebral perfusion imaging with MR imaging. Radiology 2003;227(2):593-600.
20. Kim J, Leira EC, Callison RC, Ludwig B, Moritani T, Magnotta VA, Madsen MT. Toward fully automated processing of dynamic susceptibility contrast perfusion MRI for acute ischemic cerebral stroke. Comput Methods Programs Biomed 2010;98(2):204-13.
21. Mlynash M, Eyngorn I, Bammer R, Moseley M, Tong DC. Automated method for generating the arterial input function on perfusion-weighted MR imaging: Validation in patients with stroke. American Journal of Neuroradiology 2005;26(6):1479-1486.
22. Liu GY, Sobering G, Duyn J, Moonen CTW. A Functional Mri Technique Combining Principles of Echo-Shifting with A Train of Observations (Presto). Magnetic Resonance in Medicine 1993;30(6):764-768.
23. Duhamel G, Schlaug G, Alsop DC. Measurement of arterial input functions for dynamic susceptibility contrast magnetic resonance imaging using echoplanar images: Comparison of physical simulations with in vivo results. Magnetic Resonance in Medicine 2006;55(3):514-523.
24. van Osch MJP, Vonken EJPA, Wu O, Viergever MA, van der Grond J, Bakker CJG. Model of the human vasculature for studying the influence of contrast injection speed on cerebral perfusion MRI. Magnetic Resonance in Medicine 2003;50(3):614-622.
25. Lu HZ, Clingman C, Golay X, van Zijl PCM. Determining the longitudinal relaxation time (T-1) of blood at 3.0 tesla. Magnetic Resonance in Medicine 2004;52(3):679-682.
26. Golay X, Petersen ET, Hui F. Pulsed star labeling of arterial regions (PULSAR): A robust regional perfusion technique for high field imaging. Magnetic Resonance in Medicine 2005;53(1):15-21.
27. van Osch MJP, Vonken EJPA, Viergever MA, van der Grond J, Bakker CJG. Measuring the arterial input function with gradient echo sequences. Magnetic Resonance in Medicine 2003;49(6):1067-1076.
28. Kjolby BF, Ostergaard L, Kiselev VG. Theoretical model of intravascular paramagnetic tracers effect on tissue relaxation. Magnetic Resonance in Medicine 2006;56(1):187-197.
29. Bleeker EJW, van Osch MJP, Connelly A, van Buchem MA, Webb AG, Calamante F. A new criterion to aid manual and automatic selection of the arterial input function in dynamic susceptibility contrast MRI. Magnetic Resonance in Medicine 2011;65(2):448-456.
30. Bhagwandien R, Moerland MA, Bakker CJG, Beersma R, Lagendijk JJW. Numerical-Analysis of the Magnetic-Field for Arbitrary Magnetic-Susceptibility Distributions in 3D. Magnetic Resonance Imaging 1994;12(1):101-107.

Chapter 7 Discrete differences in brain perfusion between migraineurs and controls: a voxelwise comparison of interictal dynamic susceptibility contrast MRI measurements

Enrico B Arkink*, Egbert JW Bleeker*, Nicole Schmitz, Guus G Schoonman[1], Ona Wu[2], Michel D Ferrari[1], Mark A van Buchem, Matthias JP van Osch, Mark C Kruit

** First two authors contributed equally to this work*
1) Department of Neurology, Leiden University Medical Center, Leiden, the Netherlands
2) Martinos Center, Massachusetts General Hospital, Boston, Massachusetts

ABSTRACT

The increased cerebro- and cardiovascular risk in migraineurs may be the consequence of a basal systemic vascular susceptibility, reflected by the presence of interictal global or regional cerebral perfusion abnormalities. Whether focal perfusion changes occur during interictal migraine has not been convincingly demonstrated. In this study, we measured brain perfusion with dynamic susceptibility-contrast magnetic resonance imaging (DSC-MRI) in 30 interictal female migraineurs (13 migraine with aura (MA), 17 migraine without aura (MO)) and 17 female controls to improve our understanding of migraine pathophysiology and its potential cerebrovascular consequences. In voxelwise analyses ($p<0.001$, uncorrected, minimum cluster size 20 voxels), interictal hyperperfusion was observed in the left medial frontal gyrus in migraineurs and in the inferior and middle temporal gyrus in MO patients, in comparison to controls. Hypoperfusion was seen in the postcentral gyrus and in the inferior temporal gyrus in MA patients and in the inferior frontal gyrus in MO patients. Region-of-interest analyses of the pons, hypothalamus, occipital lobe and cerebellum did not show significant interictal perfusion differences between migraineurs and controls. We conclude that interictal migraine is characterized by discrete areas of hyper- and hypoperfusion unspecific for migraine pathophysiology and not explaining the increased vulnerability of particular brain regions for cerebrovascular damage.

In preparation

INTRODUCTION

Migraine is a prevalent neurovascular disorder, characterized by recurrent attacks of disabling headache accompanied by dysfunction of the autonomic nervous system. In up to a third of the patients, neurological (mostly visual) aura symptoms precede or accompany the headache phase of migraine attacks (1). Migraine, especially migraine with aura (MA), has been identified as an independent risk factor for clinical and subclinical brain infarction.(2, 3) The posterior circulation territory, notably the cerebellum, seems to be specifically vulnerable.(2, 4, 5) Further, female migraineurs both with and without aura are at increased risk of deep white matter and hyperintense brainstem lesions (2, 5, 6). Repetitive physiological and biochemical changes during migraine attacks, including changes in brain perfusion, are amongst the mechanisms proposed to explain or contribute to the increased risk of ischemic brain lesions (7).

Besides the increased risk of cerebrovascular complications in migraineurs, there is increasing evidence that migraine is also independently associated with other (ischemic) vascular disorders, including angina pectoris, myocardial infarction, claudication and retinopathy (7, 8). A direct relationship with migraine attacks is not plausible for these types of vascular disease, and therefore these associations seem to be better explained by a basal systemic susceptibility of the vasculature in migraine patients. Several lines of evidence support this concept, including interictal evidence of endothelium (dependent) dysfunction, impaired cerebrovascular reactivity, reports on ictal and interictal generalized or coronary artery vasospasm, impaired brachial artery compliance, increased aortic stiffness and hypercoagulability, which all seem to be independent of the coincidence of established cardiovascular risk factors (9).

Consequences of such basal vascular susceptibility may be reflected by the presence of interictal global or regional perfusion abnormalities in the brains of migraineurs. Earlier single photon emission computed tomography (SPECT) reported such gross differences in cerebral hemodynamics between interictal migraineurs and control subjects, but results were contradictory (10-15). More recent perfusion studies, using positron emission tomography (PET) (16-20) and dynamic susceptibility contrast magnetic resonance imaging (DSC-MRI) (21-23), concentrated on the ictal phenomena, so it has still not been convincingly proven whether in the interictal stage of migraine, differences in cerebral hemodynamics are present or absent in comparison with headache-free control subjects.

Knowledge of patterns of interictal brain perfusion will improve our understanding of the migraine pathophysiology and its potential consequences that could make certain brain areas in migraineurs more susceptible to temporary or permanent brain changes. Further, it serves as baseline measure for future analyses of brain perfusion changes during and around migraine attacks. In the current study, we investigated interictal groups of MA and migraine without aura (MO) patients vs. controls, using DSC-MRI. DSC-MRI has several advantages compared to earlier performed PET and SPECT studies, including a better spatial resolution with whole-brain coverage and a higher signal-to-noise ratio (SNR), allowing for voxelwise detection of small perfusion

differences (24). We performed unbiased whole brain voxelwise analyses of cerebral blood flow (CBF), cerebral blood volume (CBV), mean transit time (MTT) and time-to-peak (TTP) maps, but also performed region-of-interest analyses in predefined regions that have been reported to show perfusion changes during the different stages of migraine, or that have been reported to be specifically at risk for ischemic lesion development, such as the cerebellum.

METHODS

Subject population

Thirty female migraine patients (13 MA: mean age 42.9, range 28-52; 17 MO: mean age 47.6, range 38-57) and seventeen female control subjects (mean age 39.9, range 21-55) participated in this study. Migraine patients were enrolled through advertisements in newspapers and magazines. Migraineurs were diagnosed with MA or MO according to the criteria of the Headache Classification Committee of the International Headache Society (1) at the Department of Neurology (GGS); headache-free control subjects were recruited by local advertisement and enrolled in the study. None of the migraine patients were taking prophylactic medication and all were headache-free for 7 days or more at time of scanning (interictally). The study was approved by the local ethics committee and all subjects gave written and informed consent.

Neuroimaging protocol

T_2-weighted turbo spin echo images (TR/TE 4741/80 msec, echo train length 16, acquisition matrix 448x392 mm, FOV 224x180 mm^2, 48 slices of 3 mm thickness) and fluid-attenuated inversion recovery (FLAIR) (TR/TE 10128/120 msec, echo train length 36, acquisition matrix 224x224, FOV 224x180 mm^2, 48 slices of 3 mm thickness) were acquired and evaluated by an experienced neuroradiologist (MCK). Two cases showing structural brain abnormalities that could have impeded or confounded perfusion image post processing were excluded from further analyses: one control subject with a frontal cortical infarct, and one MA patient with confluent white matter lesions (WMLs). Small, punctuate deep white matter lesions were not considered an exclusion criterion.

DSC-MR imaging was performed on a 3.0 Tesla MRI system (Achieva, Philips Medical Systems, Best, The Netherlands), using an 8-channel receive array head coil; 0.2 ml/kg-bodyweight Gd-DTPA (Magnevist®, Schering) was injected intravenously at 5 ml/sec followed by a saline chaser of 25 ml (injected at 5 ml/sec (20 ml) and 2 ml/sec (5 ml)). PRESTO (PRinciples of Echo-Shifting with a Train of Observations, a 3D ultrafast gradient echo sequence combining whole brain coverage with T_2^*-weighted imaging (25)) was used for the acquisition with the following parameters: data matrix 64x53 mm (zerofilled to 128x108 mm), echo time (TE)/repetition time (TR) 26/17 msec, flip angle 5°, field of view (FOV) 224x168 mm^2, SENSE factor of 2.4, 48 slices of

3 mm thickness, number of echoes in a echo train 21, and 60 segments per volume resulting in a dynamic scan time of 1.1 sec.

Post-processing

The perfusion maps of CBF, CBV, MTT and TTP were generated using validated software developed at the Massachusetts General Hospital using block-circulant singular value decomposition (26). This program requires a manual selection of the arterial input function (AIF, the passage of contrast agent through a major brain-feeding artery). At least eight voxels near the middle cerebral artery were selected to form the global AIF used in the deconvolution.

The signal drop in the T_2^*-weighted images resulting from the contrast agent passage was converted to the concentration contrast agent (C(t)) using

$$C(t) \sim \Delta R_2^* = -\frac{1}{TE}\log\left(\frac{S(t)}{S(0)}\right) \quad [1]$$

The deconvolution was performed over the first and second passage of the gadolinium concentration passage with a noise threshold of 0.4 and an oscillation threshold of 0.095.

The CBF maps were used to coregister all perfusion maps spatially to the PET template in SPM5 (Wellcome Trust Centre for Neuroimaging, Institute of Neurology, UCL, London UK – http://www.fil.ion.ucl.ac.uk/spm). To improve the spatial normalization further, an average CBF map was constructed over all subjects and the individual CBF maps were coregistered to that average CBF template together with all other perfusion maps. The relative CBF and relative CBV maps were converted to quantitative CBF and CBV maps by setting the white matter CBF to 22 ml/100g/min (27). The white matter segmentation for this quantification step was performed in SPM5 on the CBF map, since gray matter has a higher CBF than white matter; the segmentation mask consisted of all voxels with a 95% or higher certainty that the voxel is white matter.

Statistical analyses

All perfusion maps were smoothed using an isotropic Gaussian kernel (full width at half maximum of 8 mm). Whole brain voxelwise comparison was performed, comparing interictal scans of patients with migraine, MA, MO and controls using one-way analyses of variance implemented in SPM5, correcting for age. For statistical tests, the height threshold was set at $p<0.001$, uncorrected for multiple comparisons, with a cluster extent of minimal 20 neighbouring voxels.

Next to voxel-based comparison, regions-of-interest (ROIs) for the occipital lobe and cerebellum (constructed from the corresponding regions from the automated anatomical labeling (AAL) template for SPM5) (28), the pons and the hypothalamus (drawn manually and incorporated into the AAL template) were created to study the average distribution of perfusion parameters in these areas in the normalized, non-smoothed images. The choice of ROIs

for pons, hypothalamus and occipital lobe was based on previous reports of hemodynamic changes during migraine (16, 18-20). The cerebellum was analyzed specifically because of its suggested increased vulnerability for cerebellar infarction in migraineurs. Distributions of mean CBF, CBV, MTT and TTP were compared between migraine patients and control subjects using multivariate general linear models adjusted for age in SPSS for Windows, release 16.0.2 (Chicago, USA).

RESULTS

After exclusion of the two participants with larger brain lesions, 45 female subjects remained for analysis: 12 MA patients, 17 MO patients, and 16 control subjects for further analysis. Mean age (MA 42.9±8.2 years, MO 47.6±5.3 years, controls (39.9±12.3), p>0.05, one-way ANOVA) was not different across the groups. The results of the voxelwise whole brain comparison between interictal migraineurs and controls are shown in Table 1 and Figures 1 and 2. We found a higher CBF in a part of the left medial frontal gyrus when analyzing the whole group of migraineurs vs. controls (Figure 1A).

Table 1 Significant differences in cerebral blood flow (CBF), cerebral blood volume (CBV), mean transit time (MTT) and time-to-peak (TTP) at interictal stage

		Brain area	MNI coordinates (x y z)	Cluster-size	Z-value
CBF					
Increased					
Migraine vs. controls	L	Medial frontal gyrus	-6 28 38	48	4.21
MA vs. controls	L	Medial frontal gyrus	-8 26 40	34	3.82
MO vs. controls	L	Medial frontal gyrus	-6 28 38	20	3.76
Decreased					
MA vs. controls	R	Inferior temporal gyrus	36 0 -50	49	4.47
	L	Postcentral gyrus	-48 -24 32	24	3.41
MO vs. controls	L	Inferior frontal gyrus	-54 20 32	26	3.82
CBV					
Increased					
MO vs. controls	R	Middle temporal gyrus	48 -16 -12	26	3.51
	R	Inferior temporal gyrus	38 -2 -48	30	3.41
			58 -30 -22	22	3.34
No decreases					
MTT					
No increases or decreases					
TTP					
No increases or decreases					

MA=migraine with aura, MO=migraine without aura, MNI=Montreal Neurological Institute; p<0.001, uncorrected, cluster extent threshold of 20 voxels

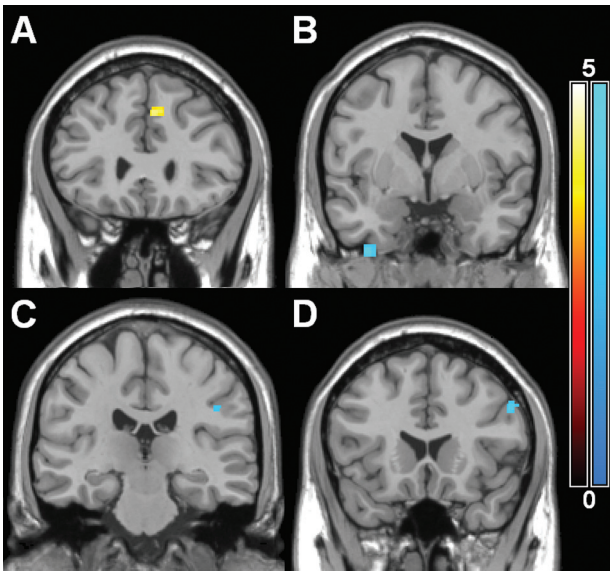

Figure 1: Statistical parametric maps demonstrating increases (yellow) and decreases (blue) in DSC-MRI measured cerebral blood flow (CBF). Increases in CBF between migraineurs and controls in the medial frontal gyrus (**A**) and decreases in CBF between MA patients and controls in the inferior temporal gyrus (**B**) and postcentral gyrus (**C**) and between MO patients and controls in the inferior frontal gyrus (**D**) are superimposed on a T_1-weighted template in MNI standard space. Color bars represent Z-values. The left side of each picture is the right side of the brain.

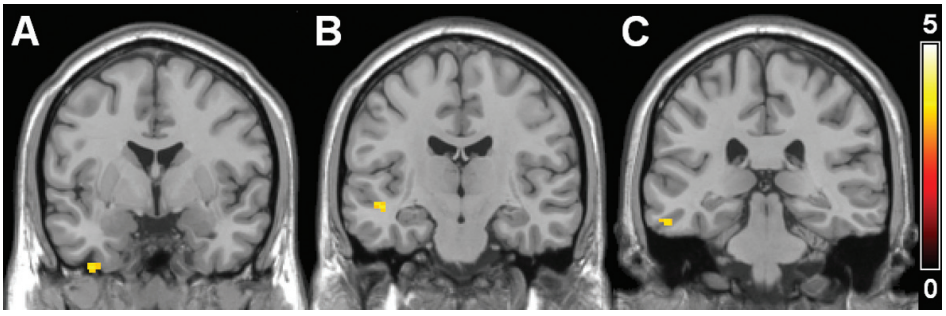

Figure 2: Statistical parametric maps demonstrating increases in DSC-MRI measured cerebral blood volume (CBV) in MO patients compared to headache-free control subjects in the inferior temporal gyrus (**A**,**C**) and middle temporal gyrus (**B**), superimposed on a T_1-weighted template in MNI standard space. Colour bars represent Z-values. The left side of each picture is the right side of the brain.

This difference remained, also when assessing MA and MO groups separately vs. controls (not shown in figure). A lower CBF was present in a zone of the right inferior temporal gyrus (figure. 1B) and the left postcentral gyrus (figure. 1C) in MA patients and in a part of the inferior frontal gyrus in MO patients (figure. 1D). CBV was increased in a zone of the right inferior and middle temporal gyrus in MO (Figure 2). CBV reductions were not identified. In addition, no

Table 2 Region-of-interest analyses cerebral blood flow (CBF), cerebral blood volume (CBV), mean transit time (MTT) and time-to-peak (TTP) for the pons, hypothalamus, occipital lobe and cerebellum at baseline, migraine and its subgroups vs. controls

	Pons		Hypothalamus		Occipital lobe		Cerebellum	
		p-value		p-value		p-value		p-value
CBF (ml/100g/min)								
Controls (n=16)	64.8 (9.9)		46.1 (6.0)		60.9 (8.4)		67.5 (9.6)	
Migraine (n=29)	64.1 (8.6)	0.312	44.2 (6.6)	0.362	59.1 (4.5)	0.504	64.7 (6.5)	0.888
MA (n=12)	63.8 (7.2)	0.683	41.1 (8.0)	0.089	61.0 (5.2)	0.389	66.4 (7.1)	0.846
MO (n=17)	64.4 (9.6)	0.172	46.3 (4.5)	0.777	57.9 (3.5)	0.736	63.5 (5.9)	0.915
CBV (ml/100g)								
Controls (n=16)	3.3 (0.6)		3.7 (0.7)		3.9 (0.7)		4.6 (1.0)	
Migraine (n=29)	3.3 (0.7)	0.526	3.8 (0.8)	0.197	4.0 (0.8)	0.184	4.7 (0.9)	0.316
MA (n=12)	3.4 (0.6)	0.520	3.6 (0.6)	0.676	4.0 (0.6)	0.432	4.6 (0.6)	0.657
MO (n=17)	3.3 (0.8)	0.694	3.9 (0.9)	0.091	4.1 (0.9)	0.121	4.7 (1.0)	0.191
MTT (s)								
Controls (n=16)	4.2 (0.5)		4.1 (0.7)		3.9 (0.5)		3.6 (0.4)	
Migraine (n=29)	4.5 (0.7)	0.273	4.4 (1.0)	0.232	4.1 (0.8)	0.250	3.8 (0.7)	0.283
MA (n=12)	4.3 (0.7)	0.678	4.1 (0.7)	0.955	3.9 (0.5)	0.774	3.7 (0.5)	0.629
MO (n=17)	4.6 (0.7)	0.127	4.6 (1.1)	0.061	4.3 (0.9)	0.111	3.9 (0.8)	0.161
TTP (s)								
Controls (n=16)	1.3 (0.5)		1.1 (0.5)		1.7 (0.5)		1.6 (0.5)	
Migraine (n=29)	1.5 (0.6)	0.316	1.4 (1.0)	0.197	1.9 (0.7)	0.566	1.8 (0.6)	0.718
MA (n=12)	1.4 (0.6)	0.499	1.4 (1.0)	0.253	1.8 (0.6)	0.847	1.7 (0.5)	0.935
MO (n=17)	1.6 (0.6)	0.192	1.4 (0.9)	0.141	2.0 (0.7)	0.357	1.9 (0.7)	0.448

MA=migraine with aura, MO=migraine without aura; denotation is mean (SD); p-values from linear regression models corrected for age

voxelwise increases or decreases in MTT and TTP were observed between migraineurs and control subjects.

The results of the ROI-analyses in interictal migraineurs and controls are shown in table 2. The CBF, CBV, MTT and TTP in pons, hypothalamus, occipital lobe and cerebellum did not differ significantly between migraine and controls, or between migraine subgroups and controls (Table 2).

DISCUSSION AND CONCLUSIONS

To the best of our knowledge, this is the first explorative DSC-MRI study assessing brain perfusion characteristics and patterns in female migraine patients in an interictal state vs. headache-free control subjects. In this relatively large sample of migraineurs (MA and MO) and control subjects, our voxelwise comparison of perfusion maps identified some small areas of perfusion differences between migraineurs and controls, including both hyper- and hypoperfusion in frontal, parietal, and temporal regions in the interictal migraine brain. Regional analyses assessing perfusion differences in the pons, hypothalamus, occipital lobe and cerebellum between

interictal migraineurs and controls did not show significant differences. In general, areas with altered interictal perfusion may reflect local interictal differences in neuronal activity or density, or may point at some degree of interictal cerebrovascular dysregulation, that both might be the consequence of repetitive migraine attacks, or might be attributed to systemic vascular processes, or both.

The area of higher CBF that we identified in the left medial frontal gyrus in both MA and MO patients, seems to co-localize with a reported area of gray matter reductions in migraine patients (29). Gray matter changes in the medial frontal gyrus have been reported to correlate with pain scores in another chronic pain condition, fibromyalgia (30), suggesting a correlation between morphology and function. In MA patients, we found lower CBF in the postcentral gyrus, part of the somatosensory cortex. One earlier morphometric study described thickening of the somatosensory cortex in migraineurs, that was suggested to be an adaptation to repetitive migraine attacks (31). In MO patients, we found areas of lower CBF in the inferior frontal gyrus and higher CBV in the middle temporal gyrus. Decreases in regional CBF in these areas were seen in MO patients after administration of sumatriptan in a recently published PET study (19), and an earlier voxel based morphometry (VBM) study in migraineurs also identified gray matter reductions in these gyri (32).

Although thus seemingly altered interictal perfusion in certain brain areas in migraineurs can be co-localized with earlier reported structural or hemodynamic changes in the brains of patients with migraine and other pain conditions, we want to stress that the changes measured by DSC-MRI are small and not necessarily specific for migraine. Further, higher or lower perfusion did not consistently relate to specific structural changes; e.g. hypoperfusion seems to be related in some areas with cortical thickening, and in other areas with gray matter reduction. This makes interpretation of these changes difficult.

We found no interictal differences in CBF, CBV, MTT or TTP in the regional maps of the pons, hypothalamus and occipital lobe, although perfusion changes have previously been identified in these areas during migraine attacks (16, 18-20). Similarly, we found no interictal perfusion abnormalities in the cerebellum. These negative interictal findings may be explained e.g. by high inter- and intra-individual variance in cerebral hemodynamics, and of course do not exclude the possibility of ictal perfusion changes in these areas.

We are not aware of any PET or DSC-MRI studies that report perfusion differences in migraineurs during interictal stage in comparison with control subjects. There are however several reports on interictal CBF changes in regular migraine compared to controls, measured with SPECT, but results are contradicting. Lauritzen et al. did not find interictal CBF changes when comparing 11 migraineurs to 20 controls (14). Levine et al. reported general hypoperfusion in 15 MA and 12 MO patients in the posterior circulation territory, compared to 20 controls (15). Other studies reported single or multiple foci of interictal hypoperfusion in 43-67% of migraineurs (10, 11). However, yet another SPECT study reported interictal global *hyper*perfusion in 50 MO patients (mainly located in frontal regions) and global *hypo*perfusion in 20

MA patients (mainly located in posterior regions), compared to control subjects (12). These contradicting results may be due to the insufficiency of visual evaluation of SPECT-derived CBF images to pick up abnormalities in interictal migraineurs (13). The small focal areas of hyper- and hypoperfusion we observed in frontal, temporal, and parietal regions in migraine patients compared to controls seem to show overlap with some of the regions found in the aforementioned SPECT studies, but comparison between these different techniques remains complicated because of differences in post-processing, which is discussed further below.

Up till now, DSC-MRI has been performed in only a few occasions in regular migraine (21-23); DSC-MRI has most often been used for studying perfusion changes during attacks of rare subforms of migraine, such as familial hemiplegic migraine or persistent migraine aura, most often only in a single case (33-40). The DSC-MRI acquisition and analysis in the current study was applied with more advanced acquisition and post-processing techniques than previously used in DSC-MRI studies in regular migraine (23). First, the 3D PRESTO acquisition in combination with parallel imaging covered the entire brain at a temporal resolution of 1.1 seconds. A low dynamic scan time is important because the concentration contrast agent is monitored dynamically, and a simulation study by Knutsson et al. showed that the dynamic scan time should be below 1.5 sec (41). Second, delay-insensitive deconvolution was used. This improves the quality of the perfusion estimates, since delay effects are more present when a global AIF is used for the deconvolution (26, 42). In our analysis, a global AIF was selected close but outside the middle cerebral arteries (43). These two brain-feeding arteries supply the majority of but not the entire cortex. However, the use of a delay insensitive deconvolution technique reduced the error for tissue that is not supplied by the MCA. Third, spatial normalization was performed in two steps, first to the PET template and second to an average CBF map. This improves the accuracy of the voxelwise comparison analysis.

Next to an increased spatial resolution allowing for voxelwise comparisons, DSC-MRI has several advantages compared to other techniques used for measuring perfusion in migraine. DSC-MRI does not expose the subjects to ionizing radiation and is therefore better suited for measuring cerebral perfusion in large samples of both migraineurs as well as controls than PET or SPECT. Further, DSC-MRI is more widely available and less time consuming. SPECT only measures CBF and some SPECT techniques provide only relative values, whereas PET and DSC-MRI measure values of CBF, CBV and MTT. Furthermore, the spatial resolution of PET and SPECT is lower than DSC-MRI making it harder to detect local perfusion changes. In the SPECT studies that compared interictal migraineurs to controls, images were acquired with varying SPECT-contrast agents and were often evaluated visually or semiquantitatively leading to a substantial degree of subjectivity. To overcome this problem, our results of local hyper- and hypoperfused areas between migraine attacks were generated by an unbiased whole brain voxelwise comparison of DSC-MRI images. Besides aforementioned advantages, DSC-MRI also has a major disadvantage. Recent studies showed that the (repetitive) use of DSC-MRI contrast agents in

patients with renal failure increases the risk for attaining nephrogenic systemic fibrosis (NSF) (44, 45).

Arterial spin-labeling (ASL) likely is a good alternative technique for both DSC-MRI and PET. ASL, a relatively new MR technique, is better for perfusion estimation and has the possibility for repeated measurements to increase the sensitivity (46). Although this technique only allows for absolute quantification of CBF (and not CBV or MTT), intravenous administration of contrast agents or radioactive tracers is not necessary. The first results of ASL during migraine attacks show results comparable to those in PET studies (47, 48).

In summary, our study shows in an unbiased whole brain voxelwise approach that interictal migraineurs have discrete areas of cerebral hyper- and hypoperfusion, measured with DSC-MRI. Their specifity for migraine pathophysiology is thought to be small, and we did not find changes in hemodynamics of interictal migraineurs that likely account for subclinical cerebellar lesions found previously.

REFERENCES

1. Headache Classification Subcommittee of the International Headache Society. The International Classification of Headache Disorders: 2nd edition. Cephalalgia 2004;24 Suppl 1:9-160.
2. Kruit MC, van Buchem MA, Hofman PA, Bakkers JT, Terwindt GM, Ferrari MD, Launer LJ. Migraine as a risk factor for subclinical brain lesions. JAMA 2004;291(4):427-434.
3. Schürks M, Rist PM, Bigal ME, Buring JE, Lipton RB, Kurth T. Migraine and cardiovascular disease: systematic review and meta-analysis. BMJ 2009;339:b3914.
4. Kruit MC, Launer LJ, Ferrari MD, van Buchem MA. Infarcts in the posterior circulation territory in migraine. The population-based MRI CAMERA study. Brain 2005;128(Pt 9):2068-2077.
5. Scher AI, Gudmundsson LS, Sigurdsson S, Ghambaryan A, Aspelund T, Eiriksdottir G, van Buchem MA, Gudnason V, Launer LJ. Migraine headache in middle age and late-life brain infarcts. JAMA 2009;301(24):2563-2570.
6. Kruit MC, Launer LJ, Ferrari MD, van Buchem MA. Brain stem and cerebellar hyperintense lesions in migraine. Stroke 2006;37(4):1109-1112.
7. Bigal ME, Kurth T, Hu H, Santanello N, Lipton RB. Migraine and cardiovascular disease: possible mechanisms of interaction. Neurology 2009;72(21):1864-1871.
8. Bigal ME, Kurth T, Santanello N, Buse D, Golden W, Robbins M, Lipton RB. Migraine and cardiovascular disease: a population-based study. Neurology 2010;74(8):628-635.
9. Tietjen GE. Migraine as a systemic vasculopathy. Cephalalgia 2009;29(9):987-996.
10. Calandre EP, Bembibre J, Arnedo ML, Becerra D. Cognitive disturbances and regional cerebral blood flow abnormalities in migraine patients: their relationship with the clinical manifestations of the illness. Cephalalgia 2002;22(4):291-302.
11. De Benedittis G, Ferrari Da Passano C, Granata G, Lorenzetti A. CBF changes during headache-free periods and spontaneous/induced attacks in migraine with and without aura: a TCD and SPECT comparison study. J Neurosurg Sci 1999;43(2):141-146.
12. Facco E, Munari M, Baratto F, Behr AU, Dal Palu A, Cesaro S, Giacomini M, Giron G. Regional cerebral blood flow (rCBF) in migraine during the interictal period: different rCBF patterns in patients with and without aura. Cephalalgia 1996;16(3):161-168.
13. Friberg L, Olesen J, Iversen H, Nicolic I, Sperling B, Lassen NA, Skyhøj Olsen T, Tfelt-Hansen P. Interictal 'patchy' regional cerebral blood flow patterns in migraine patients. A single photon emission computerized tomographic study. Eur J Neurol 1994;1:35-43.
14. Lauritzen M, Olesen J. Regional cerebral blood flow during migraine attacks by Xenon-133 inhalation and emission tomography. Brain 1984;107 (Pt 2):447-461.
15. Levine SR, Welch KM, Ewing JR, Robertson WM. Asymmetric cerebral blood flow patterns in migraine. Cephalalgia 1987;7(4):245-248.
16. Afridi SK, Giffin NJ, Kaube H, Friston KJ, Ward NS, Frackowiak RS, Goadsby PJ. A positron emission tomographic study in spontaneous migraine. Arch Neurol 2005;62(8):1270-1275.
17. Bahra A, Matharu MS, Buchel C, Frackowiak RS, Goadsby PJ. Brainstem activation specific to migraine headache. Lancet 2001;357(9261):1016-1017.
18. Denuelle M, Fabre N, Payoux P, Chollet F, Geraud G. Hypothalamic activation in spontaneous migraine attacks. Headache 2007;47(10):1418-1426.
19. Denuelle M, Fabre N, Payoux P, Chollet F, Geraud G. Posterior cerebral hypoperfusion in migraine without aura. Cephalalgia 2008;28(8):856-862.
20. Weiller C, May A, Limmroth V, Juptner M, Kaube H, Schayck RV, Coenen HH, Diener HC. Brain stem activation in spontaneous human migraine attacks. Nat Med 1995;1(7):658-660.
21. Cutrer FM, Sorensen AG, Weisskoff RM, Ostergaard L, Sanchez del Rio M, Lee EJ, Rosen BR, Moskowitz MA. Perfusion-weighted imaging defects during spontaneous migrainous aura. Ann Neurol 1998;43(1):25-31.

22. Linn J, Freilinger T, Morhard D, Bruckmann H, Straube A. Aphasic migraineous aura with left parietal hypoperfusion: a case report. Cephalalgia 2007;27(7):850-853.
23. Sanchez del Rio M, Bakker D, Wu O, Agosti R, Mitsikostas DD, Ostergaard L, Wells WA, Rosen BR, Sorensen G, Moskowitz MA, Cutrer FM. Perfusion weighted imaging during migraine: spontaneous visual aura and headache. Cephalalgia 1999;19(8):701-707.
24. Cavallin L, Axelsson R, Wahlund LO, Oksengard AR, Svensson L, Juhlin P, Wiberg MK, Frank A. Voxel-based correlation between coregistered single-photon emission computed tomography and dynamic susceptibility contrast magnetic resonance imaging in subjects with suspected Alzheimer disease. Acta Radiol 2008;49(10):1154-1161.
25. Liu G, Sobering G, Duyn J, Moonen CT. A functional MRI technique combining principles of echo-shifting with a train of observations (PRESTO). Magn Reson Med 1993;30(6):764-768.
26. Wu O, Østergaard L., Koroshetz WJ, Schwamm LH, O'Donnell J, Schaefer PW, Rosen BR, Weisskoff RM, Sorensen AG. Effects of tracer arrival time on flow estimates in MR perfusion-weighted imaging. Magn Reson Med 2003;50(4):856-864.
27. Østergaard L., Sorensen AG, Kwong KK, Weisskoff RM, Gyldensted C, Rosen BR. High resolution measurement of cerebral blood flow using intravascular tracer bolus passages. Part II: Experimental comparison and preliminary results. Magn Reson Med 1996;36(5):726-736.
28. Tzourio-Mazoyer N, Landeau B, Papathanassiou D, Crivello F, Etard O, Delcroix N, Mazoyer B, Joliot M. Automated anatomical labeling of activations in SPM using a macroscopic anatomical parcellation of the MNI MRI single-subject brain. Neuroimage 2002;15(1):273-289.
29. Kim JH, Suh SI, Seol HY, Oh K, Seo WK, Yu SW, Park KW, Koh SB. Regional grey matter changes in patients with migraine: a voxel-based morphometry study. Cephalalgia 2008;28(6):598-604.
30. Luerding R, Weigand T, Bogdahn U, Schmidt-Wilcke T. Working memory performance is correlated with local brain morphology in the medial frontal and anterior cingulate cortex in fibromyalgia patients: structural correlates of pain-cognition interaction. Brain 2008;131(Pt 12):3222-3231.
31. DaSilva AF, Granziera C, Snyder J, Hadjikhani N. Thickening in the somatosensory cortex of patients with migraine. Neurology 2007;69(21):1990-1995.
32. Rocca MA, Ceccarelli A, Falini A, Colombo B, Tortorella P, Bernasconi L, Comi G, Scotti G, Filippi M. Brain gray matter changes in migraine patients with T2-visible lesions: a 3-T MRI study. Stroke 2006;37(7):1765-1770.
33. Hsu DA, Stafstrom CE, Rowley HA, Kiff JE, Dulli DA. Hemiplegic migraine: hyperperfusion and abortive therapy with intravenous verapamil. Brain Dev 2008;30(1):86-90.
34. Jacob A, Mahavish K, Bowden A, Smith ET, Enevoldson P, White RP. Imaging abnormalities in sporadic hemiplegic migraine on conventional MRI, diffusion and perfusion MRI and MRS. Cephalalgia 2006;26(8):1004-1009.
35. Jäger HR, Giffin NJ, Goadsby PJ. Diffusion- and perfusion-weighted MR imaging in persistent migrainous visual disturbances. Cephalalgia 2005;25(5):323-332.
36. Lindahl AJ, Allder S, Jefferson D, Allder S, Moody A, Martel A. Prolonged hemiplegic migraine associated with unilateral hyperperfusion on perfusion weighted magnetic resonance imaging. J Neurol Neurosurg Psychiatry 2002;73(2):202-203.
37. Masuzaki M, Utsunomiya H, Yasumoto S, Mitsudome A. A case of hemiplegic migraine in childhood: transient unilateral hyperperfusion revealed by perfusion MR imaging and MR angiography. AJNR Am J Neuroradiol 2001;22(9):1795-1797.
38. Oberndorfer S, Wober C, Nasel C, Asenbaum S, Lahrmann H, Fueger B, Grisold W. Familial hemiplegic migraine: follow-up findings of diffusion-weighted magnetic resonance imaging (MRI), perfusion-MRI and [99mTc] HMPAO-SPECT in a patient with prolonged hemiplegic aura. Cephalalgia 2004;24(7):533-539.
39. Relja G, Granato A, Ukmar M, Ferretti G, Antonello RM, Zorzon M. Persistent aura without infarction: decription of the first case studied with both brain SPECT and perfusion MRI. Cephalalgia 2005;25(1):56-59.

40. San-Juan OD, Zermeno PF. Migraine with persistent aura in a Mexican patient: case report and review of the literature. Cephalalgia 2007;27(5):456-460.
41. Knutsson L, Stahlberg F, Wirestam R. Aspects on the accuracy of cerebral perfusion parameters obtained by dynamic susceptibility contrast MRI: a simulation study. Magn Reson Imaging 2004;22(6):789-798.
42. Calamante F, Gadian DG, Connelly A. Delay and dispersion effects in dynamic susceptibility contrast MRI: simulations using singular value decomposition. Magn Reson Med 2000;44(3):466-473.
43. Bleeker EJ, van Buchem MA, van Osch MJ. Optimal location for arterial input function measurements near the middle cerebral artery in first-pass perfusion MRI. J Cereb Blood Flow Metab 2009;29(4):840-852.
44. Idée JM, Port M, Medina C, Lancelot E, Fayoux E, Ballet S, Corot C. Possible involvement of gadolinium chelates in the pathophysiology of nephrogenic systemic fibrosis: a critical review. Toxicology 2008;248(2-3):77-88.
45. Thomsen HS, Marckmann P, Logager VB. Update on nephrogenic systemic fibrosis. Magn Reson Imaging Clin N Am 2008;16(4):551-60, vii.
46. Williams DS, Detre JA, Leigh JS, Koretsky AP. Magnetic resonance imaging of perfusion using spin inversion of arterial water. Proc Natl Acad Sci U S A 1992;89(1):212-216.
47. Kato Y, Araki N, Matsuda H, Ito Y, Suzuki C. Arterial spin-labeled MRI study of migraine attacks treated with rizatriptan. J Headache Pain 2010;11(3):255-258.
48. Pollock JM, Deibler AR, Burdette JH, Kraft RA, Tan H, Evans AB, Maldjian JA. Migraine associated cerebral hyperperfusion with arterial spin-labeled MR imaging. AJNR Am J Neuroradiol 2008;29(8):1494-1497.

Chapter 8 General discussion

The purpose of dynamic susceptibility contrast (DSC-) MRI is to provide hemodynamic parameters describing the microvascular blood supply to brain tissue. Quantification of the hemodynamic parameters has different aspects ranging from tracer kinetic theory to overcoming practical issues. For example, DSC-MRI uses a mathematical process (called deconvolution) for obtaining hemodynamic parameters from the tissue response (the passage of contrast agent through the microvasculature) and the AIF (the passage of contrast agent through the brain-feeding artery). In this mathematical process, the impulse response is calculated from the AIF and the tissue response. The impulse response only reflects properties of the capillaries, whereas the tissue response incorporates the total transport properties between the injection site and the capillaries. The hemodynamic properties of the capillaries are relevant for assessing brain diseases and pathologies.

In this chapter, the different aspects for perfusion quantification will be discussed, with a special focus on the AIF measurement. The first aspect is the tracer kinetic theory; this theory describes the physiological model for obtaining cerebral blood flow (CBF), cerebral blood volume (CBV) and mean transit time (MTT) from bolus passage measurements in tissue and a calibration measurement in the brain-feeding artery directly draining into the capillaries. Second, the influence of AIF measurements more upstream from the capillaries on the perfusion measurements is discussed. Because, in practice AIF measurements in DSC-MRI are most often performed near large brain-feeding arteries (e.g. middle cerebral artery) and not in the very small brain-feeding arteries that directly feed into the microvasculature. Third, a correct relation between the measured MR-signal and the concentration contrast agent is required for obtaining the perfusion parameters. Fourth, the sampling rate of the MR-signal changes is important as well as the effects of different sampling schemes. Fifth, different acquisition settings and their influence on the measured signal are described. Sixth, partial volume effects occur in DSC-MRI since the voxels are relatively large compared to the brain-feeding arteries supplying the microvasculature, and these partial volume effects can corrupt the AIF measurement. The seventh aspect is automatic AIF measurements for DSC-MRI: these are faster and user-independent. In this paragraph, the pros and cons of automatic AIF measurements are briefly discussed. After discussion of the different aspects in DSC-MRI, the limitations of the numerical models used in this thesis are discussed.

THE THEORY FOR PERFUSION MEASUREMENTS

The tracer kinetic theory developed by Zierler is used for determining the hemodynamic parameters CBF, CBV and MTT as measured with DSC-MRI (1). This theory is described in more detail in chapter 2. Below follows a summary of the theory.

A bolus of paramagnetic contrast agent is injected in the arm vein and flows through the heart, lungs and again through the heart before entering the oxygen rich arterial stream. Brain-feeding arteries feed the bolus contrast agent into the brain-tissue microvasculature. Therefore, the concentration of contrast agent of a voxel in tissue is dependent on the concentration of contrast agent in the feeding artery as can be seen in the following relation (see chapter 2 eq. 11):

$$c_t(t) = \frac{f}{V_{voxel}} \cdot \Re(t) \otimes c_{AIF}(t) \qquad [1]$$

where f / V_{voxel} equals the CBF except for some conversion factors, $\Re(t)$ is the residue function (the impulse response scaled to unity), $\otimes$ stands for a convolution and $c_{AIF}(t)$ is the concentration of contrast agent in the brain-feeding artery that supplies the tissue-microvasculature in the voxel.

Therefore, the CBF can be obtained by means of a deconvolution from the tissue passage curves with the AIF (keep in mind that $\Re(0)=1$):

$$CBF \cdot \Re(t) = c_t(t) \otimes^{-1} c_{AIF}(t) \qquad [2]$$

The CBV can be calculated from the product of the blood flow and the transport time function (see Chapter 2 eq. 14):

$$CBV = CBF \int_0^\infty \Re(t) dt \qquad [3]$$

Finally, the MTT of the blood through the capillary network can be calculated by using the central volume theorem, which describes the relation between CBF, CBV and the mean transit time (2, 3):

$$MTT = \frac{CBV}{CBF} \qquad [4]$$

As can be seen from eq. 3, the MTT can also be calculated by taking the area-under-the-curve of the residue function.

In theory, the CBV can also be calculated from the ratio of the areas-under-the-curve of the tissue passage curve and the AIF, although this results in slightly worse quantification than the product of the blood flow and the area under the hemodynamic response function due to difficulties in differentiating between the first passage and the recirculation (4).

If for some reason the $c_{AIF}(t)$ is over- or underestimated by a unknown factor then the CBV and CBF still would have correct relative values and because both parameters scale equally the MTT has a correct quantitative value. In this case, absolute quantification of CBV and CBF can be obtained by performing an additional absolute CBV measurement, for example by the steady state concentration (bookend method (5)) or by an additional absolute CBF measurement, such as arterial spin labeling (ASL) (6). However, both additional quantifications have their problems in absolute quantification. In ASL, the main problems are assessing the labeling efficiency and correction for transit delays and in the bookend method it is the estimation of the arterial MR-signal and the conversion from longitudinal (or transverse) relaxation rates to the concentration.

In the case that the shape of $c_{AIF}(t)$ is distorted then the deconvolution results in an erroneous estimation of all three hemodynamic parameters. A simulation study by Calamante et al. showed that perfusion errors are especially severe for distorted AIFs that exhibit a steeper upslope than the true $c_{AIF}(t)$ (7).

The theory for computing CBF, CBV and MTT assumes an intact blood-brain barrier (BBB), meaning that the vasculature from the calibration measurement to the tissue microvasculature must be intact. BBB breakdown occurs especially in high-grade tumors and stroke, and results in local increases in the concentration of the contrast agent in the measured tissue response and T_1-effects. Attempts have been made to overcome the problem of a broken BBB and Vonken et al. proposed a method to measure the extravasation of the contrast agent together with the hemodynamic parameters using model driven analysis of dual echo T_2^*-weighted images (8).

DELAY AND DISPERSION

As explained above the AIF should be measured in the small arteries directly supplying the capillaries. However, AIFs are commonly measured in arteries upstream from this ideal location. The $c_{AIF}(t)$ in the smaller brain-feeding artery is more delayed and dispersed than the $c_{AIF}(t)$ in the major brain feeding artery supplying that small artery (a result of the transport properties of the vascular tree). Deconvolution of the tissue response and an upstream AIF gives an impulse response that reflects the combined effect of the microvasculature and the vascular network from the location of the AIF measurement to the beginning of the capillaries. Correction for the induced error is not yet possible, because this would require extensive knowledge of the vascular network from the location of the AIF measurement up to the true AIF that feeds the capillaries. Several studies proposed methods to estimate dispersion or correct for dispersion.

Calamante et al. performed a finite elements model to estimate the dispersion effect in the internal carotid artery of patients with an occlusion in that segment (9). With these kind of calculations, one could predict the dispersion effect from the major brain-feeding artery (e.g. the internal carotid artery or the middle cerebral artery) to the true AIF, but it requires the geometric properties of the vascular tree and its vascular elastic properties. Blind deconvolution as proposed by Grüner et al. determines voxel-specific AIF and residue function using an iterative model-based blind deconvolution technique and thereby corrects the dispersion that would occur when a global AIF (e.g. near the middle cerebral artery) was used (10). A major disadvantage of obtaining the voxel-specific AIF and the impulse response from a single tissue response is that dispersion in the tissue response can be a result of a dispersed AIF as well as a broader impulse response, thereby making the blind deconvolution perfusion estimates sensitive to errors in the discrimination between AIF and impulse response.

Perfusion estimation with a global AIF and voxel-specific local or regional AIFs could provide insight into the vascular network between the two measurements, for example to asses an occlusion or stenosis in that part of the vascular network. This however requires two correct AIF measurements and an error in either will lead to incorrect assessment of the occlusion or stenosis.

DETERMINING THE CONCENTRATION OF CONTRAST AGENT

In DSC-MRI, the concentration of contrast agent in tissue and in the brain-feeding artery is determined using T_2^*-weighted images and sometimes using T_2-weighted images. This is possible because increasing the concentration of paramagnetic contrast agent shortens the T_2 relaxation time and induces local field disturbances in the surrounding of the vasculature. The net effect is signal dephasing and therefore a signal decrease in the $T_2^{(*)}$-weighted images.

The $T_2^{(*)}$-weighted profiles are normally transformed to $\Delta R_2^{(*)}$ via:

$$\Delta R_2^{(*)}(t) \equiv \frac{1}{T_2^{(*)}(t)} - \frac{1}{T_2^{(*)}(0)} = \frac{1}{TE} \ln\left(\frac{S(0)}{S(t)}\right) \qquad [5]$$

where $T_2^{(*)}$ is the transverse relaxation time that changes in time due to the bolus passage, TE is the echo time and S is the magnitude of the MR-signal in time.

The ΔR_2^* profile of tissue is heavily weighted by the local field disturbances caused by the susceptibility effects (11). The simulations of Kjølby and coworkers showed a linear relation between ΔR_2^* and $c_t(t)$. However, the results of chapter 5 provide some evidence that this does not hold true in vivo. In chapter 5, we found that the ratio of the area-under-the-curve of the first passage to the steady state was different for white matter and gray matter ΔR_2^* profiles, suggesting a non-linearity in the relation between the concentration of contrast agent and the

ΔR_2^*. The non-linearity could be caused by a different organization of the microvasculature of gray matter and white matter. In cortical gray matter, the small feeding arteries entering gray matter run perpendicular to the surface of gray matter and then within the gray matter layers spread out parallel to the surface of gray matter. The arterioles and capillaries have a more random organization. In white matter, the organization of the small feeding arteries is more random making the overall organization of the vasculature more random. The model of Kjølby and coworkers assumed a random organization of the small arteries, arterioles and capillaries, which is valid for white matter but not for gray matter. An alternative reason for the non-linearity could be the fact that the static dephasing regime does not hold for low concentrations (12), since in white matter the concentrations of contrast agent are much lower than in gray matter due to the lower vascular density. Finally, it could be due to the fact that dephasing is expected to level off at higher concentrations in the more dense vascular network of gray matter, since the simulations of Kjølby et al. only modeled a single capillary and not the overlapping local field changes of multiple capillaries. For instance, the space between two parallel capillaries in the plane perpendicular to the main magnetic field can be less inhomogeneous because the local field changes in between the two capillaries add up, leading to a reduced gradient. The reduction in local field gradients leads to reduced dephasing much larger than two capillaries. This of course applies for the space between any set of capillaries with non-parallel orientations to the main magnetic field.

The difference in phase of the MR-signal (with respect to the phase before contrast administration ($\Delta\varphi$)) of a tissue-voxel is close to zero for randomly oriented capillaries. However, there can be a net phase effect when the microvasculature is not randomly oriented, but determining the relation is very difficult because this requires detailed information of the organization of the microvasculature. A possible experiment could be to measure the $\Delta\varphi$ of a capillary phantom such as proposed by Anderson et al. at ISMRM 2010 (13). That phantom used parallel capillaries; however, it would be necessary to use a (more) randomly oriented capillary phantom. Local $\Delta\varphi$ changes in the brain can be observed in the DSC-MRI scan, due to the susceptibility effects of larger, less random oriented vessels. Alternatively, gyrus and sulcus structures of cortical gray matter or the shapes of other brain structures can lead to susceptibility effects in and around these structures resulting in phase effects dependent on the concentration of contrast agent. However, the overall $\Delta\varphi$ change in time is expected to be close to zero, since the cortex has a more or less spherical shape and the internal net phase effect of a sphere is zero and averaged over the entire cortex the vessels are more randomly oriented.

The ΔR_2^* profile in blood is quadratically related to the concentration of contrast agent and depends on the hematocrit level (14, 15). This quadratic relationship was determined for Gd-DTPA in whole blood at 1.5 T (15). It would be interesting to know how this quadratic relation scales with the field strength. We attempted such an experiment where we tried to mimic blood with a mixture of yeast and water, since yeast cells have a similar diameter to a red blood cell. Interestingly, the experiment did not show a quadratic relation at 1.5 T for Gd-DTPA. The

experiments at 7 T showed also a much smaller quadratic relation for Gd-DTPA than expected. A possible explanation is that red blood cells have more of a donut shape whereas yeast cells are spherical, thereby changing the susceptibility effects outside the cell. Alternatively, the difference in the water exchange rate in the cells could be an explanation for the absence of a quadratic relation. Furthermore, the temperature was different from the blood experiments because we used regular tap water, in future experiments this can easily be controlled. The two measurements did however show a linear scaling with field strength for the linear relation between the ΔR_2^* and the concentration of contrast agent. This finding encouraged us to use a linear scaling with field strength for the simulations of the local AIF measurements in chapter 6.

The $\Delta\varphi$ can also be used to determine the concentration of contrast agent inside a brain-feeding artery. The susceptibility effect of the contrast agent induces local field changes in and around the vasculature (except for parallel arteries and arteries oriented at the magic angle). Inside the artery, the local field change is homogenous and can be positive (θ<magic angle), zero (magic angle) or negative (θ>magic angle) for increasing concentrations of contrast agent. These local field changes can be measured by the phase of the gradient echo MR-signal. A potential benefit of measuring the phase is that it is independent of changes in T_1 and T_2 relaxivity. Another benefit is that the phase change inside the artery is linearly related to the concentration of contrast agent.

Because the susceptibility difference inside the artery induces local field changes outside the non-parallel arteries, the concentration of contrast agent inside the arteries can also be measured outside large (non-parallel) arteries via the magnitude or the phase of the MR-signal of T_2^*-weighted images (see chapter 3 and 4). Both signal parts are influences by the local field changes outside the artery, which are the strongest for a perpendicular orientation with respect to the main magnetic field and absent for arteries oriented parallel to B_0. Simulations showed that the correlation with the ground truth for phase-based extravascular AIF measurement was high (ρ>0.99) superior, inferior, anterior and posterior to perpendicular oriented arteries. However, whether this relation is truly linear is still a question. In the simulation of chapter 4, we observed that the relation is not exactly linear but that the peak was slightly underestimated. An analytical determination of the relation between the phase and the dephasing (due to the local field changes) in a voxel outside non-parallel arteries would be interesting. Because the tissue response often hamper the AIF measurement, the very small tissue response is beneficial for phase-based extravascular AIF measurements. In magnitude-based extravascular AIF measurements, the concentration determination is hampered by the larger tissue response (see chapter 3).

In T_2-weighted images, the 180° pulse of such spin echo sequences refocuses the local field changes and the T_2 signal is only sensitive to the relaxivity and diffusion over the local field changes. Because the local field changes are refocused, extravascular AIF measurements are not well understood at the moment. However, in practice the AIF in T_2-weighted images is determined outside large arteries, such as the middle cerebral artery. Phase-based AIF

measured are in theory not possible. Boxerman et al. showed that the sensitivity of the ΔR_2 drops off for vessels larger than 30-50 μm (16). Whether this is true for much larger arteries is up to now unanswered. Therefore, AIF measurements in or near brain-feeding arteries such as the middle cerebral artery or the internal carotid artery measured with spin echo acquisition could be the topic for future studies.

DISCRETE SAMPLING

The concentration profile cannot be determined continuously, it has to be sampled in time. A simulation study by Knutsson et al. showed that the temporal resolution should be below 1.5 seconds because otherwise the CBF will be underestimated (17). For such temporal resolutions, fast imaging acquisitions such as single shot EPI, segmented EPI or spiral readouts are required.

Single shot EPI has a relatively long echo-train length (ETL). The effect of a long ETL in the readout is image distortion especially when susceptibility differences are present (e.g. near air cavities). Segmented EPI measures k-space in multiple shots, with each shot having a shorter ETL, resulting in fewer distortions. However, head motion between shots can result in artifacts.

Because for real objects the upper half of k-space is the complex conjugate of the lower half, one half can be reconstructed from the other half without actually acquiring the data. Acquisition of (a bit more than) half of k-space and reconstructing the other half is called partial Fourier. The benefit of partial Fourier is a reduction in ETL in single shot EPI with an equal imaging matrix. A disadvantage is a reduction in baseline signal-to-noise.

Finally, DSC-MRI can benefit from the advantages of parallel imaging (e.g. SENSE or GRAPPA (18, 19)). Parallel imaging requires additional hardware (multichannel receive coils) and software but it can accelerate the acquisition. One of the possibilities with the accelerated acquisition is increasing the temporal resolution thereby decreasing the distortion artifacts (because the ETL is reduced). The accelerated acquisition can also be used to increase the spatial resolution or increase coverage, since these three measurement parameters are all interrelated.

EFFECTS OF ACQUISITION SETTINGS IN DSC-MRI

As for every measurement, DSC-MRI measurements are subject to noise. A huge benefit is that the induced ΔR_2^* signal is large compared to the noise level and signal averaging need not to be performed. The noise is Gaussian in k-space (the raw data of the MRI scanner) and after reconstruction (via inverse Fourier transformation) Gaussian in image space (the real and imaginary images). The noise in the magnitude is Rician and for high signal to noise ratios (SNR) close to a Gaussian distribution. The noise in the phase image depends on the magnitude and

at very low signal magnitudes the phase is difficult to determine and so called "salt and pepper" noise is observed.

The baseline SNR (of a single image) depends on the hardware, field strength, the voxel size, the TE and for gradient echo acquisition also on the flip angle (FA). Increasing the voxel size increases the baseline SNR and lowers the spatial resolution. Lowering the TE increases the baseline SNR in $T_2^{(*)}$-weighted images but influences the signal-to-noise of the bolus passage measurement. In addition, an FA at the Ernst angle has the highest SNR.

An increase in concentration of contrast agent results in a magnitude decrease in T_2^*-weighted images. The decrease in magnitude depends on the TE, the concentration contrast agent and the field strength. The concentration of contrast agent is higher in the larger brain-feeding arteries than in the capillaries therefore signal dropout occurs quicker in the larger arteries. At 3 Tesla the baseline SNR is nearly double the baseline SNR of 1.5 Tesla. However, the magnitude decrease is linear with field strength and therefore the magnitude drops faster for increasing concentration contrast agent. For this reason in the LUMC, a single dose contrast agent (0.1 mmol/kg-bodyweight Gd-DTPA) is injected into the arm vein when the patient is scanned at 3 Tesla and a double dose (0.2 mmol/kg-bodyweight Gd-DTPA) is injected when the patient is scanned at 1.5 Tesla. Lowering the echo time could prevent signal depletion but a disadvantage is that the much lower concentrations of contrast agent in tissue are difficult to measure with a short TE. Therefore, dual echo acquisition can be used with an optimal TE for both the AIF and the tissue response, although this can lower spatial resolution, SNR or coverage.

Single shot EPI has a repetition time (TR) exactly the same as the dynamic scan time or temporal resolution. In segmented EPI, the TR is lower than the temporal resolution because a single image is acquired with several shots. PRESTO a segmented EPI technique with echo shifting has a TR shorter than the echo time (TE). Because the contrast agent not only affects the transverse relaxivity but also the longitudinal relaxivity, a shorter TR increases the contrast agent T_1 relaxivity effect in the T_2^*-weighted images. The influence of T_1-effects on the concentration of contrast agent estimation is shown in chapter 5, figure 3. The initial dip is characteristic as well as the lower steady state. Dual echo acquisition is not only beneficial for optimal echo time for AIF and tissue but makes correction for T_1-effects in tissue possible (20, 21). Alternatively, the flip angle can be lowered to reduce the T_1-effects but this is at the cost of baseline SNR.

PARTIAL VOLUME EFFECTS

Larger voxels are beneficial for baseline SNR but also have a downside. Not only does this result in decreased spatial resolution of the perfusion maps, but also results in partial volume effects of the AIF since, the size of the voxels used in DSC-MRI will be larger than the brain-feeding arteries. Therefore, pure intravascular AIF measurements are not possible and so-called partial

volume effects hamper the ΔR_2^*, ΔR_2 and $\Delta\varphi$ AIF measurements. The partial volume effects not only lead to scaling errors in gradient echo magnitude-based AIF measurements but also shape errors, which lead to erroneous perfusion estimates. In this section, the partial volume effects in gradient echo acquisition will be discussed. Partial volume effects can be corrected for when the artery is oriented parallel to the main magnetic field (22). However, measuring the AIF in the internal carotid artery (ICA, which is approximately parallel to B_0) requires an extra slice in the neck leading to reduced brain coverage. Furthermore, the ICA is a large brain-feeding artery and therefore signal saturation occurs sooner.

Partial volume effects alter the complex trajectory of the bolus passage and therefore affect the magnitude and phase-based AIF measurements. Partial volume effects originating from voxels encompassing non-parallel brain-feeding arteries can and often will severely corrupt the shape of the measured AIF. An alternative is to measure the AIF outside the brain-feeding artery in homogeneous tissue where there are no partial volume effects of tissue with arterial signal. However, this requires strong induced local field changes in the surrounding. The local field changes are the strongest for perpendicular oriented arteries. The middle cerebral artery (MCA) is oriented approximately perpendicular to the main magnetic field and therefore ideal for extravascular AIF measurements. Extravascular AIF measurements are best performed using the phase of the MR-signal (as shown in chapter 4)

Partial volume effects also corrupt AIF measurements in small brain-feeding arteries, which are closer to the microvasculature (thereby reducing the delay and more importantly the dispersion effects). Local AIF measurements completely outside small brain-feeding arteries are not feasible because the induced local field changes are low (since the local field change depends on the radius of the artery). Therefore, local or regional AIF measurements are performed with voxels encompassing the small brain-feeding artery. These voxels are always hampered by partial volume effects but the partial volume shape error varies. If the shape error is minimal than the tissue response in the voxel can still lead to additional broadening, since the signal fraction of the tissue response is much larger in the local AIF measurements.

For future studies, it could be interesting to investigate the extent of the scaling and shape error in spin echo magnitude based global and local AIF measurements.

AUTOMATIC SELECTION

Instead of using anatomical information to select the AIF, automatic selection criteria can select AIF candidates based on the shape of the bolus passage. Up to now automatic selection programs only focus on magnitude-based AIF measurements and not on phase-based AIF measurements. Different approaches have been employed such as independent component analysis, fuzzy clustering or factor analysis (23-25).

An advantage of automatic AIF selection is that it provides fast, user independent and reproducible results. The disadvantage is that the automatic AIF selection can determine ΔR_2^* profiles to be correct when in fact the profile is corrupted by partial volume effects. Our proposed criterion (described in chapter 5) can help in preventing part of the selection bias. This criterion is especially advantageous for detecting PVEs that have a smaller width and higher peak than the true arterial response, since these are not excluded by the current automatic AIF selection criteria.

Automatic AIF measurements focus on local AIF measurements and use specific selection criteria. However, as discussed in chapter 6 partial volume effects in voxels encompassing a small brain-feeding artery lead to broader curves. Therefore, automatic methods are likely to select broader curves, which do not reflect the concentration-time curve of small brain-feeding arteries.

LIMITATIONS OF THE NUMERICAL MODELS

The numerical models of this thesis are focused on gradient echo arterial input function measurements in DSC-MRI. One numerical model (Model 1) (discussed in chapter 3, 4 and 5) simulated AIF measurements near a perpendicular oriented artery for different fast imaging sequences (single shot EPI, segmented EPI and PRESTO). Another numerical model (Model 2) simulated local AIF measurements at various orientations without incorporating the effects of fast imaging sequences (chapter 6).

Both models assumed an infinitely long straight vessel without arterial branches. Model 1 simulated an artery such as the MCA, which is oriented approximately perpendicular to the main magnetic field. This model is valid for a straight artery at least four times the diameter (26). The M1 segment of the MCA is often a straight part and, in the middle of the M1 segment, the assumption does hold. There are, however, often branches corrupting the local field surrounding the artery. Model 2 simulated smaller arteries than the MCA. These arteries are more likely to curve and have branches.

The surroundings of the artery were modeled as homogeneous tissue. However, arteries in the brain are surrounded by muscle, CSF, gray matter tissue and white matter tissue. The structures close to the vessel wall give additional partial volume effects. This thesis showed that two compartment partial volume effects can cause huge shape errors. Because partial volume effects of two compartments already produce a huge variation of shape errors, more compartments will not produce more shape errors.

The model assumed no phase effect in tissue, but as discussed above there could be a small tissue phase effect. Such a tissue phase response would hamper the extravascular phase-based AIF measurements. Magnitude-based extravascular AIF measurements are susceptible to relaxation changes and to the passage of contrast agent through tissue. The tissue response

was incorporated in the model using a linear relation. The relation could differ from in vivo as explained above.

Model 1 was created with the option to rotate the slices around the vessel axis. Tilting the slices around the vessel axis results in the same (rotated) locations for AIF measurements (data not shown). The effect of other rotations of the vessel axis was not investigated but since the optimal AIF measurements are outside the artery we would expect this criteria to hold for small angulations of the vessel axis. The numerical model was validated using phantom experiments. This comparison supported the idea that the most important effects were included in the model. The effect of diffusion was, for example, not included. In a numerical model for T_2-based AIF measurements diffusion should play a more prominent role.

REFERENCES

1. Zierler KL. Theoratical basis of indicator-dilution methods for measuring flow and volume. Circ Res 1962;10:393-407.
2. Meier P, Zierler KL. On the Theory of the Indicator-Dilution Method for Measurement of Blood Flow and Volume. Journal of Applied Physiology 1954;6(12):731-744.
3. Stewart GN. Researches on the circulation time in organs and on the influences which affect it. Part I-III. J Physiolo (London) 1894;15:1.
4. Perkio J, Soinne L, Ostergaard L, Helenius J, Kangasmaki A, Martinkauppi S, Salonen O, Savolainen S, Kaste M, Tatlisumak T, Aronen HJ. Abnormal intravoxel cerebral blood flow heterogeneity in human ischemic stroke determined by dynamic susceptibility contrast magnetic resonance imaging. Stroke 2005;36(1):44-49.
5. Sakaie KE, Shin W, Curtin KR, McCarthy RM, Cashen TA, Carroll TJ. Method for improving the accuracy of quantitative cerebral perfusion imaging. Journal of Magnetic Resonance Imaging 2005;21(5):512-519.
6. Williams DS, Detre JA, Leigh JS, Koretsky AP. Magnetic-Resonance-Imaging of Perfusion Using Spin Inversion of Arterial Water. Proceedings of the National Academy of Sciences of the United States of America 1992;89(1):212-216.
7. Calamante F, Connelly A. DSC-MRI: How accurate does the arterial input function need to be in practice? Pro. Int. Soc. Mag. Reson. Med. 15; 2007.
8. Vonken EJPA, van Osch MJP, Bakker CJG, Viergever MA. Simultaneous quantitative cerebral perfusion and Gd-DTPA extravasation measurement with dual-echo dynamic susceptibility contrast MRI. Magnetic Resonance in Medicine 2000;43(6):820-827.
9. Calamante F, Yim PJ, Cebral JR. Estimation of bolus dispersion effects in perfusion MRI using image-based computational fluid dynamics. Neuroimage 2003;19(2):341-353.
10. Gruner R, Taxt T. Iterative blind deconvolution in magnetic resonance brain perfusion imaging. Magnetic Resonance in Medicine 2006;55(4):805-815.
11. Kjolby BF, Ostergaard L, Kiselev VG. Theoretical model of intravascular paramagnetic tracers effect on tissue relaxation. Magnetic Resonance in Medicine 2006;56(1):187-197.
12. Kiselev VG. On the theoretical basis of perfusion measurements by dynamic susceptibility contrast MRI. Magnetic Resonance in Medicine 2001;46(6):1113-1122.
13. Anderson JR, Ackerman JJ, Garbow JR. Towards more accurate modeling of DCE data: development of multi-compartment phantom. Pro. Int. Soc. Mag. Reson. Med. 18; 2010. 631.
14. Akbudak, E, Hsu, RM, Li, Y, and Conturo, TE. ΔR2* Δφ contrast agent perfusion effects in blood: quantitation and linearity assessment. In:Proceedings of the ISMRM 6th Annual Meeting, Sydney, 1998, p1197.
15. van Osch MJP, Vonken EJPA, Viergever MA, van der Grond J, Bakker CJG. Measuring the arterial input function with gradient echo sequences. Magnetic Resonance in Medicine 2003;49(6):1067-1076.
16. Boxerman JL, Hamberg LM, Rosen BR, Weisskoff RM. Mr Contrast Due to Intravascular Magnetic-Susceptibility Perturbations. Magnetic Resonance in Medicine 1995;34(4):555-566.
17. Knutsson L, Stahlberg F, Wirestam R. Aspects on the accuracy of cerebral perfusion parameters obtained by dynamic susceptibility contrast MRI: a simulation study. Magnetic Resonance Imaging 2004;22(6):789-798.
18. Griswold MA, Jakob PM, Heidemann RM, Nittka M, Jellus V, Wang JM, Kiefer B, Haase A. Generalized Autocalibrating Partially Parallel Acquisitions (GRAPPA). Magnetic Resonance in Medicine 2002;47(6):1202-1210.
19. Pruessmann KP, Weiger M, Scheidegger MB, Boesiger P. SENSE: Sensitivity encoding for fast MRI. Magnetic Resonance in Medicine 1999;42(5):952-962.
20. Perman WH, Gado MH, Larson KB, Perlmutter JS. Simultaneous Mr Acquisition of Arterial and Brain Signal Time Curves. Magnetic Resonance in Medicine 1992;28(1):74-83.

21. Vonken EJPA, van Osch MJP, Bakker CJG, Viergever MA. Measurement of cerebral perfusion with dual-echo multi-slice quantitative dynamic susceptibility contrast MRI. Jmri-Journal of Magnetic Resonance Imaging 1999;10(2):109-117.
22. van Osch MJP, van der Grond J, Bakker CJG. Partial volume effects on arterial input functions: shape and amplitude distortions and their correction. Journal of Magnetic Resonance Imaging 2005;22(6):704-709.
23. Calamante F, Morup M, Hansen LK. Defining a local arterial input function for perfusion MRI using independent component analysis. Magnetic Resonance in Medicine 2004;52(4):789-797.
24. Knutsson L, Larsson EM, Thilmann O, Stahlberg F, Wirestam R. Calculation of cerebral perfusion parameters using regional arterial input functions identified by factor analysis. Journal of Magnetic Resonance Imaging 2006;23(4):444-453.
25. Murase K, Kikuchi K, Miki H, Shimizu T, Ikezoe J. Determination of arterial input function using fuzzy clustering for quantification of cerebral blood flow with dynamic susceptibility contrast-enhanced MR imaging. Journal of Magnetic Resonance Imaging 2001;13(5):797-806.
26. Bhagwandien R, Moerland MA, Bakker CJG, Beersma R, Lagendijk JJW. Numerical-Analysis of the Magnetic-Field for Arbitrary Magnetic-Susceptibility Distributions in 3D. Magnetic Resonance Imaging 1994;12(1):101-107.

Summary

The main topic of this thesis is to improve quantification of brain-perfusion measured with dynamic susceptibility contrast (DSC-) MRI. The improvements were primarily made on the arterial input function (AIF) measurement, which calibrates the hemodynamic parameters. Manual and automatic AIF selection were investigated as well global and local or regional AIF selection.

Chapter 1 is a short introduction that introduces the magnetic resonance imaging technique dynamic susceptibility contrast MRI. This chapter introduces also the term arterial input function and the relevance of a correct arterial input function in dynamic susceptibility contrast MRI.

Chapter 2 is a review about two MRI techniques for measuring brain-perfusion. Perfusion MRI techniques can be categorized in two different groups based on tracer type. First, DSC-MRI is a method based on the injection of an exogenous tracer, a gadolinium-based contrast agent, in the arm vein. By means of fast T_2 or T_2^*-weighted imaging the first passage of the contrast agent through the brain tissue is monitored. The second technique, arterial spin labeling (ASL), is a completely non-invasive technique that employs water protons as an endogenous tracer. In this chapter, the crucial elements for correct perfusion measurements by DSC-MRI and ASL are discussed. In DSC-MRI, the conversion from signal changes to concentration contrast agent, the arterial input function measurement and the deconvolution method are the most important elements. Whereas in ASL, the efficiency of the labeling method, correction for relaxation processes, and M_0-calibration methods can be considered the most essential components of blood flow quantification.

Chapter 3 provides insight in magnitude-based manual AIF selection near the middle cerebral artery (MCA) using numerical modeling. One of the main difficulties in obtaining quantitative perfusion values from DSC-MRI is a correct AIF measurement, as partial volume effects can lead to an erroneous shape and amplitude of the AIF. Cerebral blood flow and volume scale linearly with the area under the AIF, but shape changes of the AIF can lead to large, nonlinear errors. A numerical model, validated by phantom experiments, was used for predicting the optimal location for AIF measurements in the vicinity of the middle cerebral artery. The findings are fourfold: AIF measurements should be performed in voxels completely outside the artery, here a linear relation should be assumed between ΔR_2^* and the concentration contrast agent, the

exact optimal location differs per acquisition type, and voxels including a small middle cerebral artery yield also correct AIF measurements for segmented EPI when a short echo time is used.

Chapter 4 provides insight in phase-based manual AIF selection near the middle cerebral artery using the numerical model of chapter 3. In dynamic susceptibility contrast perfusion MRI arterial input function measurements using the phase of the MR signal are commonly performed inside an artery. However, phase-based AIF selection is also feasible in tissue surrounding an artery such as the MCA, which runs approximately perpendicular to B_0, since contrast agents also induce local field changes in tissue surrounding the artery. The aim of this study was to investigate whether phase-based AIF selection is better performed in tissue just outside the MCA than inside the artery. Additionally, phase-based AIF selection was compared to magnitude-based AIF selection. Three main findings are presented: first, phase-based AIF selections are better made in tissue outside the MCA rather than within the MCA, since in the latter approach partial volume effects affect the shape of the estimated AIF. Second, optimal locations for phase-based AIF selection are similar for different clinical DSC-MRI sequences. Third, phase-based AIF selection allows more locations in tissue to be chosen which show the correct AIF than does magnitude-based AIF selection.

Current selection criteria of automatic AIF-selection algorithms discriminate venous, capillary and arterial profiles based on shape- and timing-characteristics of the first passage. Unfortunately, partial volume effects (PVEs) can lead to shape errors in the bolus passage, including a narrower and higher peak, which might be selected as a "correct" AIF. Chapter 5 introduces a new criterion for AIF selection to exclude partial volume effects, which are normally not excluded by the current selection criteria. This criterion is based on tracer kinetic principles for computing CBV and employs the ratio of the steady-state value to the area-under-the-curve of the first passage, which should result in an equal value for tissue and arterial responses. By employing a reference value from tissue, PVEs-induced shape errors of the AIF measurement can be detected. In vivo data were used to evaluate the proposed approach. The data showed that the new criterion enables detection of shape errors, although false positives do occur, which could be easily avoided when combined with current AIF selection criteria.

Chapter 6 evaluated signal formation in local AIF measurements of DSC-MRI. Often a single global AIF is selected near a large brain-feeding artery. Alternatively, local AIFs could be used, which are measured closer to the capillaries, thereby resulting in better perfusion estimates, because DSC-MRI theory assumes that the employed AIF reflects the input of the microvasculature. However, do the measured local AIFs reflect the true concentration-time curves (CTC) of small arteries? To answer this question we created a 3D numerical model that simulated PVEs in local AIF measurements and compared these to the ground truth. In addition, in vivo data was used to evaluate local AIF candidates selected using two different angiograms. The

findings are two-fold. First, the simulations show that PVEs in the local AIF measurements lead to broader CTCs than the ground truth AIF (caused by the extravascular susceptibility effect and the tissue response). Second, the in vivo data showed that the shape-characteristics of local AIF candidates largely overlap with the shape-characteristics of gray matter CTCs. These findings suggest that local AIF measurements do not reflect the true CTC in the small arteries.

Chapter 7 employs some of the developed techniques in a clinical DSC-MRI study of migraine patients. Whether focal changes in cerebral perfusion are present during the interictal stage of migraine, compared to headache-free control subjects, has not been convincingly demonstrated. In this study, brain perfusion measured with DSC-MRI was compared between 30 interictal female migraineurs (13 migraine with aura, 17 migraine without aura) and 17 female controls to investigate the occurrence of perfusion changes. We conclude that interictal migraine is characterized by discrete areas of hyper- and hypoperfusion that are unspecific for migraine pathophysiology and that do not give an explanation for migraine-associated subclinical cerebellar infarction.

Chapter 8 is a general discussion in which the different aspects for perfusion quantification are discussed with a special focus on the AIF measurement. These aspects are the tracer kinetic theory, the influence of AIF measurements more upstream, correct transformation from the measured MR-signal to the concentration contrast agent, effects of different sampling schemes, different acquisition settings and their influence on the measured signal and partial volume effects. In addition, the pros and cons of automatic AIF measurements are briefly discussed. And the discussion concludes with the limitations of the numerical models used in this thesis.

Samenvatting

Dit proefschrift behandelt het verbeteren van de kwantificatie van hersenperfusie gemeten met *dynamic susceptibility contrast* (DSC-) MRI. De onderzochte verbeteringen zijn voornamelijk toegespitst op de arteriële input functie (AIF) meting. Deze passage van het contrastmiddel door een arterie is nodig voor de kalibratie van de hemodynamische parameters. Naast de handmatige en automatische AIF selectie zijn ook de globale en lokale (of regionale) AIF-metingen onderzocht.

Hoofdstuk 1 is een korte introductie van de onderzochte DSC-MRI-techniek. Dit hoofdstuk introduceert de term AIF en het belang van een correcte AIF voor DSC-MRI.

Hoofdstuk 2 is een overzichtsartikel van twee MRI-technieken voor het meten van hersenperfusie. De technieken verschillen van elkaar door de gebruikte tracer. De eerste techniek is DSC-MRI, een methode die gebaseerd is op de injectie van een exogeen contrastmiddel (een gadolinium derivaat) in een ader van de arm. Door middel van snelle T_2- of T_2^*-gewogen beelden is de eerste passage van het contrastmiddel door het hersenweefsel af te beelden. De tweede techniek is *arterial spin labeling* (ASL), een niet-invasieve techniek die waterstofprotonen in het bloed gebruikt als een endogene tracer. In hoofdstuk 2 worden de belangrijkste elementen voor correcte perfusiemetingen door DSC-MRI en ASL besproken. In DSC-MRI zijn de conversie van signaalverandering naar contrastmiddelconcentratie, de AIF meting en de deconvolutie, de belangrijkste elementen. In ASL zijn de bepaling van de labelingefficiëntie, de correctie voor relaxatie processen en de M_0-calibratie methode de belangrijkste voorwaarden voor een correcte doorbloedingskwantificatie.

Hoofdstuk 3 geeft inzicht in de handmatige AIF-selectie, die gebaseerd is op de magnitude van het MR-signaal nabij de arteria cerebri media (MCA), door middel van numerieke modelering. Een van de moeilijkheden bij het kwantificeren van de perfusie zoals gemeten met DSC-MRI is de juiste bepaling van de AIF, omdat partiële volume-effecten kunnen leiden tot vorm- en amplitudeveranderingen van de AIF. Hersendoorbloeding (*cerebral blood flow* (CBF)) en cerebrale bloedvolume schalen lineair met de oppervlakte onder de AIF, maar vormveranderingen van de AIF kunnen leiden tot grote niet-lineaire fouten. Een numeriek model, gevalideerd door middel van fantoomexperimenten, is gebruikt voor het voorspellen van de optimale lokatie voor AIF metingen in de buurt van de MCA. Uit de experimenten blijkt dat de AIF alleen buiten de arterie goed gemeten kan worden. Daarvoor dient een lineaire relatie

gebruikt te worden tussen ΔR_2^* en contrastmiddelconcentratie. Ook tonen de experimenten aan dat de exacte locatie van de correcte AIF meting verschilt per acquisitie type. Voor een kleine MCA (diameter ≈ 2 mm) geven voxels die het vat omvatten ook een correcte AIF wanneer *segmented EPI* met een korte echo tijd wordt gebruikt.

In hoofdstuk 4 wordt de beste locatie onderzocht voor de handmatige AIF-selectie gebaseerd op de fase van het MR-signaal bij de MCA. In DSC-MRI literatuur is voorgesteld om de AIF-meting middels de fase uit te voeren binnen de arterie. Echter, AIF-selectie gebaseerd op de fase is ook mogelijk in weefsel buiten een arterie zoals de MCA, omdat deze loodrecht op het magneetveld staat en daarbij lokale veldveranderingen induceert in het omliggende weefsel. Het doel van deze studie was om te onderzoeken of AIF-selectie gebaseerd op de fase van het MR-signaal beter uitgevoerd kan worden in het omliggende weefsel dan binnenin de arterie. Daarnaast zijn AIF fase-metingen vergeleken met de AIF gemeten met de magnitude van het MR-signaal. Uit deze studie blijkt ten eerste dat AIF-metingen, gemeten met de fase van het MR-signaal, beter buiten de arterie gemeten kunnen worden, omdat bij AIF metingen in het vat partiële volume effecten de vorm van de gemeten AIF veranderen. Ten tweede, de optimale lokaties voor het meten van de AIF met de fase zijn nagenoeg gelijk voor verschillende klinische DSC-MRI-sequenties. Ten derde, AIF-metingen met de fase kunnen op meer lokaties rondom het vat gedaan worden in vergelijking met de AIF-metingen met de magnitude.

Hoofdstuk 5 beschrijft een nieuw criterium voor (automatische) AIF-metingen. De huidige AIF voxelselectie criteria onderscheiden de curves van de vene, de capillairen en de arterie op basis van vorm en temporele karakteristieken van de eerste passage. Helaas kunnen partiële volume-effecten ook leiden tot vormveranderingen van de bolus passage, zoals smallere hogere pieken, die daardoor juist geselecteerd kunnen worden als correcte AIF. Wij stellen een nieuw criterium voor dat gebaseerd is op tracer kinetiek voor het bepalen van cerebrale bloedvolume. Dit criterium gebruikt de verhouding tussen de evenwichtstoestandswaarde en de oppervlakte onder de eerste passage, welke gelijk moet zijn voor weefsel en arteriële passages. Door middel van een referentiemeting in weefsel kunnen de door partiële volume-effecten geïnduceerde vormveranderingen van de AIF meting gedetecteerd worden. In vivo data is gebruikt om de methode te evalueren. De data laat zien dat het nieuwe criterium het mogelijk maakt om vormveranderingen waar te nemen. Fout positieve waarden treden eveneens op, maar deze kunnen voorkomen worden door gebruik te maken van additionele selectiecirteria die al beschreven staan in de literatuur.

Hoofdstuk 6 evalueert de signaalvorming in lokale AIF-metingen gemeten met DSC-MRI. Normalitair wordt er een enkele globale AIF geselecteerd bij een toevoerende arterie. Lokale AIFs, die dichter bij de capillairen gemeten worden, leiden tot betere perfusiebepalingen omdat de DSC-MRI theorie aanneemt dat de gebruikte AIF de werkelijke invoer van de

microvasculatuur reflecteert. Echter, komen de gemeten lokale AIFs overeen met de werkelijke concentratie-tijd curves (CTC) van smalle arteriën? Om dit te beantwoorden hebben we een 3D-numeriek model gemaakt dat partiële volume-effecten in lokale AIF-metingen simuleert. Dit hebben we vergeleken met de werkelijke invoer door in vivo data te gebruiken voor de evaluatie van lokale AIF-kandidaten die geselecteerd zijn door twee verschillende angiogrammen. De simulaties tonen aan dat partiële volume-effecten in de lokale AIF-metingen leiden tot bredere CTCs dan de werkelijke invoer (veroorzaakt door de extravasculaire susceptibiliteitseffecten en de tissue passage). Ten tweede, de in vivo data laat zien dat de vormkarakteristieken van de lokale AIF-kandidaten grotendeels overlappen met de vormkarakteristieken van grijze stof CTCs. Uit deze bevindingen blijkt dan ook dat de lokale AIF-meting waarschijnlijk niet de werkelijke CTC van kleine arteriën weergeeft.

In hoofdstuk 7 worden de beschreven technieken toegepast in een DSC-MRI-studie om het verband tussen migraine en hersendoorbloeding aan te tonen. Er is nog geen overtuigend bewijs voor de aanname dat focale veranderingen in de hersendoorbloeding voorkomen in de interictale fase van migraine in vergelijking met gezonde proefpersonen. In deze studie is de hersendoorbloeding gemeten met DSC-MRI in 30 interictale vrouwelijke migraineurs (13 migraine met aura, 17 migraine zonder aura) en 17 vrouwelijke controles. Onze bevinding is dat interictale migraine wordt gekarakteriseerd door discrete gebieden van hyper- en hypoperfusie die niet specifiek zijn voor migraine pathofysiologie of geen verklaring kunnen geven voor het op treden van subklinische infracten in de kleine hersenen.

In de algemene discussie (hoofdstuk 8) worden verschillende aspecten voor perfusiekwantificatie en AIF-metingen in het bijzonder beschreven. Deze aspecten zijn onder andere tracer kinetiek, de invloed van het meten van de AIF dichterbij de microvasculatuur, de juiste transformatie van het MR-signaal naar de contrastmiddelconcentratie, effecten van verschillende samplingmethodes, verschillende acquisitieinstellingen en hun invloed op het gemeten signaal en partiële volume-effecten. Daarbij worden de voor- en nadelen van automatische AIF-metingen besproken. De discussie sluit af met het bespreken van de beperkingen van de numerieke modellen die gebruikt zijn in dit proefschrift.

Publications

Bleeker EJW, Webb AG, Walderveen MAA, van Buchem MA, van Osch MJP, *Evaluation of signal formation in local arterial input function measurements of dynamic susceptibility contrast MRI*, under revision

Bleeker EJW, Fonteijn H, Shumskaya E, Schwarzbach J, Norris DG, *Resting state fMRI of retinotopically defined regions in human visual cortex*, under revision

Bleeker EJW, van Osch MJP, Connelly A, van Buchem MA, Webb AG, Calamante F, *A new criterion to aid manual and automatic selection of the arterial input function in dynamic susceptibility contrast MRI*, Magnetic Resonance in Medicine (2011) Feb; 65(2):448-456

Bleeker EJW, van Buchem MA, Webb AG, van Osch MJP, *Phase-based arterial input function measurements for dynamic susceptibility contrast MRI*, Magnetic Resonance in Medicine (2010) Aug; 64(2):358-68

Bleeker EJW, van Osch MJP, *Measurements of cerebral perfusion using MRI*, Imaging in Medicine (2010) Feb; 2(1):41-61

Bleeker EJW, van Buchem MA, van Osch MJP, *Optimal location for arterial input function measurements near the middle cerebral artery in first-pass perfusion MRI*, Journal of Cerebral Blood Flow and Metabolism (2009) Apr; 29(4):840-52

Mulder WJ, Strijkers GJ, Habets JW, **Bleeker EJW**, van der Schaft DW, Storm G, Koning GA, Griffioen AW, Nicolay K, *MR molecular imaging and fluorescence microscopy for identification of activated tumor endothelium using a bimodal lipidic nanoparticle*, Federation of American Societies for Experimental Biology (2005) Dec; 19(14):2008-10

ABSTRACTS FOR PROCEEDINGS

New Criterion for Automatic AIF Selection in DSC Perfusion MRI to Exclude Partial Volume Effects. **Bleeker EJW**, van Osch MJP, Connelly A, van Buchem MA, Webb AG, Calamante F, oral at ISMRM 2010, Stockholm Sweden

New criterion for automatic AIF selection in DSC-MRI to exclude partial volume effects. **Bleeker EJW**, van Osch MJP, Connelly A, van Buchem MA, Webb AG, Calamante F, oral at ESMRMB 2009, Antalya, Turkey

Resting State FMRI of Retinotopically Defined Sub-Regions in Human Visual Cortex. **Bleeker EJW**, Fonteijn H, Shumskaya E, Schwarzbach J, Norris DG, oral at ISMRM 2009, Honolulu, Hawaii

Optimal Location for Phase-Based Arterial Input Function Measurements Near the MCA for DSC-Perfusion MRI. **Bleeker EJW**, van Buchem MA, van Osch MJP, poster at ISMRM 2008, Toronto, Canada

Is PRESTO Advantageous for DSC-Perfusion MRI Using Local AIF Measurements Due to Crushing of Intravascular Signal. **Bleeker EJW**, van Buchem MA, van Osch MJP, poster at ISMRM 2008, Toronto, Canada

Optimal location for AIF selection in bolus tracking perfusion MRI. **Bleeker EJW**, van Buchem MA, van Osch MJP, oral at ISMRM Benelux 2007, Nijmegen, the Netherlands

Arterial input functions from the middle cerebral artery. Where should we select voxels for an accurate AIF? **Bleeker EJW**, van Buchem MA, van Osch MJP, oral at the perfusion workshop of ISMRM 2007, Salvador da Bahia, Brazil

Arterial Input Function Measurements in the MCA: A Numerical Model Compared with Phantom Experiment Results. **Bleeker EJW**, van Buchem MA, van Osch MJP. poster at ISMRM 2007, Berlin, Germany

Functional Hierarchy of the Visual System as revealed by Resting State fMRI. **Bleeker EJW**, Fonteijn HM, Baerends E, Shumskaya E, Norris DG Poster at ISMRM 2007, Berlin, Germany

Curriculum Vitae

Egbert Bleeker was born in Paramaribo, Suriname, in 1980 on the 22nd of April. He grew up with his parents Koos and Greet Bleeker, together with his older brother Bas and older sister Alieke. At the age of thirteen, he took up sailing, which has since been important to him throughout his life. He graduated at the High School Alexander Hegius Lyceum (VWO, Deventer, The Netherlands) in 1998. In that same year, he started his academic education at the faculty of Electrical Engineering, Technical University Twente. The following year he continued his academic education at the faculty Biomedical Engineering of the Technical University Eindhoven from which he graduated with great expectations in 2006, receiving his M.Sc. degree. His graduation project was performed at the F.C.Donders Centre in Nijmegen: the project involved revealing functional and structural connections in the visual cortex of the human brain.

From September 2006 until August 2010, he worked as a PhD-student at the C.J. Gorter Center for High Field MRI of the department of Radiology of the Leiden University Medical Center under the supervision of dr. ir. M.J.P. van Osch, prof. dr. A. Webb and prof. dr. M.A. van Buchem. The results of his research are presented in this thesis.

Dankwoord (Acknowledgements)

Graag wil ik aan het eind van mijn promotie een aantal mensen bedanken die hebben meegeholpen aan de totstandkoming van dit proefschrift.

Allereerst dank ik alle patiënten voor hun bereidheid om deel te nemen aan de MRI studies voor dit proefschrift.

Mijn collega's wil ik bedanken voor hun gezelligheid in leuke tijden en steun in moeilijkere tijden; jullie hebben mij meegeholpen om deze promotie tot een goed einde te brengen. Het was fijn om met jullie te lunchen en om eens in het jaar op onderzoekersweekend te gaan. Jullie zijn hard werkende mensen met gevoel voor humor.

Thijs, dank je wel voor de goede begeleiding en de fijne samenwerking. Je hebt een kritische blik en ik heb veel profijt gehad van jou als co-promotor.

Fernando, I greatly enjoyed working with you and I would like to thank you for the good collaboration.

Mijn promotor Mark, graag wil ik je bedanken voor de goede sturing op vele fronten. Je bent enthousiast en meelevend.

Andrew, my other promoter, thank you for your help in making this PhD-program a success.

Gerrit Kracht, bedankt voor het maken van de foto voor de kaft en je goede adviezen.

Peter, Eline en natuurlijk jullie zoon Boaz, hartelijk dank voor jullie vriendschap en liefde.

Laurens, Allard, Suzan, Joline, Marieke, Joanne, Rianne, Yvonne, Christine, Bianca en de andere van het Leids Christelijk Studenten Netwerk: dank voor gezellige maandagavonden. Ik heb het als erg opbouwend en bemoedigend ervaren.

Erika, Harry, Margreet, Ed, Christian en Patty: dank voor de vriendschap en de gezelligheid.

Simon, Ruth, Luke en Samuel, hartelijk dank voor jullie steun in en na moeilijke tijden.

Bas en Alieke, ik ken jullie al mijn hele leven. Bedankt voor jullie hulp in de afgelopen vier jaar, ik waardeer het enorm.

Mijn ouders, dank jullie voor jullie onvoorwaardelijke liefde voor mij.

Lieve Suzanne, dank je voor je liefde, gezelligheid, steun en adviezen in het laatste stadium van mijn promotietraject.